

In situ studies of silicon-based thin film growth for crystalline silicon solar cells

Citation for published version (APA):

Oever, van den, P. J. (2007). *In situ studies of silicon-based thin film growth for crystalline silicon solar cells*. [Phd Thesis 1 (Research TU/e / Graduation TU/e), Applied Physics and Science Education]. Technische Universiteit Eindhoven. <https://doi.org/10.6100/IR622422>

DOI:

[10.6100/IR622422](https://doi.org/10.6100/IR622422)

Document status and date:

Published: 01/01/2007

Document Version:

Publisher's PDF, also known as Version of Record (includes final page, issue and volume numbers)

Please check the document version of this publication:

- A submitted manuscript is the version of the article upon submission and before peer-review. There can be important differences between the submitted version and the official published version of record. People interested in the research are advised to contact the author for the final version of the publication, or visit the DOI to the publisher's website.
- The final author version and the galley proof are versions of the publication after peer review.
- The final published version features the final layout of the paper including the volume, issue and page numbers.

[Link to publication](#)

General rights

Copyright and moral rights for the publications made accessible in the public portal are retained by the authors and/or other copyright owners and it is a condition of accessing publications that users recognise and abide by the legal requirements associated with these rights.

- Users may download and print one copy of any publication from the public portal for the purpose of private study or research.
- You may not further distribute the material or use it for any profit-making activity or commercial gain
- You may freely distribute the URL identifying the publication in the public portal.

If the publication is distributed under the terms of Article 25fa of the Dutch Copyright Act, indicated by the "Taverne" license above, please follow below link for the End User Agreement:

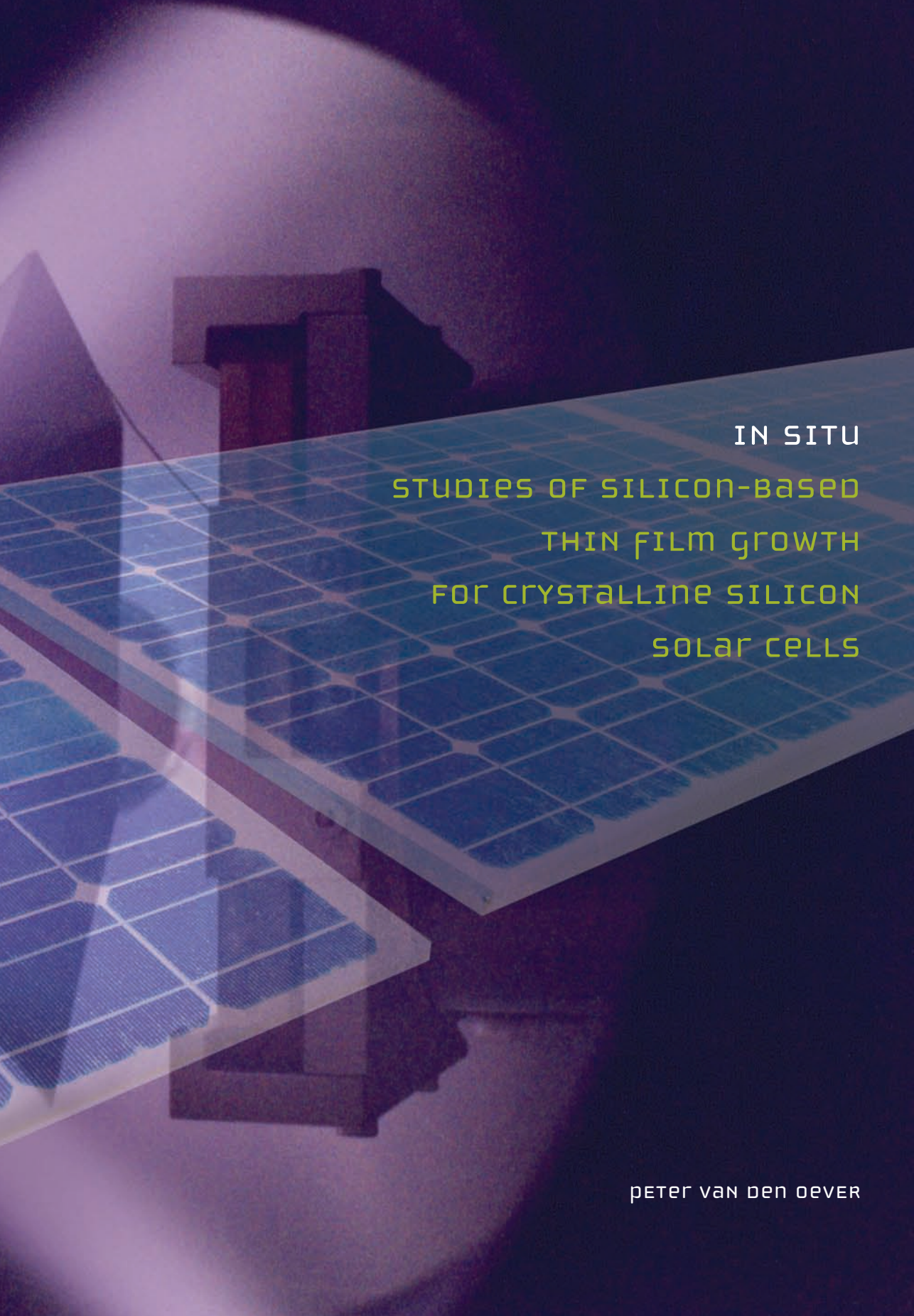
www.tue.nl/taverne

Take down policy

If you believe that this document breaches copyright please contact us at:

openaccess@tue.nl

providing details and we will investigate your claim.



IN SITU
STUDIES OF SILICON-BASED
THIN FILM GROWTH
FOR CRYSTALLINE SILICON
SOLAR CELLS

PETER VAN DEN OEVER

***In situ* studies of silicon–based thin film growth for crystalline silicon solar cells**

PROEFSCHRIFT

ter verkrijging van de graad van doctor aan de
Technische Universiteit Eindhoven, op gezag van de
Rector Magnificus, prof.dr.ir. C.J. van Duijn, voor een
commissie aangewezen door het College voor
Promoties in het openbaar te verdedigen
op donderdag 15 maart 2007 om 16.00 uur

door

Petrus Jacobus van den Oever

geboren te Oss

Dit proefschrift is goedgekeurd door de promotor:

prof.dr.ir. M.C.M. van de Sanden

Copromotor:

dr.ir. W.M.M. Kessels

The work described in this thesis is part of the “HR-CEL” project within the Economy, Ecology, Technology program funded by the Netherlands Ministry of Economic Affairs, the Ministry of Education, Culture and Science and the Ministry of Public Housing, Physical Planning and Environment.

Printed and bound by universiteitsdrukkerij Technische Universiteit Eindhoven

Cover design by Bregje Schoffelen, Oranje Vormgevers

CIP-DATA LIBRARY TECHNISCHE UNIVERSITEIT EINDHOVEN

Van den Oever, Petrus Jacobus

In situ studies of silicon-based thin film growth for crystalline silicon solar cells / by Petrus Jacobus van den Oever. – Eindhoven : Technische Universiteit Eindhoven, 2007. – Proefschrift.

ISBN-13: 978-90-386-2202-6

NUR 926

Trefwoorden: zonnecellen / plasmadepositie / ammonia / plasmadiagnostiek / cavity ring-down spectroscopie / plasmachemie / amorf silicium / ellipsometrie / infraroodspectroscopie

Subject headings: solar cells / plasma deposition / amorphous silicon nitride / plasma diagnostics / cavity ring-down spectroscopy / radical densities / amorphous silicon / ellipsometry / attenuated total reflection infrared spectroscopy

*The reasonable man adapts himself to the world;
the unreasonable one persists in trying to adapt the world to himself.
Therefore all progress depends on the unreasonable man.*

George Bernard Shaw (1856–1950)

Contents

Chapter 1	Framework and overview of the research	1
-----------	--	---

PART I

Chapter 2	Density and production of NH and NH ₂ in an Ar-NH ₃ expanding plasma jet	25
	<i>P.J. van den Oever, J.H. van Helden, C.C.H. Lamers, R. Engeln, D.C. Schram, M.C.M. van de Sanden, and W.M.M. Kessels, J. Appl. Phys. 98, 093301 (2005).</i>	
Chapter 3	Downstream ion and radical densities in an Ar-NH ₃ plasma generated by the expanding thermal plasma technique	49
	<i>P.J. van den Oever, J.L. van Hemmen, J.H. van Helden, D.C. Schram, R. Engeln, M.C.M. van de Sanden, and W.M.M. Kessels, Plasma Sources Sci. Technol. 15, 546 (2006).</i>	
Chapter 4	N, NH and NH ₂ radical densities in a remote Ar-NH ₃ -SiH ₄ plasma and their role in silicon nitride deposition	71
	<i>P.J. van den Oever, J.H. van Helden, J.L. van Hemmen, R. Engeln, D.C. Schram, M.C.M. van de Sanden, and W.M.M. Kessels, J. Appl. Phys. 100, 093303 (2006).</i>	

PART II

Chapter 5	Real time spectroscopic ellipsometry on ultrathin (<50 Å) hydrogenated amorphous silicon films	97
	<i>P.J. van den Oever, M.C.M. van de Sanden, and W.M.M. Kessels, submitted for publication</i>	
Chapter 6	Hot-wire deposition of a-Si:H thin films on wafer substrates studied by real-time spectroscopic ellipsometry and infrared spectroscopy	119
	<i>P.J. van den Oever, J.J.H. Gielis, M.C.M. van de Sanden, and W.M.M. Kessels, accepted for publication in Thin Solid Films</i>	
Summary		131
Acknowledgements		135
Curriculum Vitae		139

Chapter 1

Framework and overview of the research

I. Solar cell related research



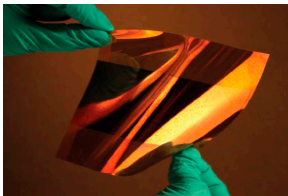
A. The three solar cell generations

The present global research efforts in the field of solar cells can be categorized in three generations, following Green *et al.* [1]. The “first generation” consists of conventional wafer-based crystalline silicon solar cells, which have dominated terrestrial photovoltaics since the introduction of the world’s first successful solar cell in 1954 [2]. The less material intensive thin film technology forms the basis for the “second generation”, which is generally regarded as the successor of first generation solar cells but has not lived up to that promise yet as reflected in their market share of 6% in 2005. The “third generation” is characterized by revolutionary new concepts, either based on conversion efficiencies far exceeding those of current first and second generation solar cells or on substantially lower production costs.

Most of the investigated solar cell concepts can be divided into these three generations as is shown in Table 1, which also shows the corresponding cumulative market share in 2005. First generation solar cell technology, which is based on mono- and multi-crystalline silicon (also called poly-crystalline), has benefited enormously from the fast developments in the integrated circuit (IC) industry. In 2005, the cumulative world production of first generation solar cells was 1.6 GW, which corresponds to a market share of 94 %. Currently, first generation technology has reached maturity and both mono- as well as multi-crystalline silicon solar cells are increasingly mass produced as is witnessed by the yearly 30–40 % increase in production volume in the photovoltaic industry [3]. To sustain this production volume growth with the corresponding cost reduction, the industry critically depends on the availability of high-throughput manufacturing tools, which was a problem in the early days of large volume commercial cell production. Apart from lower manufacturing costs induced by mass production, increasing conversion efficiencies offer another option for cost reduction. New, high efficiency solar cell concepts based on crystalline silicon are therefore actively investigated [4]. Examples of already commercialized high efficiency solar cells are the back-contact solar cell and the Heterojunction with Intrinsic Thin film (HIT™) solar cell manufactured by SunPower Corporation (U.S.A.) and Sanyo (Japan), respectively [5,6].

The 6 % remaining market share in 2005 was taken by second generation solar cells, consisting mainly of contributions of amorphous silicon (a-Si:H), cadmium telluride (CdTe) and copper indium diselenide (CIS) solar cells. Other high potential thin film technologies are based on the creation of crystalline silicon thin films either by crystallization of amorphous silicon or by epitaxial growth on low cost substrates such as glass [7,8]. Although some of these thin film solar cell concepts

Table 1: Solar cell concepts divided into three solar cell generations.

First generation: Silicon wafer based	
<p>Mono-crystalline silicon diffused emitter Single crystal silicon; Commercialized on large scale; Record efficiency 24.7 %*.</p> <p>Silicon heterojunction (SHJ) Single crystal silicon; Amorphous silicon emitter and back surface contact; Simple fabrication process; Commercialized; Record efficiency 21.8%.</p> <p>Multi-crystalline silicon diffused emitter Centimeter-sized grains of single crystal material; Defects at grain boundaries; Commercialized on large scale; Record efficiency 20.3 %.</p> <p>Ribbon silicon (EFG and String) Alternative fabrication of crystalline silicon wafers; Contains crystallographic defects; Commercialized; Record efficiency 17.7% [9].</p>	<p>2005 production: 1652 MW[†] 2005 market share: ~94 %</p>  <p>Arnstein, Germany 12 MW; http://www.sunpower.com</p>
Second generation: Thin film	
<p>Hydrogenated amorphous silicon (a-Si:H) Deposited from silane containing gas mixtures; Direct bandgap; Light-induced degradation; Small scale production ; Record efficiency 9.5%.</p> <p>Hydrogenated microcrystalline silicon (μc-Si:H) Deposited from silane-hydrogen mixtures; Nanometer-sized crystalline silicon grains; Record efficiency 10.1%.</p> <p>Cadmium Telluride (CdTe) Chalcogenide; Small scale production; Record efficiency 16.5%.</p> <p>Copper Indium Gallium Diselenide (CIGS) Chalcogenide; Small scale production; Record efficiency 18.8%.</p> <p>Copper Indium Diselenide (CIS) Chalcogenide; Small scale production; Record efficiency 11.4% [10].</p> <p>Thin film crystalline silicon Crystallization of a-Si:H or epitaxial growth; Small scale production; Record efficiency 16.6%.</p>	<p>2005 production: 108 MW 2005 market share: ~6 %</p>  <p>Ellensburg, USA 1.6 kW; http://www.brooksolar.com</p>
Third generation: New concepts	
<p style="text-align: center;">A: “Low-cost concepts”</p> <p>Organic Plastic or polymer; Potentially cheap; Record efficiency 4.8%.</p> <p>Dye sensitized (Grätzel) Mimics photosynthesis; Record efficiency 10.4%.</p>	<p>2005 production: 0 MW 2005 market share: ~0 %</p>  <p>Polymer solar cell; http://www.afrlhorizons.com</p>
<p style="text-align: center;">B: “High-efficiency concepts”</p> <p>Multi-junction devices of III-V semiconductors Better use of solar spectrum; Elaborate production process; Record efficiency 32.0%.</p> <p>Hot carrier Prevents charge carriers from losing energy to lattice.</p> <p>Up/down conversion Converts multiple non-absorbable photons into absorbable photons.</p>	

* Record efficiencies on cell level. M.A. Green, K. Emery, D.L. King, Y. Hishikawa, and W. Warta, Progress in Photovoltaics 15, 35 (2007).

[†] From PV News 25, April 2006

are commercialized on a small scale, second generation solar cell technology is still far less developed than first generation technology. To a large extent, this is caused by the lack of high-throughput manufacturing equipment on the market. A similar lack also delayed the commercial implementation of first generation solar cell technology as mentioned before. An extensive review of thin film solar cell concepts and their market status is beyond the scope of this thesis, but can be found in Ref. 11 and 12.

Most third generation solar cell concepts are far from the commercial stage and various technologies with breakthrough potential are investigated world wide. Within this category a subdivision can be made based on a cost reduction or high efficiency incentive. A good example of a solar cell concept that has the potential for inexpensive mass production is the class of organic solar cells. However, the current record conversion efficiency must be increased significantly to make commercialization of organic solar cells economically viable [13]. On the other hand, examples of third generation concepts capable of reaching significantly higher efficiencies are multi-junction solar cells based on III-V semiconductors, hot carrier solar cells, and solar cells that incorporate up- or down conversion of photons [14,15]. These concepts, often based on semiconductor nanotechnology aim on using the energy content in sunlight more efficiently by creating multiple electron-hole pairs per incident photon or by extracting "hot" photoexcited charge carriers from the solar cell that did not lose their energy to the lattice yet. Another exciting research branch is focused on the secrets of photosynthesis, the natural process that converts sunlight into chemical energy. Dye sensitized cells (Grätzel cells) try to mimic this process and have a current record efficiency of ~11% [16]. Rapid advances in nanotechnology and molecular biology hopefully provide the means for future breakthroughs in solar energy conversion.

To explore the cost-effectiveness of the three solar cell generations, it is useful to take an economic perspective by considering the conversion efficiency and the production costs per unit area as is shown in Fig. 1. First generation solar cells (I) are characterized by high production costs per unit area and intermediate conversion efficiencies. The thin film concepts (II), on the other hand, can potentially be produced at substantially lower production costs, but their efficiency is also significantly lower compared to first generation solar cells. Finally, third generation solar cells combine low production costs with intermediate conversion efficiencies (IIIa), or vice versa, intermediate production costs with a high conversion efficiency (IIIb). Figure 1 demonstrates that third generations solar cells have a large potential to become economically viable, at least when the existing technological challenges will be overcome.

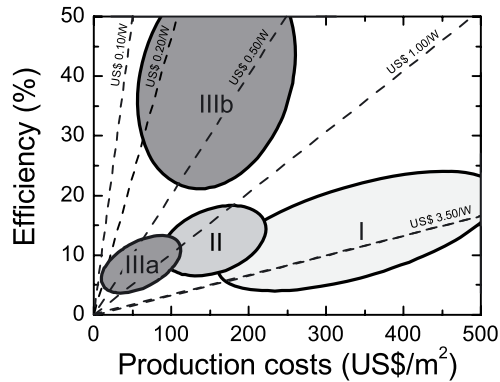


Figure 1: The three generations of solar cells viewed from an economical perspective based on production costs and conversion efficiency. The dashed lines represent equal costs per unit energy produced. Free after Green [1].

Until 2015 however, it is expected that the strongly expanding solar cell market will still be dominated by first generation crystalline silicon solar cells, despite the upcoming silicon feedstock shortage [3]. This (temporary) shortage results in increasing prices for silicon wafers and provides a window of opportunity for accelerated introduction of advanced production technologies of high efficiency and thin film solar cells modules. After 2015, it is expected that the market share of 2nd generation solar cells will increase and eventually (after 2025) 3rd generation solar cells will penetrate the market bringing down the costs significantly.

B. Framework of the current research

The work described in this thesis was carried out in collaboration with OTB Solar B.V. within the “HR-CEL” project. This project is part of the Economy, Ecology, Technology program funded by the Netherlands Ministry of Economic Affairs, the Ministry of Education, Culture and Science and the Ministry of Public Housing, Physical Planning and Environment. OTB Solar B.V. develops and sells industrial tools for inline production of crystalline silicon solar cells. The company took a license on the use of the expanding thermal plasma (ETP) source, which was developed and patented by the Eindhoven University of Technology [17], for the deposition of amorphous silicon nitride (a-SiN_x:H) antireflection coatings on crystalline silicon solar cells. OTB Solar’s first commercial product, the “DEPx”, uses three ETP sources and is well suited for high throughput production in an inline configuration because of the high deposition rates attainable with the ETP technique [18–20].

The collaboration with OTB Solar B.V. and the general consensus that the photovoltaic market will be dominated by crystalline silicon solar cells for at least

another decade, provided the reason to focus this thesis work on first generation solar cells. Within this field, two main points of interest can be distinguished with respect to thin film and plasma processing. In the first place, it is important to facilitate high-throughput production by investigation and optimization of high-rate deposition techniques for the synthesis of functional materials applied in solar cells. The a-SiN_x:H antireflection coating that can be deposited at high rates with the DEP_x system is a good example of such a functional material. Apart from its antireflection properties, the a-SiN_x:H film increases the solar cell efficiency significantly by passivating defects in the bulk of multicrystalline silicon and by reducing the recombination loss at the surface of crystalline silicon. In Part I of this thesis, the properties of this layer and the details of the deposition process using the ETP source are researched extensively.

Secondly, improved solar cell concepts that yield higher conversion efficiencies or a less complicated fabrication process are actively being studied. With the shrinking of the wafer thickness in solar cells, the importance of controlling the interface properties has drastically increased. This is evidenced by the recent interest in materials that provide excellent passivation of surface defects on crystalline silicon wafers. Another application that critically relies on accurate control of the interface properties is the silicon heterojunction solar cell [21], which uses ultrathin amorphous silicon films deposited on a crystalline silicon wafer to create emitter and back surface contacts. Hence, Part II of this thesis is focused on a general approach to study the interface formation between a wafer and a thin film deposited on top. Our laboratory is equipped with several diagnostic techniques that are exceptionally suited to study different aspects of the interface formation. Due to the emerging solar cell applications of amorphous silicon deposited on crystalline silicon (e.g. as surface passivation material [22] or in the silicon heterojunction (SHJ) solar cell [6]), the interface formation between these materials was chosen as a model system. In addition, extensive experience with high-rate deposition of amorphous silicon using the ETP source is present in our group at the Eindhoven University of Technology [23]. Eventually, when the present fundamental and technological barriers are overcome, the ETP technique might also be used for high-throughput deposition of amorphous silicon using the industrial DEP_x system for solar cell applications.

C. Outline of this thesis

The remainder of this chapter as well as the rest of this thesis is divided into two parts, which deal with the aforementioned subjects within first generation solar cell research. Section II gives an overview of the HR-CEL project and discusses the characterization of the ETP plasma source in terms of reactive species, which is described in detail in Chapters 2 and 3 of this thesis. In addition, the a-SiN_x:H

deposition mechanism is discussed in more detail, which is the main subject of Chapter 4.

Section III deals with the second part of the thesis and starts with background information about the applications of a-Si:H deposited on crystalline silicon wafer substrates. The choice for this model system is substantiated and the experimental approach to unravel the growth of ultrathin a-Si:H films on various wafer substrates and the corresponding interface formation between the wafer and a-Si:H film is presented. Subsequently, we discuss the change in dielectric function observed for ultrathin films in Chapter 5 and the formation of a hydrogen rich interface layer in Chapter 6.

Finally, the last section of this chapter (Sec. IV) looks out to fundamental as well as technological challenges within the field of thin film and plasma processing related to solar cell technology.

II. Silicon nitride deposition by the expanding thermal plasma technology

A. *The HR-CEL project*

While the potential of a-SiN_x:H as an antireflection coating was already recognized in the early eighties [24,25], wide-scale implementation into solar cell production lines was hindered for a long time by the lack of equipment for large scale production. OTB Solar reacted on the industrial demand for silicon nitride mass production equipment and developed the DEP_x, a commercial tool based upon the expanding thermal plasma (ETP) technique. The remote ETP technique, patented and developed by the Eindhoven University of Technology [15], is capable of high rate deposition of many materials including silicon nitride [21–28], which makes it extremely suitable for high-throughput production [29]. Additional details about the working principle of the ETP technique can be found in Frame 1. Figure 2 shows the lab-scale reactor employing the ETP technique as well as the commercial DEP_x system. This high throughput system with the sophisticated Linear Motor System used for carrier transport, yields high quality silicon nitride coatings with a good uniformity over the total carrier width of 36.5 cm [30]. The DEP_x distinguishes itself from competitors by its high deposition rate (4–20 nm/s), small inline footprint (4.5 x 2.5 m) and low gas consumption, which ensure low operational costs. In the same year as the market introduction of the DEP_x system, the “HR-CEL” project was started (2002). At this point in time, the multicrystalline silicon solar cell industry was largely making the transition from TiO₂ to a-SiN_x:H as an antireflection coating, because it was evident that passivation of bulk defects by hydrogen incorporated in the a-SiN_x:H layers would be a very important factor to increase the efficiency of solar cells based on intrinsically defect-rich multicrystalline silicon. It was already demonstrated

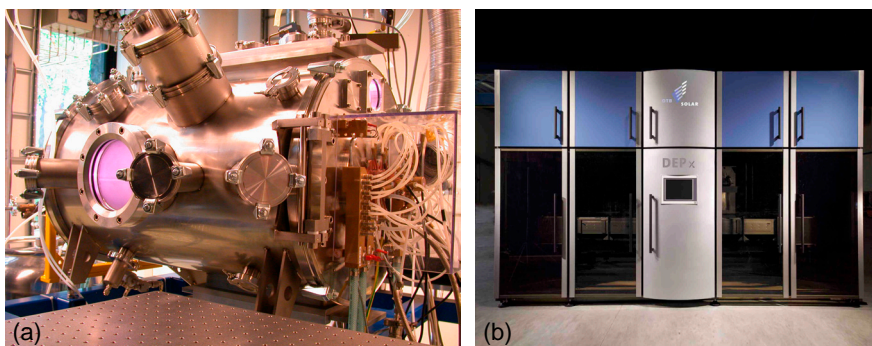


Figure 2: (a) The lab-scale reactor used for the silicon nitride plasma chemistry experiments. The plasma source is situated on the right side of the picture. (b) The “DEPx” system for commercial silicon nitride deposition produced by OTB Solar B.V. (dimensions: 4.5 x 2.5 m²).

within the Sunnovation project [31] for lab-deposited a-SiN_x:H films that the bulk passivation properties of films deposited by SiH₄-NH₃ containing ETP plasmas were substantially better than those deposited by SiH₄-N₂-H₂ containing ETP plasmas [19]. In addition, a clear correlation between mass density of the a-SiN_x:H and the level of bulk passivation [20] was demonstrated for films deposited from SiH₄-NH₃ plasmas. Therefore, the current project was initially focused on transferring the good bulk passivation properties obtained in the lab to films deposited with the industrial DEPx system. In this process, the refractive index of the a-SiN_x:H film, which correlated directly to the mass density, was used as control variable, while nuclear analysis by Rutherford backscattering measurements provided an independent determination of the mass density. Simultaneous optimization of the refractive index and absorption coefficient of the deposited a-SiN_x:H film using spectroscopic ellipsometry, yielded a substantial increase in the mass density [32]. Multicrystalline silicon solar cells that included these layers showed a clear increase in conversion efficiencies from 14.3 to 15.3 %, when the mass density increased from 2.05 to 2.45 g/cm³ [18]. This increase in efficiency as a function of mass density was attributed to the passivation of defects in the bulk of the multicrystalline silicon during a high-temperature process step, as was first reported by Hong *et al.* [20]. The method for passivating a semiconductor substrate using ETP deposited a-SiN_x:H was patented by OTB Solar B.V. [33].

For monocrystalline silicon solar cells the bulk material generally contains a low density of defects and consequently the passivation of defects on the silicon surface, which are largely responsible for the recombination of photogenerated charge carriers in these types of solar cells, has become important to increase the efficiency. This is especially true due to the decreasing thickness of the silicon wafer substrates used in solar cells. The level of surface passivation, expressed by the

Frame 1: The expanding thermal plasma technique for silicon nitride deposition

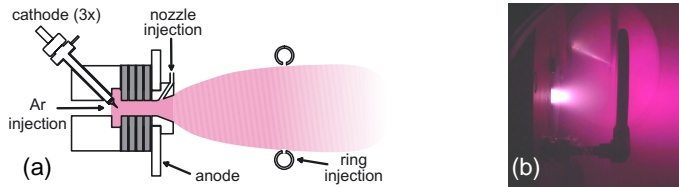


Figure 3: (a) Schematic overview of the ETP plasma source, the cathodes and anode, the nozzle used for NH_3 injection and the ring used for SiH_4 injection. (b) A picture of a pure Ar expansion from the nozzle. The SiH_4 injection ring is visible.

Figure 3 shows a schematic overview of the so-called cascaded arc plasma source used in the ETP technique [15] for high rate deposition of materials such as amorphous silicon [21], silicon dioxide [24], amorphous carbon [25], zinc oxide [26] and amorphous silicon nitride [17]. The plasma is created at high pressure in a narrow channel (typically 4 mm in diameter and a few centimeters in length) filled with a non-depositing gas such as Ar, N_2 and/or H_2 by applying a dc voltage between one or more cathodes and one common grounded anode. The cathode(s) and anode are separated by typically four ‘cascaded’ plates which are at floating potential. The discharge is current controlled between 30 and 75 A and the voltage is typically 40 V when operated at a typical Ar flow of 55 standard $\text{cm}^3 \text{ s}^{-1}$ (sccs). In this case the high pressure of typically 400 mbar and high gas temperature in the plasma channel, result in very effective ionization of the Ar atoms and the ionization degree in the plasma channel can be as high as 10–20 %. As reported previously [47], the plasma expands supersonically from a conical shaped nozzle into a low pressure reactor at typically ~ 0.2 mbar until it reaches the stationary shock that is situated approximately 7 cm from the source exit. Subsequently, the expansion continues subsonically and in this stage the plasma can be characterized as recombining plasma as no electrical power is coupled into the plasma in this downstream zone. The electron temperature is low (0.2–0.3 eV) and as a consequence electron impact induced chemistry and ion bombardment due to the plasma self bias are virtually absent, contrary to the situation in many conventional plasma techniques. When the expanding thermal plasma (ETP) source is operated at pure argon, the main reactive species are Ar^+ ions (downstream ionization degree 5–10 %) as the density of argon metastables is more than a factor of 10 lower than the Ar^+ density [49]. In this situation the Ar^+ density increases linearly with the arc current [48]. When molecular gases (e.g., H_2 and/or N_2) are admixed in the operating gas of the plasma source, the ionization degree in the downstream plasma is effectively quenched by molecular ion–electron recombination and the plasma source acts as an efficient atom (H,N) source.

The Ar-NH_3 and $\text{Ar-NH}_3\text{-SiH}_4$ plasmas discussed in this thesis are generated by injecting a NH_3 flow (0–17 sccs) at the outlet of the plasma source operated at pure Argon via a slit in the nozzle. The SiH_4 flow (0–5 sccs) is injected via an injection ring located at approximately 8 cm from the plasma source exit.

surface recombination velocity, was deduced from charge carrier lifetime measurements using a contactless inductively coupled photoconductance tester (Sinton Consulting, WCT100) [18]. Preliminary studies into the surface passivation were not very successful, despite the fact that these layers did yield a fair level of bulk passivation [34]. After reaching an excellent level of bulk passivation for a-SiN_x:H films deposited by the commercial DEP_x system using SiH₄-NH₃ plasmas, the interest in the surface passivation properties of these films was renewed. Fortunately, the films with excellent bulk passivation properties also showed excellent surface passivation properties demonstrated by a constant effective surface recombination velocity S_{eff} of ~60 cm/s over the refractive index range from 1.9 to 2.4. The levels of bulk as well as surface passivation reported here are comparable to the values obtained by other state-of-the-art commercial deposition techniques with lower deposition rates of the a-SiN_x:H. More details on the bulk and surface passivation properties of the a-SiN_x:H films deposited by the industrial DEP_x system can be found elsewhere [18]. Apart from surface passivation by silicon nitride, excellent levels of surface passivation by hydrogenated amorphous silicon, silicon dioxide, and aluminum oxide film were reached in our group [35-37]. The details of this work will be described in a second thesis within the HR-CEL project [38].

During the HR-CEL project, spectroscopic ellipsometry (SE) has played an important role as it provides a relatively easy measurement of the dielectric function of the deposited a-SiN_x:H film. Apart from the optimization of bulk and surface passivation properties using SE, efforts were undertaken to gain insight into the dynamics of the a-SiN_x:H growth by real time SE and atomic force microscopy (AFM) measurements. These fundamental studies showed that a growth process with a slow time-increase in surface roughness is beneficial for the deposition of high density films [39]. However, the high growth rates of the ETP deposited a-SiN_x:H complicated the data analysis of the real time SE measurements to such an extent that information about the first 100 nm of growth could not be extracted accurately. Exactly this thickness range is used for deposition of a-SiN_x:H antireflection coatings with a typical thickness of 70-90 nm. Therefore, it was decided to postpone the real time SE measurements until the measurement speed or signal-to-noise ratio of the spectroscopic ellipsometer was improved. A viable option to increase the signal-to-noise ratio of the measurements is the use of a brighter light source, such as the cascaded arc light source [40,41]. The feasibility of this option was demonstrated, but the cascaded arc light source has not been incorporated in the spectroscopic ellipsometer yet.

Apart from critical issues that had to be solved for successful commercial implementation of the DEP_x system such as the bulk and surface passivation properties of the deposited a-SiN_x:H films, there existed a genuine interested (from

industry as well as scientific point of view) into the reactive species produced by the plasma source operated at argon–ammonia mixtures. Remarkably, only few experimental studies on the chemistry in NH_3 –based plasmas have been reported in the literature, despite the widespread application of these plasmas for surface treatment and deposition. Although ammonia radical species (N , NH and NH_2) are expected to be very important for surface treatment as well as for deposition, none of the reported studies addressed the chemistry involved in NH_x radical production in detail. Also for the NH_3 – SiH_4 plasma, which is widely used in the semiconductor as well as in the solar cell industry to deposit a– $\text{SiN}_x\text{:H}$, the details of the plasma chemistry itself are largely unknown. Consequently, also the species responsible for a– $\text{SiN}_x\text{:H}$ growth are not identified yet. In the literature, two growth mechanisms for deposition of a– $\text{SiN}_x\text{:H}$ from NH_3 – SiH_4 plasmas are proposed. The first one is based on gas phase creation of amino–silane radicals, while in the second mechanism the silicon–nitrogen bond is created on the surface of the growing film by incident SiH_x ($x = 0\text{--}3$) and NH_x ($x = 0\text{--}2$) radicals. In both mechanisms however, NH_x radicals are expected to play a key role. Therefore, the plasma chemical investigations reported in this thesis work have been concentrated on the NH_x radicals and the most important results are summarized in the next section.

B. Plasma chemistry of the Ar– NH_3 and Ar– NH_3 – SiH_4 plasma used for silicon nitride deposition

The fundamental plasma chemical issues described in the previous section were investigated at the lab–scale ETP reactor situated at the Eindhoven University of Technology and are described in Chapters 2–4 of this thesis. The large history in plasma chemical investigations of the Plasma & Materials Processing group provided an ideal background for the characterization of the reactive species produced by the plasma source and the identification of the growth precursors for a– $\text{SiN}_x\text{:H}$ deposition from ammonia–silane containing plasmas. Figure 4 (a) shows the lab–scale ETP reactor equipped with optical access for the detection of gas phase species by cavity ring–down absorption spectroscopy [42] and a Langmuir probe system [43] to measure the ion density and electron temperature. Figure 4 (b) shows the same setup with a (threshold ionization) mass spectrometer [44] installed to probe neutral as well as ionic species in the plasma beam, while a residual gas analyzer was used to probe the background gas composition. First, these diagnostics were used to identify the most important reactive species in the Ar– NH_3 plasma, that serves as the source for reactive species to dissociate the SiH_4 injected in the plasma used for a– $\text{SiN}_x\text{:H}$ deposition. Subsequently, the effect of SiH_4 injection was investigated, focusing on the role of the reactive species in the deposition of silicon nitride.

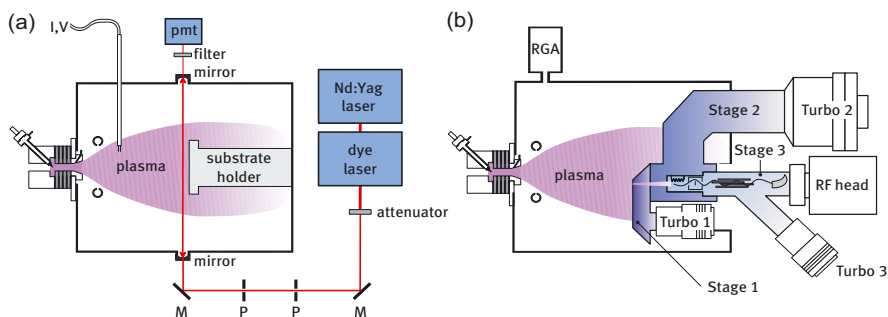


Figure 4: Overview of the plasma diagnostics used to unravel the chemistry of the Ar–NH₃ and Ar–NH₃–SiH₄ plasmas used to deposit silicon nitride. (a) The cavity ringdown absorption spectroscopy setup is shown, together with the Langmuir probe system. (b) The threshold ionization mass spectrometry setup is shown as well as the residual gas analyzer. The triple stage differentially pumped mass spectrometer probes the plasma in direct line-of-sight.

The measured absolute densities of NH and NH₂ radicals in the expanding Ar–NH₃ plasma and their production mechanism are discussed in Chapter 2. These results are extended in Chapter 3 with N radical and ion composition measurements in the plasma. The absolute densities of N, NH and NH₂ radicals in the plasma are in the order of 10¹² cm⁻³. All together, the results of Chapter 2 and 3 provide a thorough understanding of the important processes in the Ar–NH₃ plasma generated by the ETP plasma source, which is used to dissociate SiH₄ in the case of silicon nitride deposition. Table 2 gives an extensive overview of the values of various important plasma parameters and the techniques used to measure them. It must be noted that to date none of the other commercial plasma sources for a–SiN_x:H deposition have been characterized as extensively as the ETP source.

Chapter 4 discusses the effect of SiH₄ addition to the plasma and investigates the role of the N, NH and NH₂ radical species in the growth mechanism of silicon nitride. It was shown that N and NH₂ radicals are mainly responsible for the incorporation of atomic nitrogen in the film, while silicon atoms are most likely brought to the surface in the form of SiH_x (x=0–3) radicals. In the near future, detailed measurements of the SiH_x (x=0–3) radical densities by cavity ring-down spectroscopy or threshold ionization mass spectrometry are planned to elucidate the role of the SiH_x radicals further. The insights into the densities of the plasma species and their role in the deposition process gained in this thesis work are beneficial to effectively optimize process conditions or to adapt the deposition process to new applications.

Table 2: Summary of the ETP plasma properties including the diagnostic techniques used to measure them.

Plasma property	Parameter range	Plasma diagnostic	Reference
Electron temperature	0.1–0.3 eV	Thomson scattering; Langmuir probe	[45,46] Ch. 2, 3
Ion density	$\sim 10^{13} \text{ cm}^{-3}$ (pure Ar plasma) $10^{10} \text{--} 10^{11} \text{ cm}^{-3}$ (Ar–NH ₃ plasma)	Thomson scattering; Langmuir probe	[45,46] Ch. 2, 3
Ar ⁺ metastables density	$< 10^{12} \text{ cm}^{-3}$ (pure Ar plasma)	Absorption spectroscopy	[47]
NH _x and SiH _x radical densities	$\sim 10^{12} \text{ cm}^{-3}$ (NH _x in Ar–NH ₃ plasma) $\sim 10^{11} \text{ cm}^{-3}$ (SiH _x in Ar–NH ₃ –SiH ₄ plasma)	Threshold ionization mass spectrometry; Cavity ring down spectroscopy; Laser induced fluorescence	Ch. 2–4
Ion energy at substrate	1–2 eV	Langmuir probe Ion mass spectrometry	[45]
Gas temperature	1000–2000 K	Cavity ring down spectroscopy; Laser induced fluorescence	[48,49] Ch. 2
Heat load on substrate	0.3–0.6 W cm ⁻²		[50]

III. Deposition of ultrathin amorphous silicon films for solar cell applications

A. Background information

The second part of this thesis is focused on high conversion efficiency concepts within the first generation solar cells. The ongoing introduction of complex high efficiency cell structures at the research level, as well as the overall increase in cell performance observed in industry has emphasized the importance of a good quality interface between the different layers in the solar cell. In particular, the interface between the silicon wafer and the deposited thin film on top is very important to increase the efficiency of crystalline silicon solar cells. This is witnessed by the present high efficiency concepts that incorporate dedicated layers of silicon dioxide, silicon nitride, or amorphous silicon for surface passivation of the front as well as the backside of the silicon wafer. Besides its application for surface passivation, amorphous silicon is also used in the silicon heterojunction solar cell (SHJ) that relies critically on the interface quality as well.

Despite the importance of a good quality interface between the materials in the solar cell, the physical properties of these interfaces have not been investigated in full depth. The mechanism of surface passivation as well as the working principle of the SHJ solar cell, which is based on the deposition of ultrathin amorphous silicon layers on both sides of a silicon wafer as emitter and back surface contact [51,52], is not well known. This is demonstrated by the fact that to date no solar cell lab was able

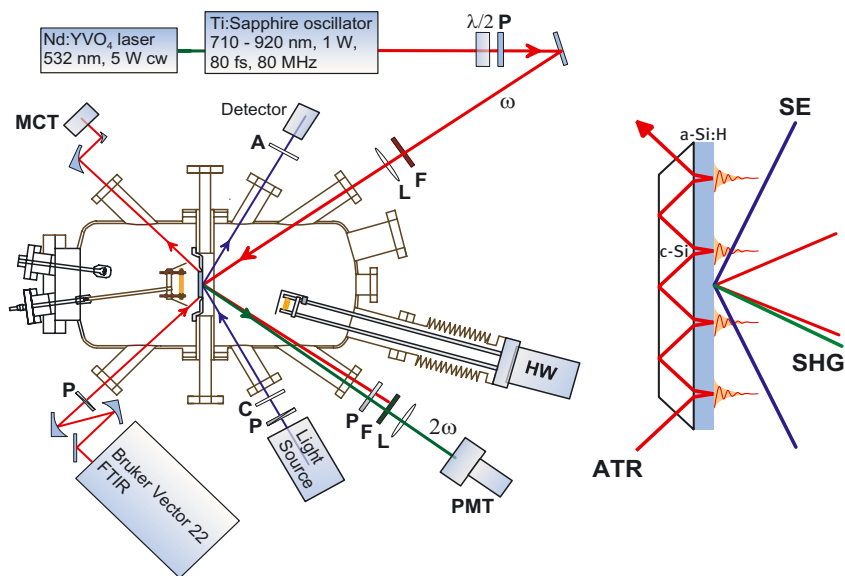


Figure 5: The UHV hot wire CVD deposition setup equipped with three *in situ* and real time diagnostics to study the interface created during the growth of ultrathin amorphous silicon films. Infrared absorption spectroscopy in the attenuated total reflection (ATR) geometry is used to probe silicon–hydrogen bonds in the growing films, while spectroscopic ellipsometry (SE) is used to monitor the dielectric functions and the thickness of the film. The third diagnostic is the interface– and surface–sensitive second–harmonic generation (SHG) technique that is used to monitor the optical resonance of the Si–Si bond at ~ 3.4 eV.

reproduce the SHJ solar cell efficiencies reported by inventor Sanyo. Recently, the SHJ solar cell has gained considerable attention and therefore the research efforts into a–Si:H growth on silicon wafers were intensified. These research efforts have resulted in evidence that the surface condition prior to a–Si:H deposition is crucial, as well as the creation of a sharp interface between the c–Si and the a–Si:H. In addition, it was demonstrated that epitaxial growth and a subsequent transition to the amorphous phase is undesirable for SHJ applications [21,53]. Therefore, further insight into and ultimately control of the interface properties is important to increase the efficiency of first generation solar cells to the next level.

The second part of this thesis is focused on gaining more insight into the interface created in the deposition of ultrathin amorphous silicon films on crystalline silicon. Good control of this interface might for example enable high–throughput industrial deposition of amorphous silicon with the DEP_x system. However, some fundamental and technological issues need to be solved before such a commercial application can be realized. Therefore, we focus on the detection of the properties of

the interface between the amorphous silicon and the underlying wafer substrate. In addition, we investigate the properties of the ultrathin a-Si:H films, that might be very different from the bulk film properties. Specific questions that come to mind are: What is the influence of the process conditions on the interface layer? Is the interface atomically sharp or more like a gradient layer? How are ultrathin a-Si:H films different from “bulk” material? Can we grow an atomically sharp interface between crystalline and amorphous silicon without an intermediate epitaxial silicon layer?

B. The interface between amorphous and crystalline silicon

To gain insight into the interface between amorphous silicon and crystalline silicon, a multi-diagnostic approach was applied. We implemented three real-time and in-situ diagnostics that can be operated simultaneously during the growth of ultrathin amorphous silicon films on crystalline silicon substrates, as is shown schematically in Fig. 5. Spectroscopic ellipsometry (SE) detects the change in polarization state of light upon reflection off a sample and yields information about the optical and structural properties of the films. Attenuated total reflection (ATR) infrared absorption spectroscopy was used to measure the stretching vibration of SiH, SiH₂ and SiH₃ groups in the hydrogenated amorphous silicon and yields information about the bonded atomic hydrogen content in the films. Finally, the surface and interface sensitive, non-linear optical technique of second-harmonic generation (SHG), was used to resonantly probe the Si-Si bonds in the interface layer. The use of these three all-optical and therefore non-intrusive techniques simultaneously, both in-situ and in real-time during thin film growth is unique and can yield detailed information about different aspects of the growth process.

The first experiments employing SE and ATR infrared absorption spectroscopy were carried out on GaAs substrates that are well suited for infrared measurements at elevated temperatures. Subsequently, all three diagnostics were used simultaneously and in real time during a-Si:H growth on Si(100) with native oxide intact. Finally, the a-Si:H was deposited on hydrogen terminated crystalline silicon and monitored by all three diagnostics simultaneously during the growth process. The real-time ellipsometry measurements of the deposition of ultrathin a-Si:H clearly indicated a change in the dielectric functions of the ultrathin layer with respect to the bulk film values (Chapter 5). An elaborate data analysis procedure showed that the optical bandgap of the a-Si:H is higher for thinner films. In the literature, this effect is often assigned to quantum confinement effects or to excess hydrogen content in the ultrathin film. Using ATR infrared absorption spectroscopy we found evidence for the creation of a hydrogen rich interface layer with a thickness of 10–24 Å, depending on substrate temperature (Chapter 6). The presence of this interface layer was corroborated by secondary ion mass spectrometry. Nevertheless, we showed that this

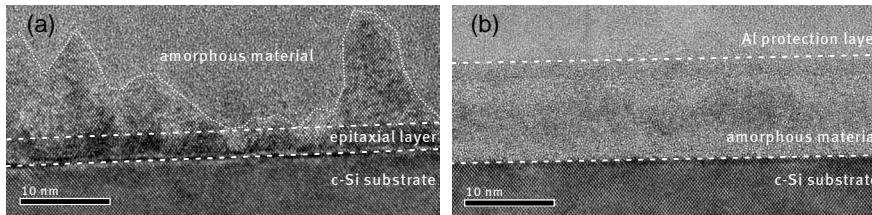


Figure 6: High resolution transmission electron microscopy (HR-TEM) images of two films deposited under identical conditions. (a) Shows a sharp interface between amorphous silicon and the hydrogen terminated crystalline silicon substrate (a), while (b) shows an epitaxial start of the growth process that is subsequently followed by a gradual breakdown to amorphous silicon growth. The epitaxial layer is approximately 20 Å thick. The lines are guides to the eye that indicate the location of the interfaces between the different materials.

excess hydrogen is probably not responsible for the increasing bandgap for ultrathin a-Si:H films. On the other hand, the observed bandgap shift as a function of the film thickness could be accurately fitted by a 1D quantum confinement model. Therefore, we suggest that the increase in bandgap observed for films with decreasing thickness is caused by quantum confinement effects of the electron wavefunction in the a-Si:H (Chapter 5).

After the exploratory work reported in Chapters 5 and 6, the investigations of the interface between hydrogen terminated silicon and a-Si:H were started. The last part of this section discusses recent experimental results on ultrathin a-Si:H films deposited on hydrogen terminated crystalline silicon that are not included in this thesis as a separate Chapter. In these experiments, we frequently observed an epitaxial start of the silicon growth process at substrate temperatures as low as 150 °C. This epitaxial layer breaks down to the amorphous phase at a certain thickness. However, an epitaxial thickness of ~20 Å, as is shown in the high resolution transmission electron microscopy (HRTEM) images in Fig. 6, is already undesirable for SHJ applications. Using spectroscopic ellipsometry and infrared absorption spectroscopy we were able to resolve the breakdown transition to amorphous silicon growth for epitaxial films when this occurred at a thickness larger than approximately 200 Å. However, these techniques were not able to distinguish between the two samples shown in Fig. 6, which is between an epitaxial or amorphous start of the growth process. In contrast, preliminary SHG measurements shown in Fig. 7 show a clear difference in real time behavior between these samples, which suggests that this technique is very well suited to detect breakdown of epitaxial growth to amorphous growth also for ultrathin films. For SHJ solar cells, that depend critically on the quality of the interface between the crystalline silicon wafer and the a-Si:H thin film, an *in situ* tool that can distinguish between epitaxial and amorphous initial

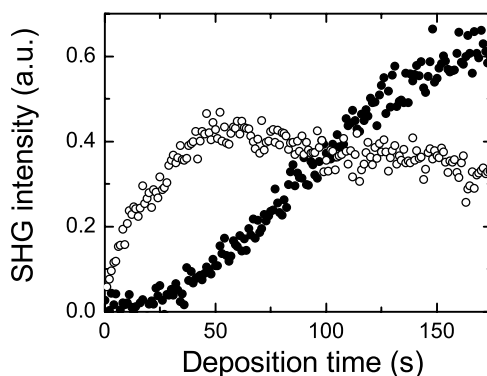


Figure 7: The second-harmonic (SHG) intensities observed during the deposition of the silicon films shown in Fig. 6. One film grows amorphous instantaneously (open dots), while the other starts to grow epitaxially (solid dots) and breaks down to amorphous growth after approximately 40 seconds. The growth conditions as well as surface pretreatment were identical for both films and the growth rate was approximately $30 \text{ \AA}/\text{min}$.

growth is very important. SHG could be such a diagnostic, but more experiments are needed to establish the ability to distinguish between epitaxial and amorphous initial growth further. Finally, these multi-diagnostic studies will contribute to the identification of the mechanisms behind epitaxial as well as amorphous silicon growth, resulting in better control of the interface formation between the silicon film and the crystalline silicon substrate.

IV. Outlook to the future

Crystalline silicon solar cells currently dominate the photovoltaic market and it is expected that they will continue to do so for at least a decade. To sustain the current developments in the solar cell field in terms of production volume growth and technological improvements, several challenges in the field of thin film and plasma processing need to be tackled. Bigger production systems with higher throughput are required to maintain the annual production volume growth for first generation, as well as second generation solar cell technology. Besides a higher throughput, significant innovation of manufacturing processes of crystalline silicon solar cells will take place in order to increase the conversion efficiency or decrease the production costs. The wet chemical etch processes used to create surface texture on the wafers and to remove the phosphorous glass after emitter diffusion can for instance be replaced by dry etch processes using plasmas. This will allow the combination of various process steps in one vacuum system, such as the phosphorous glass etch and the deposition

of the antireflection coating. Eventually, all process steps could be incorporated in an inline vacuum process, in which raw wafers enter and finished solar cells come out.

Apart from the innovations in the production technology, new cell concepts that incorporate functional layers for antireflection, surface passivation and light trapping will be introduced. To control the properties of these layers and the interfaces between them, fundamental studies (preferentially under well defined ultrahigh vacuum conditions) are necessary. Dedicated experimental studies will result in an improved understanding of the mechanisms responsible for surface passivation. In addition, they will lead to a better control of the interface that is created in the growth process. The multi-diagnostic approach to study the interface created in the growth of thin silicon films on crystalline silicon that was started in this work, has great potential to yield useful information about the interface quality as well as the growth process of amorphous and epitaxial silicon films. This generic approach is not limited to the model system of a-Si:H deposited on crystalline silicon wafers that was used in this study, but can also be applied to many other systems in which the properties of the interface between substrate and deposited film are under investigation.

References

- [1] M.A. Green, *Progress in Photovoltaics* **9**, 123 (2001).
- [2] http://www.bell-labs.com/news/2004/april/anniversary50_timeline.html
- [3] R.M. Swanson, *Progress in Photovoltaics* **14**, 443 (2006).
- [4] S.W. Glunz, *Solar Energy Materials and Solar Cells* **90**, 3276 (2006).
- [5] W.P. Mulligan, D.H. Rose, M.J. Cudzinovic, D.M. De Ceuster, K.R. McIntosh, D.D. Smith, and R.M. Swanson, *Nineteenth European–PVSEC*, p 387 (2004).
- [6] M. Taguchi, K. Kawamoto, S. Tsuge, T. Baba, H. Sakata, M. Morizane, K. Uchihashi, N. Nakamura, S. Kiyama and O. Oota, *Progress in Photovoltaics* **8**, 503 (2000).
- [7] M.A. Green, *Solar Energy* **74**, 181 (2003).
- [8] D.J. Eaglesham, H.–J. Grossmann, and M. Cerullo, *Phys. Rev. Lett.* **65**, 1227 (1990).
- [9] G. Hahn, and P. Geiger, *Progress in Photovoltaics* **11**, 341 (2003).
- [10] H. Du, C.H. Champness, and I. Shih, *Thin Solid Films* **480–481**, 37 (2005).
- [11] S. Hegedus, *Progress in Photovoltaics* **14**, 393 (2006).
- [12] M.A. Green, *Progress in Photovoltaics* **14**, 383 (2006).
- [13] M.A. Green, K. Emery, D.L. King, Y. Hishikawa, and W. Warta, *Progress in Photovoltaics* **14**, 455 (2006).
- [14] M.A. Green, *Third generation photovoltaics; Advanced Solar Energy* (Springer–Verlag, Berlin, 2003).
- [15] G. Conibeer, M. Green, R. Corkisch, Y.Cho, E–C. Cho, C–W. Jiang, T. Fangsuwannrak, E. Pink, Y. Huang, T. Puzzer, T. Trupke, B. Richards, A. Shalav, and K–L. Lin, *Thin Solid Films* **511–512**, 654 (2006).
- [16] Y. Chiba, A. Islam, Y. Watanabe, R. Komiya, N. Koide and L. Han, *Jap. J. Appl. Phys.* **45**, L638 (2006).
- [17] D.C. Schram and G.M.W. Kroesen, US Patent No. 4,871,580 (1989); European Patent No. 0297637 (1992)
- [18] B. Hoex, A. J. M. van Erven, R. C. M. Bosch, W. T. M. Stals, M. D. Bijker, P. J. van den Oever, W. M. M. Kessels, and M. C. M. van de Sanden, *Progress in Photovoltaics* **13**, 705 (2005).
- [19] J. Hong, W.M.M. Kessels, F.J.H. van Assche, H.C. Rieffe, W.J. Soppe, A.W. Weeber, and M.C.M. van de Sanden, *Progress in Photovoltaics* **11**, 125 (2003).
- [20] J. Hong, W.M.M. Kessels, W.J. Soppe, A.W. Weeber, W.M. Arnoldbik, and M.C.M. van de Sanden, *J. Vac. Sci. Technol. B* **21** (2003) 2123.
- [21] Y. Yan, M. Page, T.H. Wang, M.M. Al–Jassim, H.M. Branz, and Q. Wang, *Appl. Phys. Lett.* **88**, 101925 (2006).
- [22] S. De Wolf, and G. Beaucarne, *Appl. Phys. Lett.* **88**, 022104 (2006).

- [23] W.M.M. Kessels, R.J. Severens, A.H.M. Smets, B.A. Korevaar, G.J. Adriaansen, D.C. Schram, and M.C.M. van de Sanden, *J. Appl. Phys.* **89**, 2404 (2000).
- [24] F.W. Sexton, *Solar Energy Materials* **7**, 1 (1982).
- [25] C.C. Johnson, T. Wydeven, and K. Donohoe, *Solar Energy* **31**, 355 (1983).
- [26] M. Creatore, J.-C. Cigal, G.M.W. Kroesen, and M.C.M. van de Sanden, *Thin Solid Films* **484**, 104 (2005).
- [27] J.W.A.M. Gielen, P.R.M. Kleuskens, M.C.M. van de Sanden, L.J. van Ijzendoorn, D.C. Schram, E.H.A. Dekempeneer, J. Meneve, *J. Appl. Phys.* **80** 5986 (1996).
- [28] R. Groenen, J. Löffler, J.L. Linden, R.E.I. Schropp, and M.C.M. van de Sanden, *Thin Solid Films* **492**, 298 (2005).
- [29] M.C.M. van de Sanden, P.J. van den Oever, M. Creatore, M. Schaepekens, T. Miebach, C.D. Iacovangelo, R.C.M. Bosch, M. Bijker, M. Evers, D.C. Schram and W.M.M. Kessels, 47th Technical Conference Proceedings of the Society of Vacuum Coaters, p. 447 (2004).
- [30] http://www.otb-solar.com/products_dep.html.
- [31] E.E.T. project EETK99009 "Sunovation", ECN, Shell Solar, TNO, and Eindhoven University of Technology, <http://www.senternovem.nl/eet/projecten/sunovation.asp>.
- [32] B. Hoex, A.J.M. van Erven, M.D. Bijker, P.J. van den Oever, W.M.M. Kessels, M.C.M. van de Sanden, Proc. 20th European Photovoltaic Solar Energy Conference and Exhibition, Barcelona (2005)
- [33] M.D. Bijker, F.C. Dings, M.A.T. Hompus, W.M.M. Kessels, and M.C.M. van de Sanden, US Patent No. 6,946,404 (2005).
- [34] W.M.M. Kessels, J. Hong, F.J.H. van Assche, J.D. Moschner, T. Lauinger, W.J. Soppe, A.W. Weeber, D.C. Schram, and M. C. M. van de Sanden, *J. Vac. Sci. Technol. A* **20**, 1704 (2002).
- [35] B. Hoex, W.M.M. Kessels, M.D. Bijker, and M.C.M. van de Sanden, Proc. 21th European Photovoltaic Solar Energy Conference and Exhibition, Dresden, p. 435 (2006).
- [36] B. Hoex, F.J.J. Peeters, M. Creatore, M.A. Blauw, W.M.M. Kessels, and M.C.M. van de Sanden, *J. Vac. Sci. Technol. A* **24**, 1823 (2006).
- [37] B. Hoex, S.B.S. Heil, E. Langereis, M.C.M. van de Sanden, and W.M.M. Kessels, *Appl. Phys. Lett.* **89**, 042112 (2006).
- [38] B. Hoex, Ph.D. Thesis, to be published (2007).
- [39] P.J. van den Oever, M.C.M. van de Sanden, and W.M.M. Kessels, *Mat. Res. Soc. Sym. Proc.* **808**, 233 (2004).
- [40] A. Straaijer, M.H.W. Verbruggen, J.M.M. de Nijs, and H.H. Brongersma, *Rev. Sci. Instrum.* **64**, 1468 (1993).

- [41] R. Zijlmans, D.C. Schram, and R. Engeln, submitted for publication in *J. Phys. D.* (2007).
- [42] K. W. Busch and M. A. Busch, *Cavity–Ringdown Spectroscopy—An Ultratrace–Absorption Measurement Technique* (American Chemical Society, Washington, 1998).
- [43] G.J.H. Brussaard, M. van der Steen, C.M. Carrère, M.C.M. van de Sanden, and D.C. Schram, *Phys. Rev. E* **54**, 906 (1996).
- [44] J. Benedikt, S. Agarwal, D. Eijkman, W. Vandamme, M. Creatore, and M.C.M. van de Sanden, *J. Vac. Sci. Technol. A* **23**, 1400 (2005)
- [45] M.C.M. van de Sanden, J.M. de Regt, and D.C. Schram, *Plasma Sources Sci. Technol.* **3**, 501 (1994).
- [46] W.M.M. Kessels, C.M. Leewis, M.C.M. van de Sanden, and D.C. Schram, *J. Appl. Phys.* **86**, 4029 (1999).
- [47] A.J.M. Buuron, D.K. Otorbaev, M.C.M. van de Sanden, D.C. Schram, *Phys. Rev. E* **50**, 1383 (1994).
- [48] J.P.M. Hoefnagels, Y. Barrell, W.M.M. Kessels, and M.C.M. van de Sanden, *J. Appl. Phys.* **96**, 4094 (2004).
- [49] R. Engeln, S. Mazouffre, P. Vankan, D.C. Schram, and N. Sadeghi, *Plasma Sources Sci. Technol.* **10**, 595 (2001).
- [50] J.W.A.M. Gielen, W.M.M. Kessels, M.C.M. van de Sanden, and D.C. Schram, *J. Appl. Phys.* **82**, 2643 (1997).
- [51] M. Taguchi, M. Tanaka, T. Matsuyama, T. Matsuoka, S. Tsuda, S. Nakano, S. Kishi and Y. Kuwano, *Technical Digest of the International PVSEC–5* (Kyoto,1990) p.689.
- [52] M. Iwamoto, K. Minami, T. Yamaoki, United States Patent 5,066,340, November 19, 1991
- [53] H. Fujiwara, and M. Kondo, *Appl. Phys. Lett.* **90**, 013503 (2007).

PART I

Chapter 2

Density and production of NH and NH₂ in an Ar–NH₃ expanding plasma jet^{*}

The densities of NH and NH₂ radicals in an Ar–NH₃ plasma jet created by the expanding thermal plasma source were investigated for various source operating conditions such as plasma current and NH₃ flow. The radicals were measured by cavity ring–down absorption spectroscopy using the (0,0) band of the $A^3\Pi \leftarrow X^3\Sigma^-$ transition for NH and the (0,9,0)–(0,0,0) band of the $\tilde{A}^2A_1 \leftarrow \tilde{X}^2B_1$ transition for NH₂. For NH, a kinetic gas temperature and rotational temperature of 1750 ± 100 K and 1920 ± 100 K were found, respectively. The measurements revealed typical densities of $2.5 \times 10^{12} \text{ cm}^{-3}$ for the NH radical and $3.5 \times 10^{12} \text{ cm}^{-3}$ for the NH₂ radical. From the combination of the data with ion density and NH₃ consumption measurements in the plasma as well as from a simple 1–dimensional plasma simulation model, the key production reactions for NH and NH₂ are discussed.

^{*} Published as: P.J. van den Oever, J.H. van Helden, C.C.H. Lamers, R. Engeln, D.C. Schram, M.C.M. van de Sanden, and W.M.M. Kessels, *J. Appl. Phys.* **98**, 093301 (2005).

I. Introduction

Ammonia (NH_3) plasmas have widespread applications in research and industry for the (surface) treatment of materials. NH_3 plasmas are, for example, used for modifying the wettability and bio-compatibility of polymers [1–3], for improving the gas permeability of membranes [4], for inducing surface passivation of electronic devices [5,6], and for nitridation of dielectric and metallic materials [7,8]. Ammonia is also admixed in plasmas used for the synthesis of carbon nanotubes [9,10] and for ligand abstraction and nitridation during atomic layer deposition of metal nitrides [11–13]. One of the most important applications of NH_3 -based plasmas in industry to date is, however, the deposition of silicon nitride films. These films – generally deposited from ammonia–silane plasmas – have numerous applications, ranging from dielectric materials in the microelectronics industry to antireflection coatings for crystalline silicon-based photovoltaics [14,15] and encapsulation films for organic light emitting diodes [16].

Despite their widespread application, only few experimental studies on the plasma chemistry in NH_3 -based plasmas have been reported. Miller and Baird have addressed the plasma decomposition of NH_3 in radiofrequency plasmas [17], while Pringle and co-workers have addressed the ion-chemistry in a helical resonator [18]. These studies have not addressed the chemistry involved in ammonia radical production in detail. These radical species, however, are very likely most important during surface treatment. The interaction of NH and NH_2 plasma radicals with the surface of different materials has been addressed by Fisher and co-workers, using a molecular plasma beam in combination with laser-induced fluorescence for radical imaging [19–21]. Laser-induced fluorescence has also been used to determine the density of NH and NH_2 produced by NH_3 decomposition on a heated tungsten filament [22]. For deposition systems, few studies of the NH_3 plasma chemistry have been reported using primarily mass spectrometry (*e.g.* ammonia–silane chemistry for silicon nitride deposition [23,24] and recently also the ammonia–acetylene chemistry for carbon nanotube deposition [25]). In pure NH_3 plasmas as well as depositing plasmas based on NH_3 , the chemistry is very complex and much remains unknown about the NH_3 dissociation and its products.

To obtain more insight into the chemical reactions involved in the dissociation of NH_3 in plasmas, we have investigated the NH_3 dissociation process with respect to NH and NH_2 radical production. These studies were carried out using the expanding thermal plasma (ETP) technique, whose remote operation leads to a relatively simple chemistry, which facilitates plasma chemical investigations. Besides the technological relevance for NH_3 plasma surface treatment, the investigations can also be of astrophysical relevance [26,27]. Our particular interest lies, however, primarily

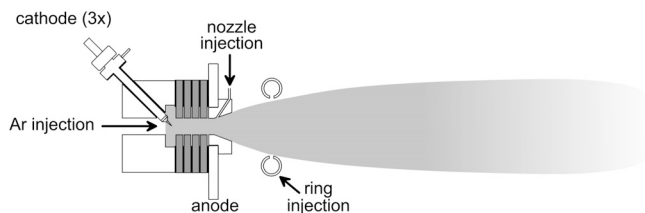


Figure 1: Schematic representation of the expanding Ar-NH₃ plasma jet.

in gaining a better understanding of the ultrahigh-rate deposition process of silicon nitride films by the expanding thermal plasma [15,28], in which silane is cracked by reactive ion and radical species (such as NH and NH₂) in the Ar-NH₃ plasma jet.

After presenting the basics of the ETP technique in Sec. II, we present the experimental details of the cavity ring-down measurements carried out to determine the NH and NH₂ radical densities (Sec. III). In the results section (Sec. IV), we present the measured NH and NH₂ radical densities as a function of NH₃ flow and current in the plasma source. Supported by data on the ion density and NH₃ consumption, we argue that NH₃ dissociation in the ETP technique is governed by Ar⁺ ions emanating from the plasma source. For NH, the key chemical reactions are charge transfer of NH₃ with Ar⁺ and dissociative recombination with electrons, while the NH₂ production appears to involve more reactions such as ion-molecule and H-abstraction reactions. This basic reaction mechanism is supported by a 1-dimensional plasma simulation model. The conclusions are presented in Sec. V.

II. Expanding Thermal Plasma setup

The Ar-NH₃ plasma jet is produced using the Expanding Thermal Plasma (ETP) technique described extensively in the literature (see *e.g.* Ref. 29 and 30). As shown in Fig. 1, this technique uses a cascaded arc plasma source to produce an Ar plasma at sub-atmospheric pressure (typically 400 kPa). In the cascaded arc, a dc current is drawn between three cathodes and one common grounded anode through a narrow (4 mm diameter) channel filled with argon gas. The cathode region and anode are separated by several “cascaded plates”, which are at floating potential. The plasma expands supersonically through a conically shaped nozzle into a low-pressure reactor (typical pressure is 20 Pa), and after a stationary shock at approximately 5 cm from the nozzle, the expansion continues sub-sonically. When going from supersonic to subsonic expansion, the directed velocity of the plasma changes from ~1800 m/s to ~600 m/s. In the downstream region the electron temperature (~0.3 eV) is low, which can be attributed to the expansion and to the fact that no electrical power is

coupled into the plasma in that region. Precursor gases can be injected into the Ar plasma jet, either through a slit in the nozzle or through an injection ring situated downstream in the jet.

In the present experiment, the plasma source is operated at a pure Ar flow of 55 standard cm^3s^{-1} (sccs), and the current through the arc channel is controlled between 30 and 70 A with a typical voltage of 40 V. The expanding Ar plasma was characterized in detail in our previous work and a brief description of some of the key findings is given here. In the downstream region, the Ar^+ ion and electron density are in the order of 10^{13} cm^{-3} . The metastable argon density Ar^m is directly linked to the ion density but is typically lower by a factor of 10 [31]. From the combination of radial ion density measurements and the forward velocity in the expansion, the equivalent flow of Ar^+ ions emanating from the source is estimated. For a current of 45 A, we found an “ Ar^+ ion flow” of 2–3 sccs, corresponding to an average Ar ionization degree of ~5% in the plasma source. Furthermore, the Ar^+ ion flow increases linearly with the plasma current for a constant Ar flow through the source [29,30].

Two injection locations of NH_3 are used: NH_3 is either injected in the nozzle before the expansion or ~8 cm downstream the expansion via a stainless steel injection ring. The NH_3 flow range used is 0.5–17 sccs, and the downstream pressure is kept constant at 20 Pa by adjusting the gate valve to the pump. A substrate holder is positioned downstream at ~39 cm from the source. Furthermore, besides the cavity ring–down system that will be discussed in detail in the next section, the setup is also equipped with a Langmuir probe [29], that can measure ion and electron densities at ~36 cm downstream from the source, and a residual gas analyzer for basic mass spectrometry measurements, which is situated at ~56 cm from the source in the plasma beam.

III. Cavity ring–down spectroscopy on NH and NH_2

Cavity ring–down spectroscopy (CRDS) [32] was used to measure the density of the NH and NH_2 radicals in the downstream plasma at a position of 36 cm from the source. Briefly, CRDS is based on the injection of a laser pulse in a stable optical resonator (cavity) that consists of two high reflectivity mirrors. The decay rate of the light inside the resonator is detected through one of the mirrors. Cavity ring–down prevents the most common limitation of absorption measurements as the decay rate is independent of the intensity of the light pulse and is therefore not affected by pulse–to–pulse energy fluctuations of the laser system. For an “empty” cavity, this decay rate is simply determined by the reflectivity of the mirrors and the cavity length, but the decay rate becomes faster when absorbing (or scattering) species are present in the cavity. From the difference in decay rate between these two conditions, the

absorption due to the species in the cavity can be determined. Consequently, the number density of the species can be calculated when information on the cross section and absorption path length is available.

The cavity used in the present work consisted of plano-concave mirrors with a 100 cm radius of curvature and 2.5 cm diameter, placed 112 cm apart on flexible bellows. In front of the mirrors an Ar flow was injected to protect the mirrors from reactive plasma species. The NH radical was detected using high-reflectivity mirrors with a optimum reflectivity at 340 nm (Laser-Optik, $R = \sim 0.998$), while for the NH₂ radical detection the optimum reflectivity was at 560 nm (Laser-Optik, $R = \sim 0.999$). Laser light pulses were generated by a Sirah PrecisionScan-D dye laser pumped by the second-harmonic of a Spectra-Physics GCR-4 Nd:YAG laser working at a repetition rate of 10 Hz. For NH detection, Pyridine 1 laser dye was used to create ~ 680 nm light, which was subsequently frequency doubled to ~ 340 nm by a KDP crystal. For NH₂ detection, the ~ 600 nm output of the dye laser operated on Rhodamine B laser dye was directly used. To avoid saturation of the transition of interest the amplifier stage of the dye laser was not used in the latter case. The laser intensity was further reduced by a set of filters while a UV attenuator was used for the 340 nm laser light. The typical pulse energy in front of the cavity was 100 μ J/pulse. Detection took place by means of a photomultiplier tube (Hamamatsu R928) at the other cavity mirror through a narrow bandpass filter, which blocked the plasma light. For every laser shot the photomultiplier signal was processed separately by a 100 MHz, 12 bits data acquisition system (TU/eDACS [33]). All decay rates were single-exponential and were analyzed by a weighted least squares fit of the logarithm of the transient data. To improve the signal-to-noise ratio an average of 20 ring-down times was taken for all measurements. The absorption loss by the radicals was determined from the difference in decay rate in a pure Ar plasma and an Ar-NH₃ plasma. If necessary, a minor baseline correction was carried out to account for small changes in mirror reflectivity. For the NH₂ measurements an oscillating behavior of the baseline signal was observed (which is common for mirrors in the wavelength range around 600 nm [34]) that hampered the baseline correction procedure and resulted in a slightly lower experimental accuracy compared to the NH measurements.

The NH radical was detected on the (0,0) band of the $A^3\Pi \leftarrow X^3\Sigma^-$ transition around 340 nm, as shown in Fig. 2(a) [35,36]. Apart from transitions of the (0,0) band, this spectrum also shows some hot band transitions of the (1,1) band. The rotational temperature of NH was extracted from the Boltzmann plot shown in Fig. 3(a), in which the statistically-weighted integrated absorptions $A_{int}(K)/(2K+1)$ obtained from the spectrum are plotted as a function of the rotational energy. In this expression, K is the rotational quantum number. This procedure yields a NH rotational temperature of 1920 ± 100 K. For the density measurements, the "isolated" $P_{33}(9)$ absorption line at

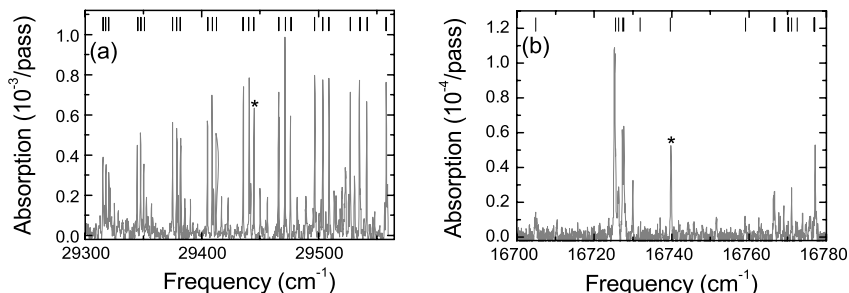


Figure 2: Spectra of (a) NH and (b) NH₂ as measured with cavity ringdown spectroscopy. A plasma source current of 45 A and a NH₃ flow of 5 sccs are used for the measurements of the spectra. The absorption line positions reported in the literature are indicated in the upper part of the graphs, as are the absorption lines used for the density measurements (marked by an asterisk).

339.62 nm (29444.28 cm⁻¹) was used, as indicated in the spectrum in Fig. 2(a). The density information is determined by scanning the laser over the absorption line and using the integrated absorption cross section, which is calculated from the oscillator strength reported in literature [36]. For the integrated absorption cross section a value of $8.3 \times 10^{-21} \text{m}^2 \text{cm}^{-1}$ was found for the absorption line under investigation (see Appendix A). This method is insensitive to the laser linewidth and the Doppler broadening effect. Doppler broadening was used to determine the kinetic gas temperature of the NH radicals by deconvoluting the experimental absorption lines into a Lorentzian laser linewidth and Gaussian Doppler contribution. This procedure, carried out on a set of distinct measurements, yielded a laser linewidth of $0.11 \pm 0.01 \text{cm}^{-1}$ at a wavelength of 29444 cm⁻¹ and a NH kinetic gas temperature of $1750 \pm 90 \text{K}$ with no clear dependence on the NH₃ flow, as can be seen in Fig. 3(b). The laser linewidth is also consistent with the manufacturer’s specifications [37] and with earlier data obtained for this laser system [33]. The NH kinetic gas temperature is in fair agreement with the rotational temperature and it reflects the gas temperature in the plasma expansion as thermalization occurs quickly under the conditions used. The gas temperature is also in good agreement with previous measurements in plasmas of different gas mixtures [33]. The NH₂ radical was detected at the (0,9,0)–(0,0,0) band of the $\tilde{A}^2A_1 \leftarrow \tilde{X}^2B_1$ transition at ~597 nm [38,39] as shown in Fig. 2(b) and the “isolated” ${}^P Q_{1,N}(7)$ absorption line at 597.38 nm (16739.90 cm⁻¹)* was used for the density measurements using a procedure similar to the one for NH. From the

* This absorption line is in fact a spin doublet that is not resolved by the measurements.

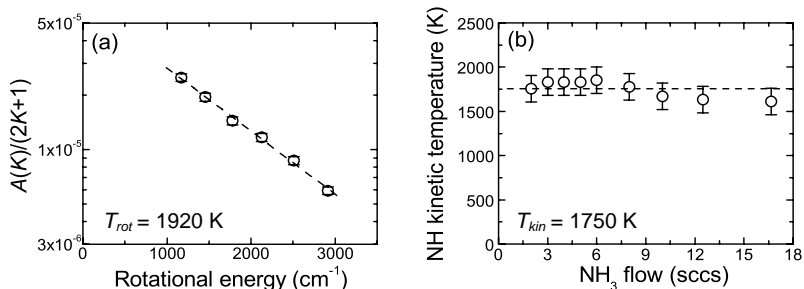


Figure 3: (a) The statistically-weighted integrated absorptions $A_{int}(K)/(2K+1)$ for several rotational lines (P_{33} branch) of the (0,0) band of the $A^3\Pi \leftarrow X^3\Sigma^-$ transition of NH as a function of the rotational energy. The rotational temperature was determined from the slope of the linear fit (dashed line). (b) The kinetic temperature of the NH radical determined from the Doppler broadening of the $P_{33}(9)$ absorption line on the (0,0) band of the $A^3\Pi \leftarrow X^3\Sigma^-$ transition as a function of the injected NH_3 flow. The dashed line represents the average value.

oscillator strength [39] an integrated absorption cross section of $7.4 \times 10^{-21} \text{m}^2 \text{cm}^{-1}$ was deduced for this particular absorption line.

The total NH and NH_2 densities were calculated by taking into account the densities in all possible states assuming a Boltzmann rotational distribution and a rotational temperature of 1750 K. For NH and NH_2 , the density in the hotbands was also taken into account by assuming equal temperatures for rotation and vibration and using the vibrational energies reported in the literature [35,40]. The density in the hotbands is approximately 8% of the total density for NH and approximately 39 % for NH_2 . In the Appendix the derivation of the integrated absorption cross sections and the calculation of the corresponding total densities of NH and NH_2 are given. The largest uncertainty in the absolute values of the densities reported is generated by the assumption about the absorption path length for the radicals in the plasma, which is estimated to be 30 cm [41]. This error can be as large as a factor of three for the local absolute densities. Finally, it is important to note that optical saturation can be neglected for both NH and NH_2 as was verified by measuring the absorption line-intensities for both radicals as a function of the laser energy coupled into the cavity.

IV. NH and NH_2 densities and plasma chemistry

Figure 4 shows the absolute densities of the NH and NH_2 radicals and the NH_3 molecules in the expanding Ar- NH_3 plasma as a function of the NH_3 flow injected through the injection ring. The argon flow used is 55 sccs, the arc current is 45 A, and

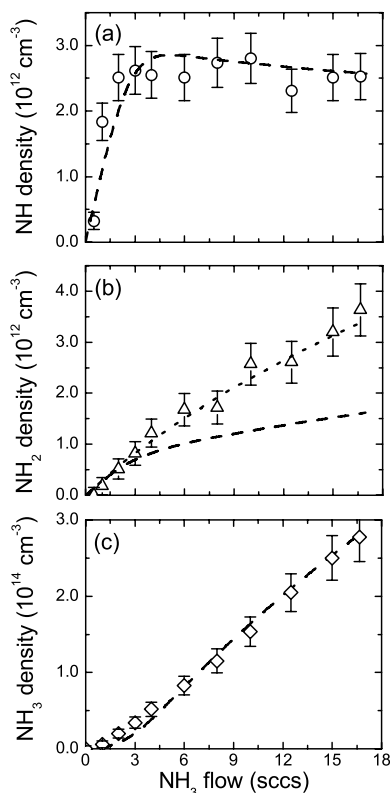


Figure 4: (a) The NH, (b) NH₂ and (c) NH₃ density as a function of the injected NH₃ flow. The NH and NH₂ density was measured by cavity ringdown spectroscopy, while the NH₃ density was calculated from the partial NH₃ density taking into account its consumption as measured by mass spectrometry. The dashed lines are simulation results from a simple 1-dimensional plug down model using literature values for the reaction rates. The dotted line shows the modeled NH₂ density when the rate of reaction R4 ($\text{NH}_3 + \text{H} \rightarrow \text{NH}_2 + \text{H}_2$) is set to a value that is a factor of 7.5 higher than reported in the literature. For this higher rate, no change in the modeled NH density is observed, while the change in the modeled NH₃ density is also negligible.

the downstream pressure is 20 Pa. The radicals were measured at 36 cm from the plasma source whereas the NH₃ density is calculated from the partial NH₃ density taking into account its consumption as measured by mass spectrometry at 56 cm from the plasma source. The NH density increases rapidly with increasing NH₃ flow and saturates at a level of $\sim 2.5 \times 10^{12} \text{ cm}^{-3}$ for NH₃ flows greater than 3 sccs. Initially, also the NH₂ density increases fast with the NH₃ flow, but for flows higher than 3 sccs the NH₂ density increases more gradually. The NH₂ density shows no saturation and reaches a maximum level of $\sim 3.5 \times 10^{12} \text{ cm}^{-3}$ for the experimental conditions used. The

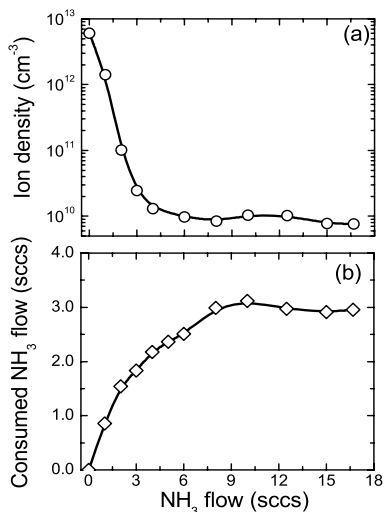


Figure 5: (a) The ion density and (b) the equivalent flow of consumed NH₃ as a function of the NH₃ flow. The ion density was measured by means of Langmuir probe measurements and the consumed NH₃ flow was determined by means of mass spectrometry experiments. The lines serve as a guide to the eye.

NH₃ density increases almost linearly with the NH₃ flow showing a deviation at low NH₃ flows, where the consumption of NH₃ in the plasma is significant [see Fig. 5(b)]. The maximum NH₃ density is approximately $3 \times 10^{14} \text{ cm}^{-3}$, which is substantially higher than the NH and NH₂ densities. Within the experimental accuracy, we obtained similar results for both ring injection and nozzle injection of NH₃.

The dissociation of NH₃ is ruled by reactive species emanating from the plasma source, such as Ar⁺, metastable argon atoms, Ar^m, and electrons. In the following, we show that argon ions most likely govern the dissociation of NH₃, as is the case in most plasma processes using the ETP source operated on argon. Electron-induced dissociation and ionization of NH₃ are not very important due to the low electron temperatures (~0.3 eV) in the expanding thermal plasma. Figure 5(a) shows the ion density determined by Langmuir probe measurements for an arc current of 45 A. The ion density (and electron density) in a pure Ar plasma is very high* and corresponds to an Ar⁺ flow emanating from the source of 2–3 sccs [29,30].

* The ion density decreases exponentially downstream due to the very effective charge transfer reactions of the ion with the injected NH₃ molecules, followed by very fast dissociative recombination of the resulting molecular ion.

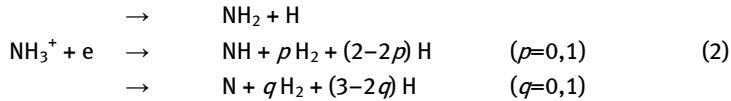
Table 1: Reactions and rate constants.

	Reaction	Branching ratio	Rate constant (cm ³ s ⁻¹)	Ref.
R1	Ar ⁺ + NH ₃ → Ar + NH ₃ ⁺ → Ar + NH ₂ ⁺ + H → ArH ⁺ + NH ₂	87% 7% 6%	1.84×10 ⁻⁹	[44]
R2	NH ₃ ⁺ + e → NH ₂ + H → NH + p H ₂ + (2-2p) H (p=0,1) → N + q H ₂ + (3-2q) H (q=0,1)	- - -	1.8×10 ^{-7*}	[45]
R3	NH ₃ ⁺ + NH ₃ → NH ₄ ⁺ + NH ₂		1.8×10 ⁻⁷	[49]
R4	NH ₃ + H → NH ₂ + H ₂		4×10 ⁻¹² (3×10 ⁻¹¹) [†]	[48]
R5	NH ₄ ⁺ + e → NH ₃ + H → NH ₂ + H + H → NH ₂ + H ₂	85 % (69 %) [€] 13 % (21 %) 2 % (10 %)	1.8×10 ^{-7§}	[50,42]
R6	NH ₂ ⁺ + e → NH + H → N + H + H → N + H ₂	34 % 66 % 0 %	1.8×10 ^{-7§}	[42]
R7	NH ⁺ + e → N + H		1.8×10 ^{-7§}	
R8	ArH ⁺ + e → Ar + H		1.8×10 ^{-7§}	[43]

When NH₃ is injected downstream in the plasma, the ion density decreases drastically until it has decreased about three orders of magnitude for NH₃ flows >3 sccs. This drastic decrease of the ion density can be attributed mainly to the reaction mechanism, in which Ar⁺ ions undergo charge transfer reactions with NH₃ producing predominantly NH₃⁺ (for other branching products see Table 1):



with a reaction rate constant of 1.84×10⁻⁹ cm³s⁻¹ [44]. Subsequently, the molecular ions produced recombine dissociatively with electrons,



* Estimated rate constant for dissociative recombination reactions.

† This value is used in the model calculations shown by the dotted line in Fig. 4(b).

€ In the model, the branching ratios reported in Ref. 50 were used. These are in fair agreement with earlier results reported in Ref. 42 that are denoted between brackets.

These dissociative recombination reactions typically have a rate constant of $1 \times 10^{-7} \hat{T}_e^{1/2} \text{ cm}^3 \text{ s}^{-1}$, [45] which leads to a rate of $1.8 \times 10^{-7} \text{ cm}^3 \text{ s}^{-1}$ for an electron temperature \hat{T}_e of 0.3 eV. The combination of these two reactions with their high reaction rates explains the very fast decrease in ion density when going from a pure Ar plasma to an Ar–NH₃ plasma. Penning ionization of NH₃ by argon metastables is not important because the Ar^m density in the expanding thermal plasma is typically more than a factor of 10 lower than the density of Ar⁺ ions* [31], and the reaction rate ($4.2 \times 10^{-11} \text{ cm}^3 \text{ s}^{-1}$ [46]) is also considerably smaller than the one of reaction (1).

More evidence for the fact that the argon ions dominate the NH₃ dissociation is obtained by considering the consumed NH₃ flow, which is calculated by multiplying the relative NH₃ consumption with the injected NH₃ flow. Figure 5(b) shows that the consumed NH₃ flow saturates at ~3 sccs, which is, within the experimental accuracy, slightly higher or equivalent to the Ar⁺ ion flow emanating from the plasma source (See Sec. II). The NH₃ consumption saturates relatively slowly (for a NH₃ flow of ~7 sccs), which might indicate that a small amount of the NH₃ is dissociated by radicals produced by the initial NH₃ dissociation reactions. For completeness, we also mention that pyrolysis of NH₃ molecules due to the relatively high plasma temperatures can be neglected as this reaction has a rate constant below $1 \times 10^{-18} \text{ cm}^3 \text{ s}^{-1}$ for a gas temperature of 1750 K [47]. For this gas temperature, also the dissociation of NH₃ by hydrogen atoms, which are produced by other NH₃ dissociation reactions, does not seem to play a significant role based on its relatively low reaction rate of $\sim 4 \times 10^{-12} \text{ cm}^3 \text{ s}^{-1}$ [48], but this reaction will be re-considered below.

To further test our hypothesis that the NH₃ dissociation is dominated by Ar⁺ ions, we measured the NH and NH₂ densities for varying Ar⁺ ion flow from the ETP source by changing the plasma current. The argon ion flow is approximately linear with the plasma current and ranges from ~1.6 sccs at a current of 30 A to ~5 sccs at a current of 70 A. Figure 6(a) shows the NH and NH₂ densities as a function of the plasma current for high NH₃ flows (such that NH₃ is abundantly present and therefore not a limiting factor), and Fig. 6(b) shows the consumed NH₃ flow calculated from mass spectrometry data. Taking into account the experimental uncertainty in the measured Ar⁺ flow, both the NH density and the consumed NH₃ flow increase linearly with the Ar⁺ flow reaching a density of $\sim 5 \times 10^{12} \text{ cm}^{-3}$ and a consumed flow of ~6 sccs,

* Argon metastables, Ar^m, in a pure Ar plasma are produced downstream by 3-particle recombination of Ar+ with electrons. When molecular gases are admixed, this reaction channel for Ar⁺ loss is highly unlikely and therefore the Ar^m density is lower than the Ar⁺ density by more than a factor 10.

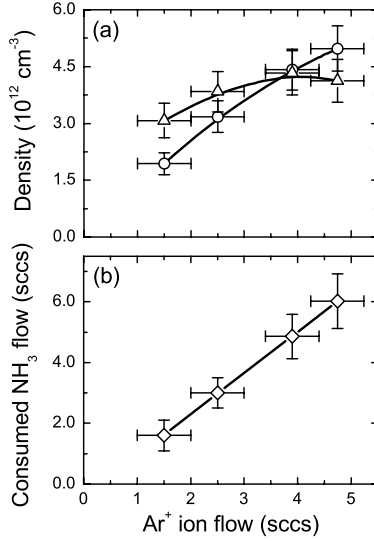


Figure 6: (a) The NH (circles) and NH₂ (triangles) density and (b) the consumed NH₃ flow as a function of the Ar⁺ ion flow emanating from the plasma source. The lines serve as a guide to the eye.

respectively. The NH₂ density, however, increases initially and subsequently remains constant at $\sim 4 \times 10^{12} \text{ cm}^{-3}$.

The NH density shows a first order dependence on the Ar⁺ flow. This behavior can be explained by NH production via the reaction sequence given by reactions (1) and (2). Furthermore, the NH radicals are not lost in gas phase reactions with NH₃ as can be deduced from the saturation of the NH density as a function of the NH₃ flow in Fig. 4. The density of the NH₂ radical on the other hand shows a less pronounced dependence on the Ar⁺ flow. This suggests that the generation of NH₂ radicals is controlled by a different reaction mechanism than the production of NH radicals. A reaction that can play a significant role in the production of NH₂ is the reaction between ammonia ions and molecules,



which has a reaction rate of $1.7 \times 10^{-9} \text{ cm}^3 \text{ s}^{-1}$ [49]. For high NH₃ flows, when the ion and electron densities are significantly reduced, this reaction becomes competitive with the dissociative recombination reaction of NH₃⁺. On the basis of the reaction rates, it can be deduced that this will happen when the ratio of the electron density over the NH₃ density is below ~ 0.01 (*i.e.*, for a NH₃ flow of $> \sim 3$ sccs). This reaction might therefore explain the gradual increase in the NH₂ density for higher NH₃ flows, which is not observed for the NH density. The NH₄⁺ ion formed in this reaction can also

recombine dissociatively with electrons, mainly leading to $\text{NH}_3 + \text{H}$ and to a somewhat lesser extent to NH_2 and 2H [50].

The feasibility of the proposed reaction pathway is investigated by a 1-dimensional plasma simulation model. For the type of plasma expansions addressed in this study, such plasma simulation models have been very valuable in gaining insight into the plasma chemistry [51,52]. In the 1-dimensional model, the species in the expansion region are produced and consumed by reactions in a forward chemistry as a function of the axial position from the plasma source. The initial conditions are set in terms of the initial ion and NH_3 flows, and it is assumed that the forward velocity and beam diameter are constant. Furthermore, we want to stress that no recirculation of background gas species is included, while also no reactions of species at the reactor walls are explicitly taken into account. Table 1 shows the reactions that are included in the model with the corresponding reaction rates taken from the literature. For the dissociative recombination reactions, a rate of $1.8 \times 10^{-7} \text{ cm}^3 \text{ s}^{-1}$ has been assumed as discussed earlier. The model results are shown by the dashed lines in Fig. 4 and the trends for NH and NH_3 show a good agreement with the experimental data. For NH_2 , however, the model predicts significantly lower NH_2 densities at high NH_3 flows compared to experimental results.

In the model, the branching ratio of the dissociative recombination reaction of NH_3^+ (reaction 2), which is not known in the literature, was set to 80% NH production and 20 % NH_2 production, neglecting the channel resulting in N radicals. This ratio was primarily chosen to reproduce the experimental NH density. Setting the branching ratio to a different value cannot account for the observed NH_2 increase for high NH_3 flows. Also reaction (3) was taken into account in the model, but it cannot fully explain the observed increase of the NH_2 density for high NH_3 flows whereas changes in the rate constant of this reaction will affect the modeled NH density significantly. Therefore, another reaction seems to play an important role in the NH_2 production for high NH_3 flows. Although several reactions might contribute to the NH_2 density, we have focused on the reaction of NH_3 with atomic H :



which has a rather low rate constant of $4.0 \times 10^{-12} \text{ cm}^3 \text{ s}^{-1}$ [48] for ground state reactants. However, this rate might be substantially higher in the presence of energetic atomic H and ro-vibrationally excited NH_3^{IV} . In our case, energetic atomic H is primarily produced as a product of the exoergic dissociative recombination reactions in the NH_3 dissociation process, while dissociative recombination of NH_4^+ probably yields NH_3^{IV} [50]. Therefore, reaction (4) is expected to be a good candidate to explain the discrepancy between the modeled and experimental NH_2 densities. When reaction (4) is implemented in the model, good agreement with the experimental data can be achieved for a reaction rate that is a factor of 7.5 higher

than the literature value (see Fig. 4). Such an enhancement in reaction rate seems not inconceivable. Reaction (4), as a reaction between NH_3 and atomic H produced from other NH_3 dissociation reactions, might also explain the fact that the consumed NH_3 flow appears to be slightly higher than the Ar^+ ion flow from the plasma source [see Fig. 6(b)] as well as the slow saturation of the consumed NH_3 flow [see Fig. 5(b)].

From the above, it can be concluded that good agreement between the experimental data and the results of a simple plasma simulation model can be obtained by including the reactions in Table 1 and the corresponding rates reported in the literature. Only to explain the production of NH_2 a higher rate constant for reaction (4) was used. However, we stress that in the model not all possible reactions have been considered. For example, the reactions of NH and NH_2 with NH_3 , with themselves, and with other plasma radicals have not been addressed. This seems to be justified on the basis of the reaction rates reported [46] and the (expected) radical densities. Also the surface loss of radicals has not been addressed, as no data are available for the surface reactivity of NH and NH_2 on the stainless steel reactor walls. However, from the data of Fisher and co-workers [19–21] it seems that the radicals are not very reactive with the surface. Finally, from the radical densities and NH_3 consumption measured, it can be inferred that a significant amount of the consumed NH_3 flow has to be converted into other stable species in the plasma, such as N_2 and H_2 molecules. These and other aspects will be addressed in future studies, while the NH and NH_2 density will also be investigated for the ammonia–silane plasma to address the importance of NH and NH_2 for silicon nitride film growth.

V. Conclusions

The dissociation of NH_3 in an expanding Ar– NH_3 plasma jet created by the ETP technique was investigated with respect to NH and NH_2 radical production. The NH and NH_2 radicals were measured by cavity ring–down spectroscopy for different NH_3 flows and plasma source currents. For NH, densities up to $\sim 5 \times 10^{12} \text{ cm}^{-3}$ were found when using a high NH_3 flow and plasma source current. The maximum density of NH_2 is $\sim 4 \times 10^{12} \text{ cm}^{-3}$. By combining the NH and NH_2 density information with ion density and NH_3 consumption measurements, it was concluded that NH is directly produced through Ar^+ ions from the source in a charge transfer and dissociative recombination reaction. The situation for NH_2 is more complex and appears to involve ion–molecule reactions between NH_3^+ and NH_3 and possibly H–abstraction of NH_3 by atomic H. The results were based on and corroborated by a simple 1–dimensional plasma simulation model, which captures the key plasma chemical reactions in terms of NH and NH_2 production in the plasma. Furthermore, from the cavity ring–down

measurements a kinetic gas temperature and rotational temperature of 1750 ± 100 K and 1920 ± 100 K were found for NH, respectively.

Acknowledgements

The authors thank M.J.F. van de Sande, J.F.C. Jansen, A.B.M. Hüsken, and H.M.M. de Jong for their skillful technical assistance. This study has been supported by the Netherlands Foundation for Fundamental Research on Matter (FOM) and by the Netherlands Ministry of Economic Affairs, the Ministry of Education, Culture and Science and the Ministry of Public Housing, Physical Planning and Environment (E.E.T.-project "HR-CEL"). The research of W.K. has been made possible by a fellowship of the Royal Netherlands Academy of Arts and Sciences (KNAW).

Appendix: Integrated absorption cross sections of NH and NH₂

A. Cross section of the $A^3\Pi(v'=0)\leftarrow X^3\Sigma^-(v''=0)P_{33}(9)$ transition of NH at 29444.277 cm^{-1}

For NH the integrated cross section can be calculated from the Einstein coefficient for spontaneous emission on the basis of information reported by Lents [36] and Schadee [53]. The integrated absorption cross section of a molecule σ_{int} can be directly related to the Einstein coefficient for spontaneous emission A_{ki} [54]:

$$\sigma_{int} = \int \sigma_{ik}(\nu) d\nu = \frac{g_k}{g_i} \frac{c^2}{8\pi\nu^2} A_{ki}, \quad (\text{A1})$$

where c is the speed of light, g_i and g_k are the degeneracies of the lower i and upper level k and ν is the transition frequency. Subsequently, the Einstein coefficient for emission A_{ki} can be related to the electronic–vibrational transition probability A_{00} by the following expression [36]:

$$A_{ki} = A_{00} \frac{P_{33}(J)}{g'_e (2(J-1)+1)(2S'+1)}, \quad (\text{A2})$$

where $P_{33}(J)$ is the Hönl–London factor for lines in the P_{33} branch of the $A^3\Pi \leftarrow X^3\Sigma^-$ transition, g'_e is the electron degeneracy of the upper level, S' is the total spin of the upper state and J is the quantum number of the total angular momentum of the lower level. In the subsequent derivation, singly primed coefficients pertain to the upper Π state and doubly primed quantities to the lower Σ state. The Hönl–London factor $P_{33}(J)$ is given by Schadee [53]:

$$P_{33}(J) = \frac{(J-1)(J+1) \left\{ (J-2)u'_{3+}(J-1)g''(J) + 4(J-1)\sqrt{J(J+1)}s''(J) + Ju'_{3-}(J-1)g''(J) \right\}^2}{8Jc'_3(J-1)} \quad (\text{A3})$$

with the following coefficients:

$$g(J) = \left(\frac{F_2(J) - F_1(J)}{F_3(J) - F_1(J)} \right)^{\frac{1}{2}}, \quad (\text{A4})$$

$$s(J) = \left(\frac{F_3(J) - F_2(J)}{F_3(J) - F_1(J)} \right)^{\frac{1}{2}}, \quad (\text{A5})$$

$$u_{3+}(J) = \left[(\gamma-2)^2 + 4J(J+2) \right]^{\frac{1}{2}} + (\gamma-2), \quad (\text{A6})$$

$$u_{3-}(J) = \left[(\gamma-2)^2 + 4J(J+2) \right]^{\frac{1}{2}} - (\gamma-2), \quad (\text{A7})$$

$$C_3(J) = Y(Y-4)(J-1)(J+2) + 2(2J+1)J(J+1)(J+2) - (Y-2) \left[(Y-2)^2 + 4J(J+2) \right]^{\frac{1}{2}} + Y(Y-4) - 4(J+1), \quad (\text{A8})$$

$$F_2(J) - F_1(J) = \left[(B_v - \frac{1}{2}\gamma - \lambda)^2 + 4J(J+1)(B_v - \frac{1}{2}\gamma)^2 \right]^{\frac{1}{2}} - (B_v - \frac{1}{2}\gamma - \lambda) \quad (\text{A9})$$

$$F_3(J) - F_2(J) = \left[(B_v - \frac{1}{2}\gamma - \lambda)^2 + 4J(J+1)(B_v - \frac{1}{2}\gamma)^2 \right]^{\frac{1}{2}} + (B_v - \frac{1}{2}\gamma - \lambda), \quad (\text{A10})$$

$$F_3(J) - F_1(J) = 2 \left[(B_v - \frac{1}{2}\gamma - \lambda)^2 + 4J(J+1)(B_v - \frac{1}{2}\gamma)^2 \right]^{\frac{1}{2}}. \quad (\text{A11})$$

The molecular constant γ represents the spin-rotation interaction, λ is the splitting constant, B_v the rotational constant, and Y represents the coupling between the nuclear spin S and the orbital angular momentum L . The electron degeneracies of the Σ and Π states are $2(2S+1)$ and $2(2S+1)$ respectively [55]. Using the molecular constants of the electronic states ($A^3\Pi$ and $X^3\Sigma^-$) of the NH radical reported by Brazier *et al.* [35] and the electronic-vibrational transition probability A_{00} reported by Lents [36], we can calculate the Einstein coefficient for emission of the $P_{32}(J=9)$ line:

$$A_{ki} = 6.07 \times 10^4 \text{ s}^{-1} \quad (\text{A12})$$

Using Eq. (A1) and $g_k = 2(J-1)+1$ and $g_i = 2J+1$ with $J=9$ we find for the integrated absorption cross section:

$$\sigma_{int} = 2.49 \times 10^{-10} \text{ m}^2 \text{ Hz}. \quad (\text{A13})$$

The peak absorption cross section for a gas temperature T can now be calculated by incorporating the Gaussian lineshape function $\Phi(0,a)$ that depends on the pressure broadening parameter a [39,47]:

$$\sigma_{peak} = \sigma_{int} \Phi(0,a). \quad (\text{A14})$$

For the low working pressures in our experimental conditions, pressure broadening is negligible [56] and $\Phi(0,a)$ can be written as a function of the Doppler width $\Delta\nu_D$:

$$\Phi(0,a) = \sqrt{\frac{4\ln 2}{\pi}} \frac{1}{\Delta\nu_D}. \quad (\text{A15})$$

$\Delta\nu_D$ is the full width at half maximum of the Doppler broadened line profile and can be written as:

$$\Delta\nu_D = \frac{\nu}{c} \sqrt{\frac{8kT\ln 2}{m}} = 7.16 \times 10^{-7} \nu \sqrt{\frac{T}{M}}, \quad (\text{A16})$$

with k Boltzmann's constant, m the mass of the NH molecule, T the gas temperature (in Kelvin) and M the molar mass of NH. This formula results in a peak absorption cross section of the $A^3\Pi(\nu'=0) \leftarrow X^3\Sigma^-(\nu''=0) P_{33}(9)$ line at $T=1750$ K of:

$$\sigma_{peak} = 3.43 \times 10^{-20} \text{ m}^2. \quad (\text{A17})$$

The density of NH in the $A^3\Pi(v'=0) \leftarrow X^3\Sigma^-(v''=0)P_{33}(9)$ transition can be calculated from measured integrated absorption A_{int} :

$$n_{NH,J=9} = \frac{A_{int}}{\sigma_{int} l}, \quad (\text{A18})$$

where l is the length of the absorption path in the cavity (30 cm). Assuming a Maxwell–Boltzmann distribution for densities in the rotational and vibrational states, we can calculate the total NH density:

$$n_{NH} = \frac{n_{NH,J=9}}{f_b}, \quad (\text{A19})$$

where the f_b is the Boltzmann fraction which is taken from Herzberg [57]:

$$f_b = \frac{2J+1}{Q_r Q_v} \exp\left[-\frac{E_{rot}(K)}{kT_{rot}}\right] \exp\left[-\frac{E_{vib}(n)}{kT_{vib}}\right]. \quad (\text{A20})$$

Q_r and Q_v are the rotational and vibrational partition functions, respectively and $E_{vib}(n)$ and $E_{rot}(K)$ vibrational energy and rotational energy:

$$E_{vib}(n) = hc\omega_1 \left(n + \frac{1}{2}\right), \quad (\text{A21})$$

$$E_{rot}(K) = hcB_v K(K+1). \quad (\text{A22})$$

h is Planck's constant, ω_1 the vibrational constant, n is the vibrational quantum number and K is the rotational quantum number of the lower level apart from electronic spin. The vibrational partition function including the zero point energy is given by Herzberg [57]:

$$Q_v = \frac{\exp\left[-\frac{hc\omega_1}{2kT_{vib}}\right]}{1 - \exp\left[-\frac{hc\omega_1}{kT_{vib}}\right]}. \quad (\text{A23})$$

For the diatomic NH, the rotational partition function can be approximated by the classical expression [57]:

$$Q_r = \frac{kT}{hcB_v}. \quad (\text{A24})$$

Using molecular constants reported by Brazier *et al.* [35] and assuming the rotational and vibrational temperature to be equal to the gas temperature ($T = 1750$ K in the present work), the total NH density (m^{-3}) can be calculated as a function of the measured integrated absorption $A_{int} [\text{cm}^{-1}]$:

$$n_{NH} = \frac{n_{NH,J=9}}{f_b} = 7.39 \times 10^{21} A_{int} \quad (\text{A25})$$

B. Cross section of the $\tilde{A}^2A_1(0,9,0) \leftarrow \tilde{X}^2B_1(0,0,0)\Sigma^P Q_{1,N}(7)$ transition of NH_2 at 16739.90 cm^{-1}

For NH_2 , the integrated cross section can be calculated from information on the oscillator strength reported by Votsmeier *et al.* [39] and the molecular constants reported by Green *et al.* [40]. The relation between the integrated absorption cross section of a molecule σ_{int} and the oscillator strength f_{ik} of the transition is given by [54]:

$$\sigma_{int} = \frac{e^2}{4\varepsilon_0 m_e c} f_{ik} \cdot \quad (B1)$$

Using the fundamental physical constants for the electron mass m_e elementary charge e , the dielectric constant ε_0 the speed of light c and the oscillator strength $f_{ik} = 8.36 \times 10^{-5}$ reported by Votsmeier *et al.* [39], we find the following value for the integrated absorption cross section:

$$\sigma_{int} = 2.21 \times 10^{-10} \text{ m}^2 \text{ Hz} \quad (B2)$$

Using a similar procedure as for the NH radical in the previous section [Eqs. (A14)–(A16)], one can calculate the peak absorption cross section σ_{peak} for the $\tilde{A}^2A_1(0,9,0) \leftarrow \tilde{X}^2B_1(0,0,0)\Sigma^P Q_{1,N}(7)$ transition of NH_2 by incorporating the lineshape function $\Phi(0, a)$ for a gas temperature of 1750 K [Eq. (A15)]:

$$\sigma_{peak} = 5.53 \times 10^{-20} \text{ m}^2 \quad (B3)$$

To obtain the total density of NH_2 , we adapt a similar procedure as for the NH radical [Eqs. (A18) and (A19)]. The Boltzmann fraction f_b for NH_2 is given by Green *et al.* [40] and Kohse–Höinghaus *et al.* [58]:

$$f_b = \frac{3(2J''+1)}{4g''Q_rQ_v} \exp\left[-\frac{E_{rot}}{kT_{rot}}\right] \exp\left[-\frac{E_{vib}}{kT_{vib}}\right] \quad (B4)$$

Q_r and Q_v are the rotational and vibrational partition functions and J'' and g'' are the total rotational quantum number including spin and the electron–spin degeneracy of the lower state. The factor 3/4 occurs due to the nuclear spin of the H atoms. The vibrational energy E_{vib} for the NH_2 molecule is given by [57]:

$$E_{vib} = hc\omega_1\left(n_1 + \frac{1}{2}\right) + hc\omega_2\left(n_2 + \frac{1}{2}\right) + hc\omega_3\left(n_3 + \frac{1}{2}\right), \quad (B5)$$

with $\omega_1, \omega_2, \omega_3$ the vibrational constants and $n_1, n_2,$ and n_3 the vibrational quantum numbers of the lower state. The rotational energy is given by the following formula:

$$E_{rot} = hcF(J), \quad (B6)$$

where $F(J)$ is the experimentally determined rotational term value reported by Ross *et al.* [38]. The vibrational partition function including the zero point energy of the vibration is given by Green *et al.* [40]:

$$Q_r = \frac{\exp\left[-\frac{hc\omega_1}{2kT}\right] \exp\left[-\frac{hc\omega_2}{2kT}\right] \exp\left[-\frac{hc\omega_3}{2kT}\right]}{1 - \exp\left[-\frac{hc\omega_1}{kT}\right] 1 - \exp\left[-\frac{hc\omega_2}{kT}\right] 1 - \exp\left[-\frac{hc\omega_3}{kT}\right]} . \quad (\text{B7})$$

For NH₂, which is an asymmetric top molecule, the rotational partition function Q_r can be estimated by [40,57]:

$$Q_r = \frac{\sqrt{\pi}}{\sigma} \sqrt{\frac{8\pi^2 I_A kT}{h^2}} \sqrt{\frac{8\pi^2 I_B kT}{h^2}} \sqrt{\frac{8\pi^2 I_C kT}{h^2}} . \quad (\text{B8})$$

In this equation, σ is the symmetry number and I_A , I_B , and I_C are the moments of inertia of the NH₂ molecule. The symmetry number σ is equal to 2 and the electron spin degeneracy g'' is equal to 1, because the measured line is in fact a spin-split doublet, which is not resolved by the measurement. Using the moments of inertia and the vibrational frequencies reported by Green *et al.* [40] and assuming equal temperatures for rotation and vibration (1750 K), we can calculate the total NH₂ density (m⁻³) as a function of the measured integrated absorption A_{int} [cm⁻¹]:

$$n_{NH_2} = \frac{A_{int}}{\sigma_{int} l f_b} = 4.95 \times 10^{22} A_{int} \quad (\text{B9})$$

References

- [1] J.E. Klemberg–Sapieha, O.M. Küttel, L. Martinu, and M.R. Wertheimer, *J. Vac. Sci. Technol. A* **9**, 2975 (1991).
- [2] J. Kurdi, H. Ardelean, P. Marcus, P. Jonnard, and F. Arefi–Khonsari, *Appl. Surf. Sci.* **189**, 119 (2002).
- [3] A. Lu, and R. Sipehia, *Biomaterials* **22**, 1439 (2001).
- [4] E.F. Castro Vidaurre, C.A. Achete, R.A. Simão, and A.C. Habert, *Nucl. Instrum. Methods B* **175–177**, 732 (2001)
- [5] E.S. Aydil, K.P. Giapis, R.A. Gottscho, V.M. Donnelly, and E. Yoon, *J. Vac. Sci. Technol. B* **11**, 195 (1993).
- [6] C–M. Yu, H–C. Lin, T–Y. Huang, and T–F. Lei, *J. Electrochem. Soc.* **150**, G843 (2003).
- [7] Y–S. Lai, K–J. Chen, and J.S. Chen, *J. Appl. Phys.* **91**, 6428 (2002).
- [8] J.C. Wang, D.C. Shie, T.F. Lei, and C.L. Lee, *Electrochem. Solid St.* **6**, F34 (2003).
- [9] M. Chhowalla, K.B.K. Teo, C. Ducati, N.L. Rupasinghe, G.A.J. Amaratunga, A.C. Ferrari, D. Roy, J. Robertson, and W.I. Milne, *J. Appl. Phys.* **90**, 5308 (2001).
- [10] Z.P. Huang, J.W. Xu, Z.F. Ren, J.H. Wang, M.P. Siegal, and P.N. Provencio, *Appl. Phys. Lett.* **73**, 3845 (1998).
- [11] Y.J. Lee and S–W. Kang, *Thin Solid Films* **446**, 227 (2004).
- [12] H.S. Sim, J.H. Park, and Y. T. Kim, *Phys. Status Solidi A* **201**, R92 (2004).
- [13] O–K. Kwon, S–H. Kwon, H–S. Park, and S–W. Kang, *Electrochem. Solid St.* **7**, C46 (2004).
- [14] A.G. Aberle, *Sol. Energ. Mat. Sol. Cells* **65**, 239 (2001).
- [15] J. Hong, W.M.M. Kessels, W.J. Soppe, A.W. Weeber, W.M. Arnoldbik, and M.C.M. van de Sanden, *J. Vac. Sci. Technol. B* **21**, 2123 (2003).
- [16] D. Stryahilev, A. Sazonov, and A. Nathan, *J. Vac. Sci. Technol. A* **20**, 1087 (2002).
- [17] G.P. Miller and J.K. Baird, *J. Phys. Chem.* **97**, 10984 (1993).
- [18] S.D. Pringle, V.S. Joss, and C. Jones, *Surf. Interface Anal.* **24**, 821 (1996).
- [19] E.R. Fisher, P. Ho. W.G. Breiland, and R.J. Buss, *J. Phys. Chem* **96**, 9855 (1992).
- [20] P.R. McCurdy, C.I. Butoi, K.L. Williams, and E.R. Fisher, *J. Phys. Chem. B* **103**, 6919 (1999).
- [21] M.L. Steen, K.R. Kull, and E.R. Fisher, *J. Appl. Phys.* **92**, 55 (2002).
- [22] H. Unemoto, K. Ohara, D. Morita, T. Morimoto, M. Yamawaki, A. Masuda, and H. Matsumura, *Jpn. J. Appl. Phys.* **42**, 5315 (2003).
- [23] D.L. Smith, A.S. Alimonda, C–C. Chen, S.E. Ready, and B. Wacker, *J. Electrochem. Soc.* **137**, 614 (1990).
- [24] D.L. Smith, *J. Vac. Sci. Technol. A* **11**, 1843 (1993).

- [25] M.S. Bell, R.G. Lacerda, K.B.K. Teo, N.L. Rupesinghe, G.A.J. Amaratunga, and W.I. Milne, *Appl. Phys. Lett.* **85**, 1137 (2004).
- [26] S.D. Rodgers and S.B. Charnley, *Astrophys. J.* **546**, 324 (2001).
- [27] H. Kawakita, J. Watanabe, H. Ando, W. Aoki, T. Fuse, S. Honda, H. Izumiura, T. Kajino, E. Kambe, S. Kawanomoto, K. Noguchi, K. Okita, K. Sadakane, B. Sato, M. Takada–Hidai, Y. Takeda, T. Usuda, E. Watanabe, and M. Yoshida, *Science* **294**, 1089 (2001).
- [28] J. Hong, W.M.M. Kessels, F.J.H. van Assche, H.C. Rieffe, W.J. Soppe, A.W. Weeber, and M.C.M. van de Sanden, *Progress in Photovoltaics* **11**, 125 (2003).
- [29] W.M.M. Kessels, C.M. Leewis, M.C.M. van de Sanden, and D.C. Schram, *J. Appl. Phys.* **86**, 4029 (1999).
- [30] M.C.M. van de Sanden, R.J. Severens, W.M.M. Kessels, R.F.G. Meulenbroeks, and D.C. Schram, *J. Appl. Phys.* **84**, 2426 (1998); *J. Appl. Phys.* **85**, 1243 (1999).
- [31] A.J.M. Buuron, D.K. Otorbaev, M.C.M. van de Sanden, and D.C. Schram, *Phys. Rev. E* **50**, 1383 (1994).
- [32] K.W. Busch and M.A. Busch, *Cavity–Ringdown Spectroscopy – An Ultratrace–Absorption Measurement Technique*, American Chemical Society, Washington (1998).
- [33] J.P.M. Hoefnagels, Y. Barrell, W.M.M. Kessels, and M.C.M. van de Sanden, *J. Appl. Phys.* **96**, 4094 (2004).
- [34] D. Romanini and K.K. Lehmann, *J. Chem. Phys.* **99**, 6287 (1993).
- [35] C.R. Brazier, R.S. Ram, and P.F. Bernath, *J. Mol. Spectrosc.* **120**, 381 (1986).
- [36] J.M. Lents, *J. Quant. Spectrosc. Radiat. Transfer* **13**, 297 (1973).
- [37] *Manual PrecisionScan–D dye laser*. Sirah Laser– und Plasmatechnik GmbH, Darmstadt, Germany (1999).
- [38] S.C. Ross, F.W. Birss, M. Vervloet, and D.A. Ramsay, *J. Mol. Spectrosc.* **129**, 436 (1988).
- [39] M. Votsmeier, S. Song, D.F. Davidson, and R.K. Hanson, *Int. J. Chem. Kinet.* **31**, 323 (1999).
- [40] R.M. Green, and J.A. Miller, *J. Quant. Spectrosc. Radiat. Transfer* **26**, 313 (1981).
- [41] W.M.M. Kessels, A. Leroux, M.G.H. Boogaarts, J.P.M. Hoefnagels, M.C.M. van de Sanden, and D. C. Schram, *J. Vac. Sci. Technol. A* **19**, 467 (2001)
- [42] L. Viktor, A. Al–Khalili, H. Danared, N. Djuric, G.H. Dunn, M. Larsson, A. Le Padellec, S. Rosén, and M. af. Ugglas, *Astron. Astrophys.* **344**, 1027 (1999).
- [43] R.F.G. Meulenbroeks, A.J. van Beek, A.J.G. van Helvoort, M.C.M. van de Sanden, and D.C. Schram, *Phys. Rev. E.* **49**, 4397 (1994).
- [44] R. Derai, G. Mauclaire, and R. Marx, *Chem. Phys. Lett.* **86**, 275 (1982).
- [45] J. Perrin, O. Leroy, and M.C. Bordage, *Contrib. Plasm. Phys.* **36**, 3 (1996).
- [46] M.J. Kushner, *J. Appl. Phys.* **71**, 4173 (1992).

- [47] I. Rahinov, N. Ditzian, A. Goldman, and S. Cheskis, *Appl. Phys. B.* **77**, 541 (2003).
- [48] T. Ko, P. Marshall, and A. Fontijn, *J. Phys. Chem.* **94**, 1401 (1990).
- [49] M.P. Skrzypkowski and R. Johnsen, *Chem. Phys. Lett.* **274**, 473 (1997).
- [50] J. Öjekull, P.U. Andersson, M.B. Någård, J.B.C. Pettersson, A.M. Derkatch, A. Neau, S. Rosén, R. Thomas, M. Larsson, F. Österdahl, J. Semaniak, H. Danared, A. Källberg, M. af. Ugglas, and N. Marković, *J. Chem. Phys.* **120**, 7391 (2004).
- [51] W.M.M. Kessels, J.P.M. Hoefnagels, M.G.H. Boogaarts, D.C. Schram, and M.C.M. van de Sanden, *J. Appl. Phys.* **89**, 2065 (2001).
- [52] J. Benedikt, D.C. Schram, and M.C.M. van de Sanden, *J. Phys. Chem. A* **109**, 10153 (2005).
- [53] A. Schadee, *Astron. & Astrophys.* **41**, 213 (1975).
- [54] A.P. Thorne, *Spectrophysics*, Chapman and Hall & Science Paperbacks (1974)
- [55] G. Herzberg, *Spectra of diatomic molecules*, D. Van Nostrand Company, Inc. (1965).
- [56] G. Friedrichs, M. Colberg, M. Fikri, Z. Huang, J. Neumann, and F. Temps, *J. Phys. Chem. A* **109**, 4785 (2005).
- [57] G. Herzberg, *Molecular spectra and molecular structure, Vol. II. Infrared and Raman Spectra of Polyatomic Molecules*, D. Van Nostrand Company, Inc. (1966)
- [58] K. Kohse-Höinghaus, D.F. Davidson, A.Y. Chang, and R.K. Hanson, *J. Quant. Spectrosc. Radiat. Transfer* **42**, 1 (1989).

Chapter 3

Downstream ion and radical densities in an Ar–NH₃ plasma generated by the expanding thermal plasma technique*

A full characterization of the Ar–NH₃ expanding thermal plasma source applied in industrial processes for high–rate silicon nitride deposition is presented in terms of absolute densities of reactive species such as ions and radicals. The ion composition of the plasma was identified by mass spectrometry, while absolute ion density information was obtained by Langmuir probe measurements. N radicals were detected by threshold ionization mass spectrometry, whereas NH and NH₂ radicals were measured by cavity ring–down spectroscopy. It was found that the ion density decreases from 10^{13} cm^{-3} in a pure Ar plasma to 10^{10} – 10^{11} cm^{-3} when NH₃ is injected, with ArH⁺, NH₂⁺, NH₃⁺, NH₄⁺ and H₃⁺ being the most abundant ions. The densities of N and NH both saturate at a level of $3 \times 10^{12} \text{ cm}^{-3}$ at NH₃ flows above 3 sccs while the density of NH₂ increases linearly with the NH₃ flow and reaches a level of $4 \times 10^{12} \text{ cm}^{-3}$. When the plasma source current is increased, the densities of N and NH increase linearly, while the NH₂ density remains approximately constant. Furthermore, it is revealed that most of the consumed NH₃ is converted into N₂ and H₂ in the plasma.

* Published as: P.J. van den Oever, J.L. van Hemmen, J.H. van Helden, D.C. Schram, R. Engeln, M.C.M. van de Sanden, and W.M.M. Kessels, *Plasma Sources Sci. Technol.* 15, 546 (2006).

I. Introduction

New developments in industries that rely on plasma-based processing of materials as well as emerging applications of plasmas are the driving factor behind a continuous innovation in the science and technology of plasma processing. There is for example a need for plasma sources that can deliver a high flux of reactive species such as ions and radicals and simultaneously satisfy industrial requirements such as robustness, versatility and freedom in the choice of reactant mixture, the absence of drift, and reasonably low maintenance. A plasma source that seems to fulfill these requirements to a large extent is the Expanding Thermal Plasma (ETP), developed at the Eindhoven University of Technology [1,2]. This remote technique combines a high-pressure plasma source with a low-pressure processing reactor used for deposition, etching, etc. The very high fluxes of reactive species produced by this source make it very suitable for high rate deposition and etching processes. The application of this technique for deposition has been demonstrated for various materials including amorphous and nanocrystalline silicon [2,3], silicon dioxide [4], amorphous carbon [5], zinc oxide [6] and silicon nitride [7,8]. After a period of more than a decade of lab operation, the ETP source has recently been commercialized by General Electric for the deposition of silicone ($\text{SiC}_x\text{H}_y\text{O}_z$) scratch resistive coatings for automotive purposes [9] and by OTB Solar for the deposition of silicon nitride antireflection coatings for solar cells [10]. For this purpose, the ETP technique has been implemented in the DEP_x (inline) deposition system. The ETP deposited silicon nitride is also investigated as a moisture diffusion barrier for the encapsulation of organic LEDs [11,12].

For the deposition of silicon nitride thin films, a pure Ar plasma generated by the ETP source is used to dissociate NH_3 molecules which are injected into the plasma at the position of the source exit. The reactive NH_x fragments created subsequently react with the SiH_4 molecules which are injected in the downstream region. In this region, the reactive fragments of SiH_4 and NH_3 can deposit onto substrates forming a silicon nitride thin film. For efficient process optimization with respect to the different applications of the silicon nitride (antireflection coating, surface and bulk passivation, moisture diffusion barrier), detailed knowledge of the behaviour of the ETP source for various operating conditions, such as Ar- NH_3 gas flows and source power, is required. Furthermore, fundamental studies of the Ar- NH_3 plasma system also contribute to generic insight into NH_3 -based plasmas which can be relevant for emerging applications of NH_3 plasmas such as the passivation of semiconductor devices [13], the alteration of polymer wettability [14], the modification of the biocompatibility of materials for medical applications [15], and the deposition of carbon nanotubes (when hydrocarbons are admixed) [16].

Although many studies correlated plasma settings to device performance for various industrial processes using NH_3 plasmas, the properties of NH_3 plasmas have been investigated poorly in terms of densities of reactive ions and radicals. The study by Miller and Baird [17] in 1993 into the NH_3 decomposition efficiency was one of the first addressing the ammonia dissociation chemistry. In 1996, Pringle *et al.* [18] reported results on the role of the ions and radicals in a helicon resonator using mass spectrometry. They found that NH_4^+ and NH_3^+ were the dominant ions in the plasma, but did not attempt to measure N, NH and NH_2 radicals in the plasma. Most reported studies remain fairly descriptive and measurements of absolute NH_x ($x=0-2$) radical densities in plasmas are rarely reported, while these radicals are presumably of pivotal importance in surface modification and deposition processes. The interaction of the radicals NH and NH_2 with the surface of various materials has been addressed by Fisher and co-workers using a molecular plasma beam [19–21].

In an earlier publication, we discussed the absolute density and the production mechanism of NH and NH_2 radicals in the Ar– NH_3 Expanding Thermal Plasma in detail [22]. Here we will extend these results to a complete characterization of the ETP source operated on Ar– NH_3 , which will also involve measurements of the ion composition and density in the plasma and measurements of the absolute N radical density. Furthermore, we will include a discussion about the consumption of the injected NH_3 precursor and the resulting generation of H_2 and N_2 molecules in the plasma.

After presenting the basic principle of the expanding thermal plasma and the experimental details of the plasma diagnostics used in this study (section II), we will discuss the experimental results in section III. To obtain a general view of the operation of the ETP source on a Ar– NH_3 mixture, we have focused on two important parameters, the NH_3 gas flow variation (section. III.A) and the plasma source current variation (section III.B). Data obtained from Langmuir probe measurement (ion densities), line-of-sight mass spectrometry (ion composition), threshold ionization mass spectrometry (N density) and cavity ring-down spectroscopy (NH and NH_2 densities) will be presented. Furthermore, the consumption of NH_3 and the production of new molecules (H_2 and N_2) in the plasma will be addressed. In section IV the results will be summarized.

II. Experimental setup and plasma diagnostics

A. Expanding thermal plasma technique

Figure 1 shows a schematic overview of the so-called cascaded arc plasma source used in the ETP technique [1,2]. The plasma is created at high pressure in a narrow channel (typically 4 mm in diameter and a few centimeters in length) filled

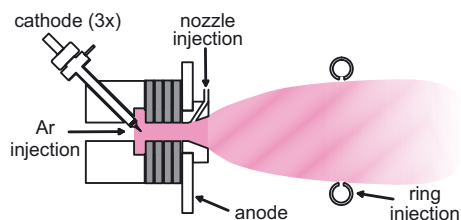


Figure 1: Schematic representation of the plasma source used in the expanding thermal plasma (ETP) technique.

with a non-depositing gas such as Ar, N₂ and/or H₂ by applying a dc voltage between one or more cathodes and one common grounded anode. The cathode(s) and anode are separated by four “cascaded plates” which are at floating potential. The discharge is current controlled between 30 and 75 A and the voltage is typically 40 V when operated at a typical Ar flow of 55 standard cm³ s⁻¹ (sccs). Due to the high pressure of typically 400 mbar (350 Torr) and high gas temperature in the plasma channel, the Ar atoms are very effectively ionized and consequently the ionization degree in the plasma channel can be as high as 20 %. As reported previously [23], the plasma expands supersonically from a conical shaped nozzle into a low pressure reactor at typically ~0.2 mbar (~0.15 Torr) until it reaches the stationary shock that is situated approximately 7 cm from the source exit. Subsequently, the expansion continues subsonically and in this stage the plasma can be characterized as a recombining plasma as no electrical power is coupled into the plasma in this downstream zone. The electron temperature is low (0.2–0.3 eV) and as a consequence electron impact induced chemistry and ion bombardment due to the plasma self bias are virtually absent, contrary to the situation in many conventional plasma techniques. The main reactive species in the expanding plasma are argon ions (downstream ionization degree 5–10 %) as the density of argon metastables is more than a factor of 10 lower than the Ar ion density [24]. For pure Ar plasmas, it has been shown that the downstream ion density increases linearly with the arc current [25,26]. The Ar–NH₃ plasma discussed in this publication is generated by injecting a NH₃ flow of 1 to 17 sccs at the outlet of the plasma source via a slit in the nozzle.

B. Plasma diagnostics

Figure 2 shows the reactor chamber and the plasma diagnostics used to investigate the reactive species in the downstream Ar–NH₃ plasma. The reactor chamber has a length of 0.82 m and a diameter of 0.50 m and it is pumped by a pump stack consisting of a large roots blower (1900 m³/h) backed by a small roots blower (500 m³/h) and a roughing pump (65 m³/h). In Fig. 2(a) the laser setup used for the cavity ring-down experiments and the double Langmuir probe are shown

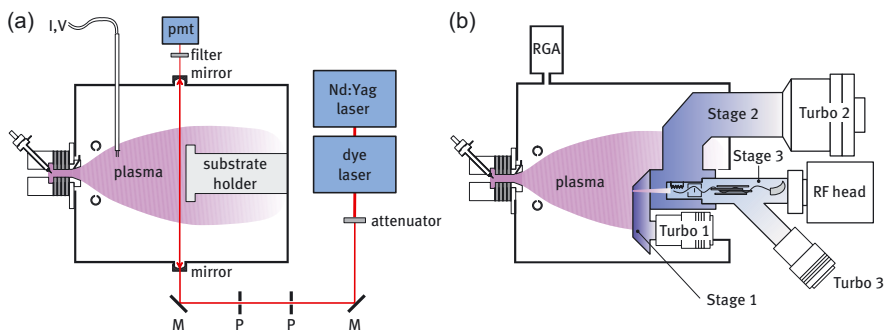


Figure 2: The experimental arrangement for (a) cavity ring-down spectroscopy and Langmuir probe measurements and (b) for threshold ionization mass spectrometry and residual gas analysis. In the figure “P” stands for pinhole, “M” for mirror and “pmt” for photo multiplier tube.

schematically, while Fig. 2(b) shows the implementation of the triple stage differentially pumped mass spectrometer in the setup as well as the residual gas analyzer. These diagnostic techniques will be discussed in greater detail in the following sections.

Langmuir probe technique

The ion and electron densities in the plasma were determined by double Langmuir probe measurements as described in our previous work [26,27]. Briefly, a double cylindrical probe is immersed in the plasma and the collected current is measured as a function of the applied potential between the two probes (-20 V to 20 V) using a Keithley 2400 source measure unit. The probes are made of tungsten wire with a diameter of 0.18 mm and they protrude about 1 cm from a long ceramic tube. The distance between the two probes is approximately 3 mm. For the typical electron densities (10^{10} – 10^{13} cm^{-3}) and electron temperature (~ 0.3 eV) in the ETP technique, the Debye length is $< 10^{-4}$ m. This implies that the plasma sheath thickness is smaller than the mean free path of the ions in the plasma which is in the order of 10^{-3} m. The plasma sheath can therefore be considered as collisionless. The Langmuir probe measurements were analyzed by the procedure proposed by Petersen and Talbot [26,28] yielding the electron temperature and the ion saturation current at plasma potential. The ion mass used in the analysis was 40 amu for pure Ar plasmas and 17 amu for Ar–NH₃ plasmas. Assuming quasi-neutrality and an equal temperature for the electrons and ions in the plasma, which is a valid assumption for the expanding thermal plasma [29], we can deduce the ion and electron density from the ion saturation current at plasma potential.

The radial measurements were carried out at two distances from the plasma source (at 9 and 36 cm), while the measurements as a function of the distance from the source were carried out along the axis of the plasma beam. The relative error in the Langmuir probe measurements is approximately 30% for the electron temperature and 20% for the electron density [29].

Cavity ring-down spectroscopy on NH and NH₂

The cavity ring-down setup used for the NH and NH₂ absorption measurements is schematically depicted in Fig. 2(a). Two plano-concave mirrors are placed 112 cm apart at a distance of 36 cm from the plasma source. The mirrors are protected from the influence of reactive plasma species by an Ar flow that is injected in front of the mirrors. The laser pulses were generated by a dye laser pumped by the second harmonic of a Nd:YAG laser working at a repetition rate of 10 Hz. The pulse energy measured directly in front of the cavity was attenuated to below 100 μJ to prevent optical saturation of the transitions used in the absorption measurements. The light intensity leaking out of the cavity was measured through an interference bandpass filter by a photomultiplier tube and for every single laser shot the decay rate was sampled by a 100 MHz, 12 bits data acquisition system [30]. All decay rates were single exponential and they were analyzed by a weighted least squares fit of the logarithm of the transient data. The consecutive decay rates were averaged 20 times to improve the signal to noise ratio. More details on the cavity ring-down setup can be found elsewhere [22,30].

The NH radical density was measured on the (0-0) band of the $A^3\Pi \leftarrow X^3\Sigma^-$ transition at ~339.6 nm ($P_{33}(9)$ absorption line), while for the detection of the NH₂ radical the (0,9,0)-(0,0,0) band of the $\tilde{A}^2A_1 \leftarrow \tilde{X}^2B_1$ transition at ~597.4 nm was used ($\Sigma^P Q_{1,N}(7)$ line). The complete derivation of the integrated absorption cross sections used for the density determination can be found elsewhere [22]. The largest uncertainty in the absolute values of the densities reported is most likely generated by the assumption of the absorption path length in the cavity. Based on earlier results in a similar type of plasma, we estimate that the absorption path length is approximately 30 cm [31]. The error in the NH and NH₂ densities introduced by this estimation can be as large as a factor 3.

(Threshold ionization) mass spectrometry

In this work a triple stage differentially pumped mass spectrometer [32] was used to measure the densities of N radicals in the plasma. The current design was modified from a single stage version used to measure N radicals in N₂-SiH₄ plasmas in our previous work [7]. The triple stage design allows for a relatively high beam-to-background ratio in the mass spectrometer, resulting in a high sensitivity for reactive

species. Furthermore, it facilitates the determination of absolute number densities of plasma radicals. Briefly, the plasma is sampled by effusive extraction through a 0.8 mm orifice that is situated approximately 56 cm from the plasma source and 4.5 cm off the reactor axis (due to geometrical reasons). This extraction creates a molecular beam in the mass spectrometer. The second orifice, connecting the first and second stage, has a diameter of approximately 1.6 mm and is situated at a distance of 4 cm from the sampling orifice. Finally, the third orifice connecting the second and third stage is 4 mm wide and is situated at a distance of 8 cm from the second orifice. The quadrupole mass spectrometer (Hiden Analytical Epic 300, PSM upgrade) is placed in the third stage, in line-of-sight with the three orifices. The mass spectrometer consists of an ionizer cage, followed by a Bessel box energy analyzer, a quadrupole mass filter, a channeltron detector and several electrostatic lenses to focus the ion beam.

The pumping speeds and the influx in the three stages determine the pressure in the various stages. The pumping speed (for N_2) of the turbomolecular pumps in the first, second and third stage are 35 l/s, 300 l/s and 56 l/s, respectively. However, simulations have shown that the effective pumping speeds are lower due to a limited conductivity between the stages and the pumps [32]. Typical pressures in the second and third stage during measurements are $\sim 10^{-6}$ mbar ($\sim 10^{-6}$ mTorr) and $\sim 10^{-7}$ mbar, while the third stage base pressure is below $\sim 10^{-9}$ mbar. The finite pressure in the third stage means that the measured signal will not only consist of a beam component, but also of a background component.

For accurate measurements of the absolute radical densities, it is necessary to distinguish the beam component from the background component of the species in the third stage. Therefore, a chopper that modulates the incident molecular beam, is situated in the second stage in front of the orifice connecting the second and third stage. It has been shown that if the chopping frequency is faster than the residence time of the species in the ionizer cage of the mass spectrometer, the measured background signal will be constant during one complete chopping period and accurate background subtraction is possible. Using a sufficiently high chopping frequency, a beam-to-background ratio of 0.31 was determined for NH_3 .

In general, electron impact ionization of radicals has a lower threshold energy (ionization potential) than dissociative ionization of parent molecules (appearance potential) leading to the same ion. This fact is exploited in threshold ionization mass spectrometry in which the signal is measured at a certain mass-over-charge (m/z) ratio versus the energy of the electrons used for ionization. Table 1 shows the different ionization processes contributing to the signal at a m/z ratio of 14 which is used to measure atomic N and Fig. 3 shows the corresponding measurement signal versus electron energy in an Ar- NH_3 mixture for plasma off and plasma on.

Table 1: Literature values for the different electron–impact ionization processes contributing to the measured signal at a mass–over–charge ratio of 14.

	Process	Ionization/Appearance potential	Reference
A	$N + e \rightarrow N^+ + 2e$	15.3 eV	Kim <i>et al.</i> [33]
B	$NH_3 + e \rightarrow N^+ + H_2 + H + 2e$	22.6 eV	Rosenstock <i>et al.</i> [34]
C	$N_2 + e \rightarrow N^+ + N + 2e$	24.3 eV	Rosenstock <i>et al.</i> [34]

The plasma off signal shows an appearance potential of ~ 24.4 eV which is due to the dissociative ionization of NH_3 (process B). The plasma on signal, on the other hand, has a contribution appearing at ~ 15.6 eV due to direct ionization of N radicals (process A). At ~ 24.9 eV, the plasma on signal shows the contributions related to dissociative ionization of NH_3 and of N_2 that is created in the Ar– NH_3 plasma, as will be discussed in section III.A. The appearance potential of the dissociative ionization of N_2 (process C), is approximately 24.3 eV and cannot be distinguished from the dissociative ionization of NH_3 (process B) within the accuracy of the measurement. The increase in signal above ~ 24 eV cannot be explained by dissociative ionization of NH_3 solely, because the signal due to NH_3 should be smaller in the ‘plasma on’ case than in the ‘plasma off’ case due to consumption of NH_3 in the plasma. The observed values for the appearance potentials are in good agreement with values reported in the literature (see table 1).

To obtain absolute densities of N radicals by mass spectrometry, we used the calibration procedure proposed by Singh *et al.* [35] which is based on the direct ionization of molecules with a known density in the reactor for the plasma off situation (NH_3 in our case). To avoid the need for continuous calibration of the electron energy scale, we used the slopes of the measured signals S_S versus the electron energy instead of the signal at one specific electron energy. Equivalently, also the slopes of the electron impact ionization cross sections σ_S versus electron energy were used. This procedure also improves the accuracy in the densities by averaging the data. From the ratio between the signal of N radicals to the signal of the known NH_3 density in the reactor for the plasma off situation, we obtain an expression for the absolute N density:

$$n_N = \frac{S_S^{N \rightarrow N^+}}{S_S^{NH_3 \rightarrow NH_3^+}} \frac{F(m_{NH_3})}{F(m_N)} \frac{I_{e,NH_3}}{I_{e,N}} \frac{\sigma_S^{NH_3 \rightarrow NH_3^+}}{\sigma_S^{N \rightarrow N^+}} \frac{1 + R_{NH_3}}{R_{NH_3}} n_{NH_3}. \quad (1)$$

In this expression, the instrument dependent geometrical factor present in the relation between measured signal and density in the reactor cancels out. $F(m_i)$ is the mass dependent proportionality constant, which is instrument dependent and which has a $m_i^{-0.3}$ dependence for the current system, $I_{e,i}$ is the emission current generated

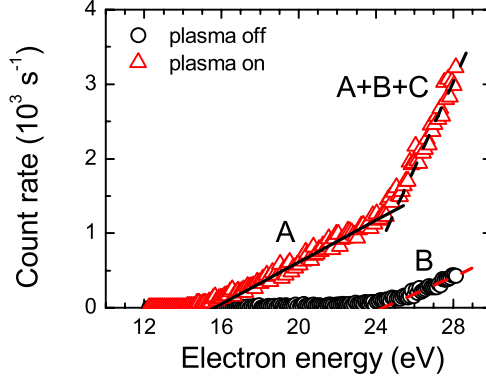


Figure 3: Scan of the mass spectrometer count rate at a mass-over-charge ratio of 14 versus the electron energy used for ionization as obtained for an Ar-NH₃ gas mixture (plasma off) and an Ar-NH₃ plasma (plasma on). The plasma on signal clearly shows the contribution of the N radicals (A) to the signal at low electron energies. At high electron energies, the signal originates mainly from the dissociative ionization of NH₃ (B) and N₂ (C). The N₂ is produced in the plasma.

by the filament in the ionizer and $\sigma_S^{i \rightarrow j^+}$ is the slope of the cross section for electron impact ionization versus energy. $\sigma_S^{N \rightarrow N^+}$ was determined from data reported by Kim *et al.* [36] and $\sigma_S^{NH_3 \rightarrow NH_3^+}$ was determined from data reported by Tarnovsky *et al.* [37] and Märk *et al.* [38]. The factor $R_{NH_3} = 0.31$ is the beam-to-background ratio for NH₃. It is assumed that N radicals do not have a background contribution due to their high surface loss probability on stainless steel at the low operating pressure in the third stage of the mass spectrometer [39]. The overall uncertainty in the absolute densities introduced by this calibration method can be as large as a factor of 3.

Apart from N radical measurements, the mass spectrometer was also used to determine the densities of molecules in the plasma, such as NH₃, H₂ and N₂. The calibration procedure to obtain absolute densities of H₂ and N₂ which are created in the plasma was carried out using different reference gas mixtures of H₂ and N₂ with Ar in order to mimic the actual measurement situation in terms of flows and pressure. The calibration factor was determined from the slope of the measured signal versus the densities calculated using the ideal gas law. This calibration procedure was carried out prior to every measurement run.

The relative consumption or depletion D of NH₃ can be calculated from the measured signals and is defined as:

$$D_{NH_3} = \frac{S_S^{NH_3 \rightarrow NH_3^+}(\text{off}) - S_S^{NH_3 \rightarrow NH_3^+}(\text{on})}{S_S^{NH_3 \rightarrow NH_3^+}(\text{off})}, \quad (2)$$

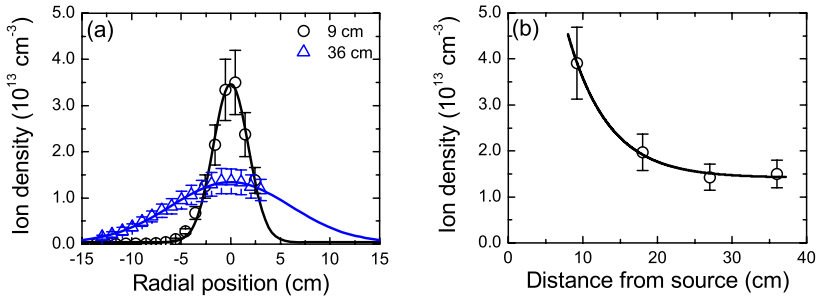


Figure 4: (a) The radial ion density profile in a pure Ar expanding plasma at 9 and 36 cm from the source determined by Langmuir probe measurements. The lines are Gaussian fits. (b) The axial ion density as a function of the distance from the plasma source. The line is a guide to the eye. The plasma current was 45 A and the Ar flow 55 sccs.

with $S_5^{NH_3 \rightarrow NH_3^+}$ (off) and $S_5^{NH_3 \rightarrow NH_3^+}$ (on) the NH_3 signals when the plasma is off and on, respectively.

The ion composition of the plasma was measured with the ionizer cage of the mass spectrometer switched off. In this case, a small negative voltage was applied to the extractor plate of the mass spectrometer to ensure efficient extraction of the ions from the plasma, unlike the situation for the detection of neutral species where a positive voltage was applied to prevent the collection of ions from the plasma. The other electrostatic lenses in the system were adjusted to optimize the mass spectrometer's signal for ion detection. Ions can be detected with a much higher sensitivity than neutrals due to the absence of the low-efficiency ionization step in the detection process. Therefore, the ion density in the mass spectrometer can be high, especially for high ion densities in the plasma, which can lead to space charge build up that can reduce the measured signals. It is likely that the measurements in a (nearly) pure Ar plasma have suffered from this effect as well as from saturation of the detector signal.

III. Results

A. Influence of NH_3 flow

Ion density and composition

Figure 4 shows the ion density determined from the Langmuir probe measurements for an Ar flow of 55 sccs (no NH_3), a plasma source current of 45 A and a downstream pressure of 0.20 mbar. Figure 4(a) shows the ion density as a function of the radial distance from the centre of the plasma beam measured at 9 cm and 36

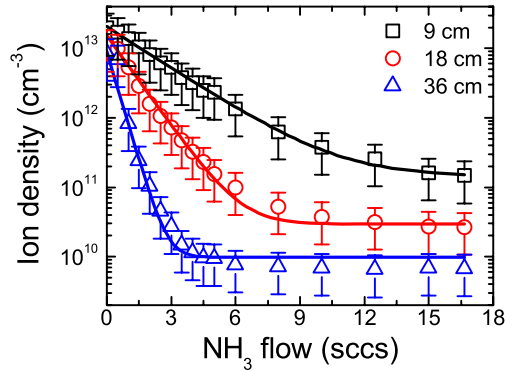


Figure 5: The axial ion density as a function of the injected NH_3 flow for a plasma current of 45 A and an Ar flow of 55 sccs. The ion densities were measured by a Langmuir probe at three different distances from the source. The lines represent exponential fits of the measurements.

cm from the plasma source. At 9 cm a maximum ion density of $3.5 \times 10^{13} \text{ cm}^{-3}$ is reached on the axis of the plasma beam, while the ion density drops drastically in radial direction. At 36 cm the axial ion density has decreased by more than a factor two while the profile has broadened in radial direction. The observed ion density profiles can be fitted with a Gaussian line shape (see Fig. 4(a)) revealing a full-width-half-maximum of 4 cm and 14 cm for an axial position of 9 cm and 36 cm respectively. The expansion of the Ar plasma beam is therefore clearly apparent from Fig. 4. The decrease of the axial ion density as a function of the distance to the plasma source is relatively minor as can be observed from Fig. 4(b). This behaviour is well understood from our previous studies [24] which revealed that the decrease in Ar^+ density is governed by three particle recombination reactions, which have a very low equivalent two body reaction rate at these electron/ion densities. From the radial ion density measurements also the flow of Ar^+ ions emanating from the plasma source can be calculated by integrating over the Gaussian density profile and assuming a directed beam velocity ($\sim 1400 \text{ m/s}$ at 9 cm and 450 m/s at 36 cm from the plasma source) [40]. For a plasma source current of 45 A this leads to an Ar^+ ion flow of ~ 3.5 sccs emanating from the source, in agreement with previous estimates [41].

Figure 5 shows the axial ion density in the downstream plasma when a NH_3 flow is injected in the plasma. The pressure is kept at 0.20 mbar and the ion density is measured at three different positions from the plasma source. The ion density decreases drastically when NH_3 is injected and the drop in ion density can be fitted by an exponential decay as can be seen in Fig. 5. At a distance of 36 cm from the source, the ion density reaches a value of $1.3 \times 10^{10} \text{ cm}^{-3}$ for an injected NH_3 flow of 4 sccs, after which the ion density remains approximately constant. This fast decrease in ion

density when a molecular gas is introduced in the plasma is well understood for the ETP plasma and is caused by charge transfer reactions between Ar^+ ions and NH_3 molecules forming NH_3^+ ions. These molecular ions can subsequently recombine dissociatively with electrons forming radicals such as N, NH and NH_2 as addressed in the next section. The recombination channel of the ions in the downstream Ar- NH_3 plasma is very fast because of the large reaction rates of the charge exchange reaction ($k_{ce} = 1.84 \times 10^{-9} \text{ cm}^3 \text{ s}^{-1}$ [42]) and the dissociative recombination reaction ($k_{dr} = 1.8 \times 10^{-7} \text{ cm}^3 \text{ s}^{-1}$ for an electron temperature of 0.3 eV [43]) compared to the three particle recombination reaction*. Closer to the plasma source the ion density on the axis of the plasma beam is higher and the decrease upon NH_3 injection is slower, which can be attributed to the fact that the charge exchange reactions need time to complete in the expanding plasma beam with a high average forward velocity (~900 m/s).

Apart from the ion density, also the electron temperature can be deduced from the Langmuir probe measurements. The measurements revealed an electron temperature of 0.3 ± 0.1 eV at the axis of the plasma beam and did not show a pronounced trend with either the axial position or the flow of NH_3 injected. Electron temperatures around 0.3 eV are typically reported for the ETP technique as already mentioned in section II. More information on the ionic species present in the plasma was obtained by ion mass spectrometry measurements as shown in Figs. 6(a) to 6(c). The measurements were carried out with a plasma source current of 70 A instead of 45 A while all the other conditions remained constant. The difference in current has only a significant influence on the absolute ion and radical densities (see section III.B). The signals were corrected for the mass filter transmittance and detector efficiency of the mass spectrometer which showed a $m^{-0.3}$ dependence (see section II.B). For a pure Ar plasma and for very low NH_3 flows (< 0.25 sccs), the ion density is very high and the count rate might be limited by space charge building up in the mass spectrometer or by the maximum count rate of the detector in the mass spectrometer as mentioned before. However, it is clear that Ar^+ is the most abundant ion in the plasma under these conditions. When NH_3 is injected, the Ar^+ ion signal shows a sharp drop and ArH^+ becomes the most abundant ion in the plasma at low NH_3 flows as can be seen from Fig. 6(a). For higher NH_3 flows the ArH^+ signal decreases exponentially until the signal disappears at NH_3 flows over 3 sccs. Above a NH_3 flow of 0.5 sccs also ions such as NH_4^+ , NH_3^+ , NH_2^+ , H_3^+ and H^+ become important in the plasma while the signal of H_2^+ remains very low under all conditions. Figures 6(b) and

* The rate for the charge exchange reaction k_{ce} can also be estimated from the initial decrease in ion density depicted in Fig. 5. Using mass spectrometric measurements of the NH_3 density in the plasma and assuming an average forward velocity of 900 m/s, k_{ce} was estimated to be approximately $3 \times 10^{-10} \text{ cm}^3 \text{ s}^{-1}$.

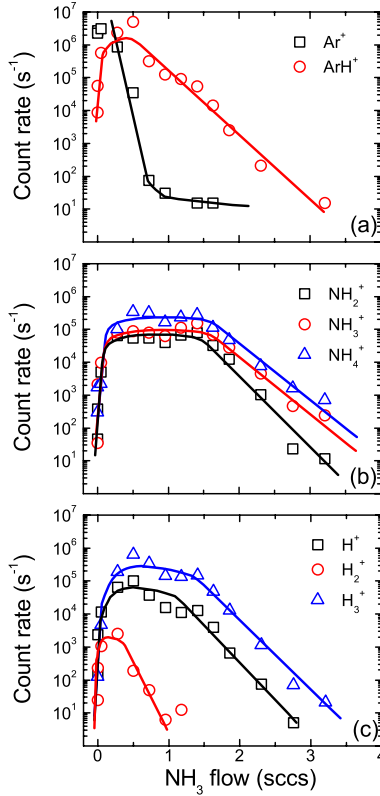


Figure 6: Ion mass spectrometry data revealing the ion composition in the Ar–NH₃ plasma. (a) Ar⁺ and ArH⁺, (b) NH₄⁺, NH₃⁺ and NH₂⁺, (c) H₃⁺, H₂⁺ and H⁺. The plasma source current was 70 A and the Ar flow was 55 sccs. The ions were extracted from the plasma at a distance of 56 cm from the source. The lines serve as a guide to the eye.

6(c) show that the signals due to NH_x⁺ ions (x=2–4) and H₃⁺ and H⁺ follow approximately the same trend versus the NH₃ flow with a plateau in the ion signals between 0.5 and 1.5 sccs NH₃ and an exponential decrease for higher flows. This decrease can be attributed to dissociative recombination reactions as mentioned above, leading to NH_x (x=0–2) radical species that will be discussed in the next section. Overall, it can be concluded that the most abundant ion species in the Ar–NH₃ plasma changes from Ar⁺ for flows below 0.25 sccs NH₃ to ArH⁺ for intermediate flows and subsequently to ArH⁺, NH₂⁺, NH₃⁺, NH₄⁺, and H₃⁺ for NH₃ flows higher than 1 sccs.

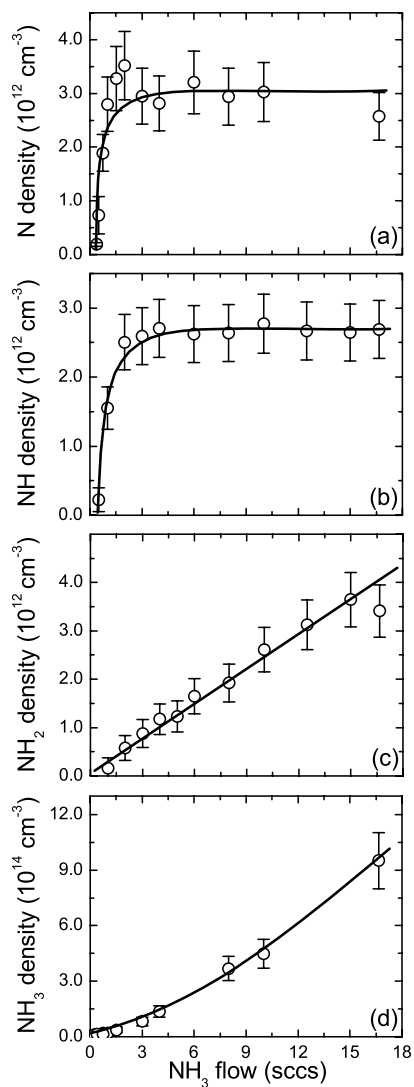


Figure 7: The density of (a) N, (b) NH, (c) NH_2 and (d) NH_3 in the ETP plasma as a function of the NH_3 flow. The measurements took place at a distance of 36 cm and 56 cm from the plasma source for the cavity ringdown (NH and NH_2) and (threshold ionization) mass spectrometry (N and NH_3) measurements respectively. The Ar flow was 55 sccs and the plasma source current was 45 A. The lines serve as a guide to the eye.

Radical species in the Ar- NH_3 plasma

Figure 7 shows the densities of the N, NH and NH_2 radicals produced in the plasma as measured by threshold ionization mass spectrometry and cavity ring-down

spectroscopy. The N density increases very fast initially and saturates at a level of $\sim 3 \times 10^{12} \text{ cm}^{-3}$ at an injected NH_3 flow of ~ 3 sccs. The NH density shows a similar behaviour as the N density, but reaches a level of $2.7 \times 10^{12} \text{ cm}^{-3}$ for NH_3 flows above 3 sccs. The NH_2 density on the other hand does not saturate and shows a linear increase as a function of the NH_3 flow. The value of the NH_2 density is $\sim 4.0 \times 10^{12} \text{ cm}^{-3}$ for an injected NH_3 flow of 17 sccs. Remarkably, the radicals N, NH and NH_2 all reach a similar density in the Ar- NH_3 plasma of $2\text{--}4 \times 10^{12} \text{ cm}^{-3}$ for a high NH_3 flow. However, on the basis of their density no conclusion can be drawn about the relative importance of the different ammonia radical species for materials processing.

In Fig. 7(d) also the density of NH_3 as measured by mass spectrometry is given as a function of the NH_3 flow. The NH_3 density is much higher than the NH_x radical densities and as expected, the NH_3 density in the plasma increases approximately linearly as a function of the injected NH_3 flow, except in the low flow region where the consumption of NH_3 in the plasma is substantial.

The production and loss reactions ruling the NH and NH_2 densities in the Ar- NH_3 plasma have been discussed extensively in a previous publication [22]. Clearly, the trend of the N density as a function of NH_3 flow is very similar to the trend of the NH density which suggests that they are produced by the same reaction mechanism. Both N and NH are therefore most likely direct products of the charge transfer and dissociative recombination reaction sequence discussed above. For a NH_3 flow of 3 sccs, approximately all Ar^+ ions emanating from the plasma source are consumed (in agreement with the estimated flow of ~ 3.5 sccs Ar^+ deduced from the Langmuir probe measurements) leading to a saturation in the N and NH density. The fact that N and NH remain constant at high NH_3 flows also implies that gas-phase loss of these radicals can be neglected. The behavior of the NH_2 density versus NH_3 flow is completely different, which suggests a different NH_2 production mechanism involving ion-molecule reactions and possibly hydrogen abstraction reactions as discussed in detail in reference 22.

NH_3 consumption and production of stable species.

From Fig. 7(d) it was already seen that the NH_3 consumption at low NH_3 flows is substantial. In Fig. 8(a) the decrease in NH_3 density when the plasma is switched on is plotted. In the low flow regime, the decrease in NH_3 density is proportional to the injected NH_3 flow, while for flows higher than ~ 6 sccs the decrease in NH_3 density saturates at value of $2.7 \times 10^{14} \text{ cm}^{-3}$. This clearly demonstrates that the amount of NH_3 that can be dissociated by the plasma is most likely limited by the ion density emanating from the plasma source. From the data, also the relative NH_3 consumption can be calculated. For the present conditions (55 sccs Ar flow, 45 A plasma current and 0.20 mbar pressure), the relative consumption of NH_3 is close to 75 % for a NH_3

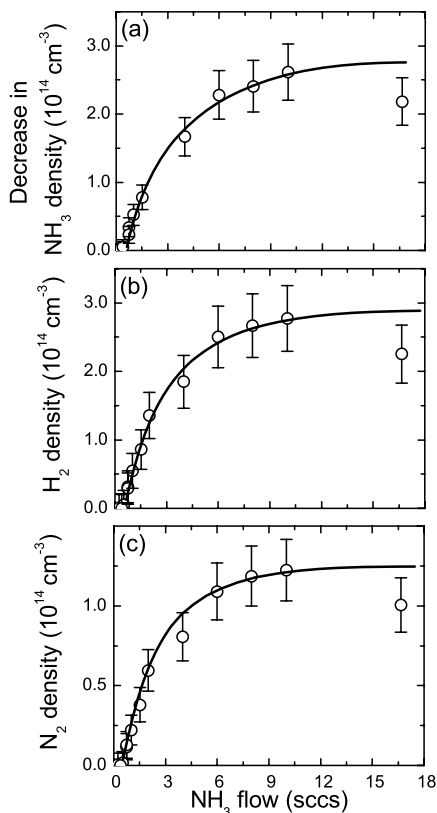


Figure 8: (a) The decrease in NH₃ density and the produced density of (b) H₂ and (c) N₂ molecules when the Ar–NH₃ plasma is switched on. The plasma source current was 45 A and the Ar flow was 55 sccs. The lines serve as a guide to the eye.

flow of 1 sccs and 20 % for a NH₃ flow of 17 sccs. When multiplying this relative consumption with the NH₃ flow injected it is found that a maximum flow of ~ 3.4 sccs NH₃ is consumed by the plasma. This flow is approximately equal to the Ar⁺ ion flow emanating from the plasma source, which suggests that regeneration of NH₃ molecules in the plasma plays only a minor role.

The amount of NH₃ consumed in the plasma is two orders of magnitude larger than the typical NH_x radical densities generated. Because the NH_x species in an Ar–NH₃ plasma do not accumulate at the walls – as is for example the case in a depositing plasma – other species need to be generated in the plasma. The most likely candidates are H₂ and N₂ molecules that can be formed in the plasma itself or by wall association of plasma produced fragments. Figures 8 (b) and 8 (c) show the densities of H₂ and N₂ produced in the plasma as a function of the NH₃ flow. The

produced H_2 and N_2 density show a similar trend as the decrease in NH_3 density and they saturate at densities of $\sim 2.9 \times 10^{14} \text{ cm}^{-3}$ for H_2 and $1.2 \times 10^{14} \text{ cm}^{-3}$ for N_2 . The amounts of H_2 and N_2 produced in the Ar- NH_3 plasma are very high and can account for most of the consumed NH_3 molecules. Neglecting the relatively small NH_x densities ($\sim 10^{12} \text{ cm}^{-3}$ versus $\sim 10^{14} \text{ cm}^{-3}$ for H_2 and N_2), a ratio between the consumed NH_3 density and the produced H_2 and N_2 density of 2 : 3 : 1 is expected in the plasma. Our results give a ratio of 2.0 : 2.1 : 0.9 which is in fair agreement with the expectation. The fact that the measured amount of H_2 is lower than expected can most probably be attributed to the difficulty in calibrating H_2 signals with mass spectrometry and/or more effective pumping of H_2 due to its higher conductance.

B. Influence of plasma current

So far we discussed almost only results obtained at a plasma current of 45 A. The plasma current is however a parameter which has a large influence on the amount of reactive species produced by the plasma source. As mentioned earlier, the flow of Ar^+ ions emanating from the plasma source increases linearly with the plasma current. Therefore the densities of N, NH, and NH_2 produced in the Ar- NH_3 plasma were investigated as a function of the plasma source current as shown in Figs. 9(a) to 9(c). The Ar and NH_3 flows were 55 and 17 sccs, respectively and the pressure was 0.20 mbar. The amount of NH_3 consumed in terms of the decrease in NH_3 density is given in Fig. 9(d).

From Fig. 9, it is clear that the consumption of NH_3 is linear with the plasma current leading to a linear increase of the N and NH densities produced in the plasma. For N radicals a density of $\sim 4 \times 10^{12} \text{ cm}^{-3}$ is reached for a plasma current of 70 A while the NH density goes up to $\sim 5 \times 10^{12} \text{ cm}^{-3}$. These observations are in agreement with the fact that the production mechanism for N and NH is Ar^+ ion dominated as argued in section III.A. The NH_2 density however, increases only slightly and then remains constant at a value of $\sim 6 \times 10^{12} \text{ cm}^{-3}$ for high plasma currents. The fact that this trend deviates from those of the N and NH densities confirms that the reaction mechanism determining the NH_2 density is considerably different from the mechanism that governs the N and NH density.

The densities of H_2 and N_2 produced in the plasma (not shown) are also linear with the plasma current, which is in agreement with the linearly increasing NH_3 consumption. When the plasma current is increased from 30 to 70 A, the consumption increases from 15 % to approximately 60 % and the equivalent flow of consumed NH_3 increases from ~ 2.5 to ~ 10 sccs. This reveals that the plasma current is an important parameter to increase the flux of reactive species in the Ar- NH_3 plasma albeit that a large fraction of consumed NH_3 is converted into H_2 and N_2 .

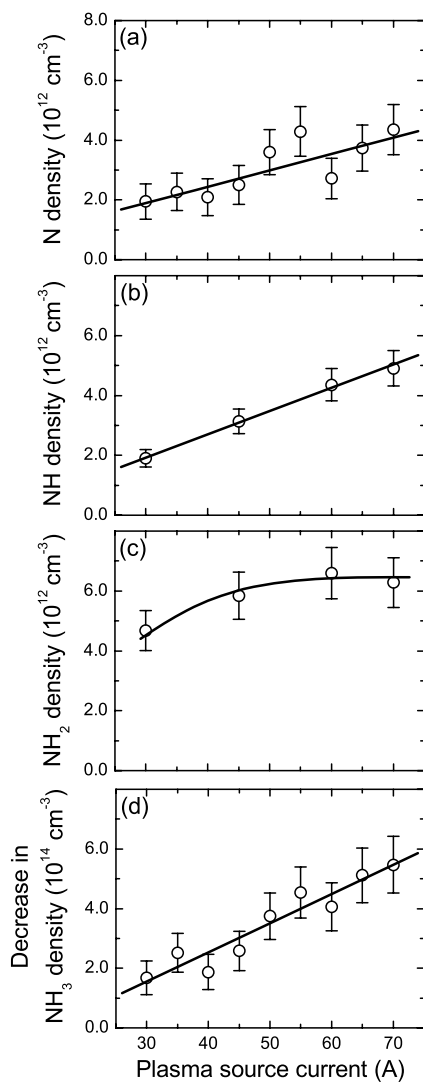


Figure 9: The (a) N, (b) NH, (c) NH_2 density as a function of the plasma source current as well as (d) the decrease in NH_3 density in the Ar- NH_3 plasma. The Ar and NH_3 flows were 55 and 17 sccs, respectively. The lines serve as a guide to the eye.

IV. Concluding remarks

The Ar-NH₃ plasma generated by the expanding thermal plasma source, applied industrially for silicon nitride deposition for solar cells and moisture diffusion barriers, was investigated extensively. From a combination of Langmuir probe measurements, cavity ring-down spectroscopy and (threshold ionization) mass spectrometry valuable information on the absolute density of the most important species in the Ar-NH₃ plasma was obtained:

- The ion density decreases from 10^{13} cm^{-3} in a pure Ar plasma to 10^{10} – 10^{11} cm^{-3} when NH₃ is injected in the plasma. For no or very low NH₃ flows, Ar⁺ and ArH⁺ are the most abundant ions in the plasma while ArH⁺, NH₂⁺, NH₃⁺, NH₄⁺ and H₃⁺ are more important at higher NH₃ flows.
- The density of N and NH both saturate at a level of $\sim 3 \times 10^{12} \text{ cm}^{-3}$ for NH₃ flows above 3 sccs while the density of NH₂ increases linearly with the NH₃ flow and reaches a level of $\sim 4 \times 10^{12} \text{ cm}^{-3}$. The densities of ammonia radicals are apparently all similar in magnitude.
- The density of N and NH increase linearly when increasing the plasma current from 30 to 70 A while the NH₂ density shows a slight increase and subsequently remains constant.
- A high degree of NH₃ consumption is reached at low NH₃ flows while at higher NH₃ flows the dissociation of NH₃ saturates due to the limited amount of Ar⁺ ions available. By far most of the consumed NH₃ is converted into N₂ and H₂ molecules in the plasma.

Acknowledgments

The authors thank M.J.F. van de Sande, J.F.C. Jansen, A.B.M. Hüsken, and H.M.M. de Jong for their skillful technical assistance. C.C.H. Lamers is gratefully acknowledged for her contribution to the measurements and J. Benedikt is acknowledged for the design and building of the TIMS setup. This study has been supported by the Netherlands Foundation for Fundamental Research on Matter (FOM) and by the Netherlands Ministry of Economic Affairs, the Ministry of Education, Culture and Science and the Ministry of Public Housing, Physical Planning and Environment (E.E.T.–project “HR–CEL”). The research of W.K. has been made possible by a fellowship of the Royal Netherlands Academy of Arts and Sciences (KNAW).

References

- [1] D.C. Schram and G.W.M. Kroesen, U.S. Patent No. 4,871,580 (1989); European Patent No. 0297637 (1992).
- [2] W.M.M. Kessels, R.J. Severens, A.H.M. Smets, B.A. Korevaar, G.J. Adriaenssens, D.C. Schram, and M.C.M. van de Sanden, *J. Appl. Phys.* **89**, 2404 (2001).
- [3] C. Smit, A. Klaver, B.A. Korevaar, A.M.H.N. Petit, D.L. Williamson, R.A.C.M.M. van Swaaij and M.C.M. van de Sanden, *Thin Solid Films* **491**, 280 (2005).
- [4] M. Creatore, J.-C. Cigal, G.M.W. Kroesen and M.C.M. van de Sanden, *Thin Solid Films* **484**, 104 (2005).
- [5] J. Benedikt, D.J. Eijkman, W. Vandamme, S. Agarwal and M.C.M. van de Sanden, *Chem. Phys. Lett.* **402**, 37 (2005).
- [6] R. Groenen, H. Linden and R. van de Sanden, *Plasma Processes and Polymers* **2**, 618 (2005).
- [7] W.M.M. Kessels, F.J.H. van Assche, J. Hong, D.C. Schram and M.C.M. van de Sanden, *J. Vac. Sci. Technol. A* **22**, 96 (2004).
- [8] B. Hoex, A.J.M. van Erven, R.C.M. Bosch, W.T.M. Stals, M.D. Bijker, P.J. van den Oever, W.M.M. Kessels and M.C.M. van de Sanden, *Progress in Photovoltaics* **13**, 705 (2005).
- [9] Y. Barrell, M. Creatore, M. Schaepkens, C.D. Iacovangelo, T. Miebach and M.C.M. van de Sanden, *Surface and Coatings Technology* **180–181**, 367 (2004).
- [10] W.M.M. Kessels, P.J. van den Oever, R.C.M. Bosch, M.D. Bijker, M. Evers, D.C. Schram and M.C.M. van de Sanden, *High Temperature Material Processes* **9**, 141 (2005).
- [11] M. Schaepkens, T.W. Kim, A.G. Erlat, M. Yan, K.W. Flanagan, C.M. Heller and P.A. McConnelee, *J. Vac. Sci. Technol. A* **22**, 1716 (2004).
- [12] F.J.H. van Assche, W.M.M. Kessels, R. Vangheluwe, W.S. Mischke, M. Evers and M.C.M. van de Sanden, *Thin Solid Films* **484**, 46 (2005).
- [13] E.S. Aydil, K.P. Giapis, R.A. Gottscho, V.M. Donnelly and E. Yoon, *J. Vac. Sci. Technol. B* **11**, 195 (1993).
- [14] N. Inagaki, K. Narushim, N. Tsuchida and K. Miyazaki, *Journal of Polymer Science B* **42**, 3727 (2004).
- [15] M. Crombez, P. Chevallier, R.C. Gaudreault, E. Petitclerc, D. Mantovani and G. Laroche, *Biomaterials* **26**, 7402 (2005).
- [16] M.S. Bell, R.G. Lacerda, K.B.K. Teo, N.L. Rupesinghe, G.A.J. Amaratunga, W.I. Milne and M. Chhowalla, *Appl. Phys. Lett.* **85**, 1137 (2004).
- [17] G.P. Miller and J.K. Baird, *J. Phys. Chem.* **97**, 10984 (1993).
- [18] S.D. Pringle, V.S. Joss and C. Jones, *Surface and Interface Analysis* **24**, 821 (1996).

- [19] E.R. Fisher, P. Ho, W.G. Breiland and R.J. Buss, *J. Phys. Chem.* **96**, 9855 (1992).
- [20] P.R. McCurdy, C.I. Butoi, K.L. Williams and E.R. Fisher, *J. Phys. Chem. B* **103**, 6919 (1999).
- [21] M L Steen, K R Kull and E R Fisher, *J. Appl. Phys.* **92**, 55 (2002).
- [22] P.J. van den Oever, J.H. van Helden, C.C.H. Lamers, R. Engeln, D.C. Schram, M.C.M. van de Sanden and W.M.M. Kessels, *J. Appl. Phys.* **98**, 093301 (2005) ; Chapter 2.
- [23] M.C.M. van de Sanden, J.M. de Regt and D.C. Schram, *Plasma Sources Sci. Technol.* **3**, 501 (1994).
- [24] A.J.M. Buuron, D.K. Otorbaev, M.C.M. van de Sanden and D.C. Schram, *Phys. Rev. E* **50**, 1383 (1994).
- [25] M.C.M. van de Sanden, R.J. Severens, W.M.M. Kessels, R.F.G. Meulenbroeks and D.C. Schram, *J. Appl. Phys.* **84**, 2426 (1998); *J. Appl. Phys.* **85**, 1243 (1999).
- [26] M.F.A.M. van Hest, J.R. Haartsen, M.H.M. van Weert, D.C. Schram and M.C.M. van de Sanden, *Plasma Sources Sci. Technol.* **12**, 539 (2003).
- [27] G.J.H. Brussaard, M. van der Steen, M. Carrère, M.C.M van de Sanden and D.C. Schram, *Phys. Rev. E* **54**, 1906 (1996).
- [28] E.W. Peterson and L. Talbot, *AIAA Journal* **8**, 2215 (1970).
- [29] G.J.H. Brussaard, Remote arc generated plasma in diatomic gases, PhD Thesis Eindhoven University of Technology (1999).
- [30] J.P.M. Hoefnagels, Y. Barrell, W.M.M. Kessels and M.C.M. van de Sanden, *J. Appl. Phys.* **96**, 4096 (2004).
- [31] W.M.M. Kessels, A. Leroux, M.G.H. Boogaarts, J.P.M. Hoefnagels, M.C.M. van de Sanden and D.C. Schram, *J. Vac. Sci. Technol. A* **19**, 467 (2001).
- [32] J. Benedikt, S. Agarwal, D. Eijkman, W. Vandamme, M. Creatore and M.C.M. van de Sanden, *J. Vac. Sci. Technol. A* **23**, 1400 (2005).
- [33] Kim Y –K and Desclaux J P 2002 *Phys. Rev. A* **66** 012708
- [34] Rosenstock H M, Draxl K, Steiner B W and Herron J T 1977 *Journal of Physical and Chemical Reference Data Vol 6, Supplement No. 1* (Washington: National Bureau of Standards)
- [35] H. Singh, J.W. Coburn and D.B. Graves, *J. Vac. Sci. Technol. A* **18**, 299 (2000).
- [36] Y–K. Kim and J.P. Desclaux, *Phys. Rev. A* **66**, 012708 (2002).
- [37] V. Tarnovsky, H. Deutsch and K. Becker, *International Journal of Mass Spectrometry and Ion Processes* **167–168**, 69 (1997).
- [38] T.D. Märk, F. Egger and M. Cheret, *J. Chem. Phys.* **67**, 3795 (1977).
- [39] H. Singh, J.W. Coburn and D.B. Graves, *J. Appl. Phys.* **88**, 3748 (2000).
- [40] R. Engeln, S. Mazouffre, P. Vankan, D.C. Schram and N. Sadeghi, *Plasma Sources Sci. Technol.* **10**, 595 (2001).

- [41] W.M.M. Kessels, C.M. Leewis, M.C.M. van de Sanden and D.C. Schram, *J. Appl. Phys.* **86**, 4029 (1999).
- [42] R. Derai, G. Mauclaire, and R. Marx, *Chem. Phys. Lett.* **86**, 275 (1982).
- [43] J. Perrin, O. Leroy and M.C. Bordage, *Contributions to Plasma Physics* **36**, 3 (1996).

Chapter 4

N, NH and NH₂ radical densities in a remote Ar–NH₃–SiH₄ plasma and their role in silicon nitride deposition *

The densities of N, NH and NH₂ radicals in a remote Ar–NH₃–SiH₄ plasma used for high–rate silicon nitride deposition were investigated for different gas mixtures and plasma settings using cavity ring–down absorption spectroscopy and threshold ionization mass spectrometry. For typical deposition conditions, the N, NH and NH₂ radical densities are in the order of 10¹² cm^{–3} and the trends with NH₃ flow, SiH₄ flow and plasma source current are reported. We present a feasible reaction pathway for the production and loss of the NH_x radicals that is consistent with the experimental results. Furthermore, mass spectrometry revealed that the consumption of NH₃ was typically 40 %, while it was over 80% for SiH₄. On the basis of the measured N densities we deduced the recombination and sticking coefficient for N radicals on a silicon nitride film. Using this sticking coefficient and reported surface reaction probabilities of NH and NH₂ radicals, we conclude that N and NH₂ radicals are mainly responsible for the N incorporation in the silicon nitride film, while Si atoms are most likely brought to the surface in the form of SiH_x radicals.

* Published as: P.J. van den Oever, J.H. van Helden, J.L. van Hemmen, R. Engeln, D.C. Schram, M.C.M. van de Sanden, and W.M.M. Kessels, *J. Appl Phys.* **100**, 093303 (2006).

I. Introduction

Plasma deposited amorphous silicon nitride ($a\text{-SiN}_x\text{:H}$) thin films have been studied extensively because of their electrical and optical properties that make them very suitable for many applications in microelectronics device fabrication (e.g., as gate dielectric or passivation layer [1–3]). Other applications can be found in the encapsulation of devices such as organic light emitting devices [4] and in the photovoltaic industry, where $a\text{-SiN}_x\text{:H}$ is used as an antireflection coating on $c\text{-Si}$ solar cells that also serves as a surface and bulk passivation layer to improve the carrier lifetime in silicon [5,6]. Most silicon nitride deposition processes use mixtures of SiH_4 and NH_3 or N_2 , but also liquid precursors like hexamethyldisilazane (HMDS), tris(diethylamino)chlorosilane (TDEACS) and bis(dimethylamino)–dimethylsilane (BDMADMS) have been used with varying success [7–9].

Because of their numerous applications, silicon nitride films deposited by plasma enhanced chemical vapor deposition (PECVD) have been widely investigated and the dependence of the film properties on the plasma gas composition and deposition conditions was established in various types of plasma reactors [10–13]. However, due to the complexity of chemical reactions both in the gas phase and at the surface, the mechanisms underlying silicon nitride deposition are not yet fully understood and further knowledge of the processes taking place in the plasma is still required. For $\text{N}_2\text{-SiH}_4$ plasmas several studies of the silicon nitride growth mechanism were reported. In 1990 Smith *et al.* found that N radicals are probably directly incorporated in the $a\text{-SiN}_x\text{:H}$ film [14], while Hanyaloglu and coworkers (1998) suggested on the basis of optical emission spectroscopy that excited N_2^* molecules are most likely responsible for the N incorporation in the $a\text{-SiN}_x\text{:H}$ films [15]. Recently, more support for the incorporation of N radicals in the $a\text{-SiN}_x\text{:H}$ film was found in a remote $\text{Ar-N}_2\text{-H}_2\text{-SiH}_4$ plasma and a refined growth mechanism was proposed. In this refined growth mechanism an $a\text{-Si:H}$ -like surface layer formed by predominantly SiH_3 radicals is converted into $a\text{-SiN}_x\text{:H}$ by nitridation reactions with impinging N radicals [16, 17].

On the other hand, Smith and coworkers identified the amino–silane radical as the most important precursor for silicon nitride deposition in a $\text{NH}_3\text{-SiH}_4$ radiofrequency plasma using mass spectrometry [11,18]. This result was supported by Beach and Jasinski (1990) who proposed a reaction mechanism for the formation of amino–silane radicals involving NH_2 radicals [19]. In 1995, Murley *et al.* showed that the amount of amino–silanes formed is dependent on the gas residence time inside the reactor chamber [20]. Long residence times typically lead to high amino–silane concentrations, whereas short residence times result in no amino–silanes at

all, which suggests the existence of a complementary growth mechanism most likely based on SiH_x and NH_x radicals under short-residence-time conditions.

For $\alpha\text{-SiN}_x\text{H}$ growth based on $\text{NH}_3\text{-SiH}_4$ gas mixtures, the role and densities of N, NH and NH_2 radicals has not been investigated in great detail. The results of Theil *et al.* (1992) suggest that SiH_x and NH_x radicals are more important for silicon nitride growth than the amino-silane radicals [21], although they did not measure these radicals directly. More recently Umemoto and coworkers measured NH, NH_2 and SiH_3 radicals in a hotwire chemical vapor deposition (CVD) process and they found that SiH_3 and NH_2 are most likely responsible for the Si and N incorporation in the film [22]. The density and role of N radicals in $\text{NH}_3\text{-SiH}_4$ based plasmas, however, is not well known as limited studies into this subject have been reported.

Further insight into the silicon nitride growth mechanism can be inferred from the interaction of the various NH_x radicals with the surface, which was studied by several research groups. Fisher *et al.* measured the surface interaction of NH and NH_2 radicals for different types of surfaces using laser induced fluorescence combined with a molecular beam setup [23–25]. For N radicals on stainless steel and silicon nitride surfaces, the surface reactivity has been summarized and extended by Kessels *et al.* [17] based on the experimental results of Adams and Miller [26] and Singh and coworkers [27].

In this Chapter, we report the densities of the NH_x radicals in a remote Ar- $\text{NH}_3\text{-SiH}_4$ plasma and we focus on the role of these radicals in the deposition process of silicon nitride. In Sec. II, the expanding thermal plasma (ETP) technique operated on an Ar- NH_3 gas mixture [28] is briefly described. This technique was recently introduced in industry [29, 30] and is capable of depositing good quality silicon nitride at nominal deposition rates ranging from 4 to 7 nm/s, which is faster than most conventional processes (< 1 nm/s). The diagnostic techniques, such as cavity ring-down absorption spectroscopy (CRDS) for the detection of NH and NH_2 radicals and threshold ionization mass spectrometry (TIMS) for the N radical measurements are described briefly in Sec. III. In Sec. IV, we present the NH_x radical densities as function of several plasma parameters such as NH_3 flow, SiH_4 flow and plasma source current (Sec. IV.A–IV.C) and discuss the most important plasma reactions that can explain the observed trends. Furthermore, the NH_3 and SiH_4 consumption and the production of molecules from the dissociated molecules (Sec. IV.D) are addressed for different plasma settings. Subsequently, Sec. V summarizes the plasma chemistry and discusses the surface reaction probability of the NH_x radicals and the implications of our measurements on the silicon nitride growth mechanism. Finally, the conclusions are given in Sec. VI.

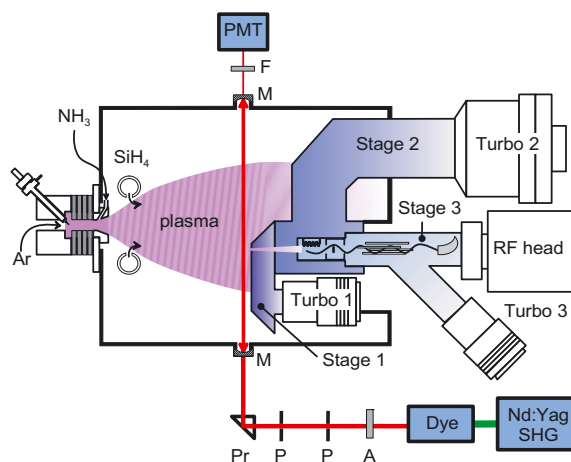


Figure 1: The experimental setup, showing the cascaded arc plasma source, the cavity ringdown setup and the threshold ionization mass spectrometer. In the figure “F” stands for filter, “M” for mirror, “Pr” for prism, “P” for pinhole, and “A” for attenuator.

II. The expanding thermal plasma on Ar–NH₃

Figure 1 shows a schematic overview of the deposition setup including the laser setup used for the measurements of the NH and NH₂ densities and the mass spectrometry setup for the determination of the N density. Both diagnostic techniques will be discussed in greater detail in the Sec. III.

An extensive description of the plasma source and the Expanding Thermal Plasma (ETP) technique can be found elsewhere [28,31,32] and here a brief summary of the ETP plasma operated on an Ar–NH₃ mixture will be given. The ETP technique consists of a cascaded arc plasma source that operates at sub-atmospheric pressures (~300 mbar) and a low pressure processing chamber. A DC current of typically 45 A is used to efficiently ionize argon atoms in a narrow plasma channel with flowing argon gas. NH₃ gas is introduced through a slit in the nozzle at the outlet of the plasma source (see Fig. 1) and the resulting Ar–NH₃ plasma expands into the low pressure chamber (~0.20 mbar). The electron temperature is low (0.2–0.3 eV) in the expansion and as a consequence, electron impact induced chemistry and ion bombardment due to the plasma self bias potential are not important. The most important reactive species emanating from the plasma source are Ar⁺ ions that transfer their charge to NH₃ molecules in the course of the expansion, creating mainly NH₃⁺ molecular ions. These molecular ions recombine dissociatively with electrons into mainly N and NH radicals [33]. The charge transfer reaction as well as the dissociative recombination reaction is very fast and the N and NH densities both

Table 1: The range of plasma parameters used in this study.

Parameter	Standard value	Range studied
Ar flow	55 sccs	---
NH ₃ flow	17 sccs	0–17 sccs
SiH ₄ flow	2.5 sccs	0–5 sccs
Arc current	45 A	30–70 A
Arc voltage	42 V	---
Arc pressure	280 mbar	---
Downstream pressure	0.20 mbar	---

saturate at a level of $3 \times 10^{12} \text{ cm}^{-3}$ for NH₃ flows above 3 sccs due to the limited amount of Ar⁺ ions available. Langmuir probe measurements carried out at 36 cm from the plasma source revealed an exponential decrease of the ion density by three orders of magnitude until 3 sccs NH₃ was injected in the plasma [28], which is in line with the constant N and NH densities above 3 sccs NH₃. The saturation also implies that gas phase loss with NH₃ can be neglected for these radicals. NH₂ radicals, on the other hand, are most likely produced differently via reactions of NH₃⁺ with NH₃ or via NH₃ dissociation reactions by H abstraction, resulting in a linear increase of the NH₂ density as a function of the NH₃ flow. The NH₂ density reached for 15 sccs injected NH₃ flow is approximately $4.0 \times 10^{12} \text{ cm}^{-3}$. More information on the reaction mechanism responsible for the creation of NH and NH₂ in the Ar–NH₃ plasma can be found in Ref. 33.

When the plasma is used for silicon nitride deposition SiH₄ gas is injected through a ring situated at a distance of approximately 8 cm from the nozzle. The reactive fragments (NH_x, H, etc) created in the initial part of the expansion are used to dissociate the injected SiH₄ leading to silicon containing reactive species that deposit an a–SiN_x:H film on a downstream situated substrate. The standard experimental conditions and the parameter range used in this study are given in Table 1.

III. Plasma diagnostics

A. Cavity ring–down absorption spectroscopy

The cavity ring–down setup is shown schematically in Fig. 1. Laser pulses generated by a dye laser pumped by the second harmonic radiation of a Nd:YAG laser, were injected into a high finesse optical cavity formed by two plano–concave high reflectivity mirrors (M). The mirrors, protected from reactive plasma species by a small argon flow, were placed 112 cm apart on flexible bellows at a distance of 36 cm from the plasma source, which is 3 cm before the substrate holder. Before injection into

the cavity, the laser pulse energy was attenuated to below 100 μJ per pulse to avoid optical saturation of the used transitions. The light intensity leaking out of the cavity was detected through an interference bandpass filter (F) by a photomultiplier tube (PMT). For every single laser pulse, the decay rate was sampled by a 100 MHz, 12 bits data acquisition system (TU/eDACS [34]). All observed decay rates were single-exponential and were analyzed by a weighted least squares fit of the logarithm of the transient data, while an average of 20 single decays was used to improve the signal to noise ratio. More details on the cavity ring-down setup can be found elsewhere [33].

The NH radical was detected on the (0,0) band of the $A^3\Pi \leftarrow X^3\Sigma^-$ transition around ~ 340 nm and the NH_2 radical on the (0,9,0)–(0,0,0) band of the $\tilde{A}^2A_1 \leftarrow \tilde{X}^2B_1$ transition at ~ 597 nm. For NH, the isolated $P_{3,3}(9)$ absorption line at 339.62 nm (29444.28 cm^{-1}) was used, while the “isolated” $\Sigma^P Q_{1,N}(7)$ absorption line at 597.38 nm (16739.90 cm^{-1}) was used for NH_2 . The actual density information was determined by scanning the laser over the particular absorption line and using the integrated absorption cross-sections derived in Ref. 33.

First, the spectra of NH and NH_2 were recorded for the Ar– NH_3 plasma to establish the measurement procedure. We found that the addition of SiH_4 to the plasma introduced a broadband absorption in addition to the NH and NH_2 spectral features. The origin of this broadband absorption has not been identified, but it did not change the distinct spectral features of the NH and NH_2 radical. The largest uncertainty in the absolute values of the densities reported is generated by the assumption about the absorption path length for the radicals in the plasma, which is estimated to be 30 cm [35]. This systematic error can be as large as a factor of three for the local absolute densities.

B. (Threshold ionization) mass spectrometry

The triple stage differentially pumped quadrupole mass spectrometer (QMS) used in this study was modified from the version that was used to measure N radicals in an Ar– N_2 – SiH_4 plasma [16]. The apparatus used in this study is based on the design by Agarwal *et al.* [36] and was described extensively elsewhere [28,37]. Briefly, the plasma is sampled by effusive extraction through a 0.8 mm orifice that is situated approximately 56 cm from the plasma source and 4.5 cm off the reactor axis. The extraction creates a molecular beam that passes two consecutive orifices separating the pumping stages in the housing of the mass spectrometer. The quadrupole mass spectrometer (Hiden Analytical Epic 300, PSM upgrade) is placed in the third stage, in line-of-sight with the three orifices. Typical pressures in the second and third stage during measurements are 10^{-6} mbar and 10^{-7} mbar, while the third stage base pressure is below 10^{-9} mbar. Due to the finite pressure in the third

Table 2: Various reactions leading to N^+ ions in the mass spectrometer’s ionizer by electron impact ionization. The literature values for the appearance potentials are also given.

	Process	Appearance potential	Reference
A	$N + e \rightarrow N^+ + 2e$	15.3 eV	Kim <i>et al.</i> [38]
B	$NH_3 + e \rightarrow N^+ + H_2 + H + 2e$	22.6 eV	Rosenstock <i>et al.</i> [39]
C	$N_2 + e \rightarrow N^+ + N + 2e$	24.3 eV	Rosenstock <i>et al.</i> [39]

stage, the mass spectrometer signal will not only consist of a beam component, but also of a background component due to surface scattered molecules.

Ground state N radicals were detected using the so called threshold ionization or appearance potential technique [14,28]. In general, electron impact ionization of radicals has a lower threshold than dissociative ionization of parent molecules leading to the same ion. Table 2 shows the different electron impact ionization processes that lead to the detection of an ion with a mass-over-charge (m/e) ratio equal to 14. By scanning the electron energy used for ionization, we can distinguish different ionization processes. To obtain absolute densities of N radicals, we used a calibration method for the N radicals similar to the one described by Singh and coworkers [27]. The absolute N densities were obtained by correlating the measured signal of N radicals to the direct ionization signal of NH_3 reference gas with a known number density. The details of the calibration procedure can be found in Ref. 28.

The mass spectrometer was also used to determine the densities of stable species such as NH_3 , SiH_4 , H_2 and N_2 in the plasma beam. The calibration procedure to obtain the absolute densities of these molecules was carried out prior to each measurement run using different reference gas mixtures in argon (e.g. NH_3 in Ar, SiH_4 in Ar, etc.) to mimic the actual measurement conditions. From these measurements the relative consumption or depletion of a species can be calculated.

For the Ar- NH_3 - SiH_4 plasma, all signals were corrected for clogging of the sampling orifice by normalizing all signals to the Ar signal in the ‘plasma off’ case. This correction was not necessary for non-depositing plasmas.

IV. Results

A. NH_x radical densities versus NH_3 flow

Figures 2 (a–d) show the absolute densities of N, NH and NH_2 radicals and NH_3 molecules in the expanding Ar- NH_3 - SiH_4 plasma as a function of the NH_3 flow for a SiH_4 flow of 2.5 sccs (circles). The observed trends for a pure Ar- NH_3 plasma (described in Sec. II) are also shown for comparison (triangles). When 2.5 sccs SiH_4 is

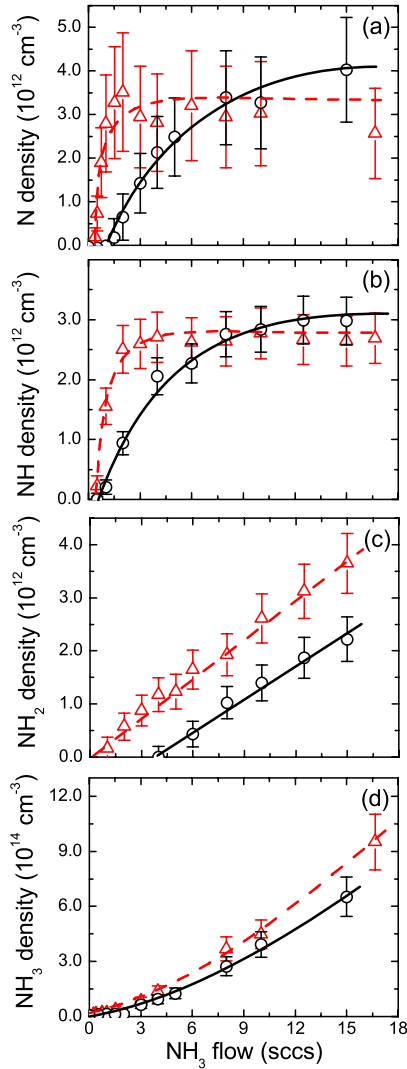


Figure 2: The N (a), NH (b), NH_2 (c) and NH_3 (d) densities as a function of the NH_3 flow for an injected SiH_4 flow of 0 sccs (open triangles, dashed line) and 2.5 sccs (open circles, solid line). The arc current was 45. The N and NH_3 densities were measured by (threshold ionization) mass spectrometry and the NH and NH_2 densities by cavity ringdown spectroscopy. The lines serve as a guide to the eye.

added to the Ar- NH_3 plasma, the behavior of the NH_x ($x = 0-3$) densities is quite similar to the situation without SiH_4 as can be seen in Fig. 2. The N and NH densities increase more gradual to their final values of $\sim 4.0 \times 10^{12} \text{ cm}^{-3}$ and $\sim 3.0 \times 10^{12} \text{ cm}^{-3}$

respectively. Also the NH_2 density shows a similar linear increase as in the case without SiH_4 reaching a density of $2.5 \times 10^{12} \text{ cm}^{-3}$ at 15 sccs NH_3 . For NH_3 flows below 4 sccs, however, no NH_2 radicals could be detected in the plasma in contrast to the situation without SiH_4 . The NH_3 density obtained for 15 sccs NH_3 flow is $7.0 \times 10^{14} \text{ cm}^{-3}$, which is slightly lower than in the situation without SiH_4 .

The observed density changes can be qualitatively understood by looking at the production rate P and and loss time τ of species in a steady state situation:

$$\frac{\partial n}{\partial t} = P - \frac{n}{\tau} = 0, \quad (1)$$

with n the density of the species. In this case, the observed *gradual* increase of the N and NH density can be explained by a decrease in the production rate of these radicals due to SiH_4 injection. Competition between charge transfer reactions of Ar^+ ions with NH_3 , responsible for the creation of N and NH radicals, and with SiH_4 results in a lower production rate for N and NH. This effect is especially important when the NH_3 flow is comparable to or smaller than the SiH_4 flow, as is also observed in Fig. 2 (a) and (b). For high NH_3 flows the influence of the charge transfer reaction of Ar^+ with SiH_4 is of minor importance and the observed N and NH densities are similar to the values obtained in the situation without SiH_4 . The final N radical density seems to be somewhat higher in the presence of SiH_4 , which is predominantly caused by a change in the loss time of the N radical [e.g., a different surface reaction probability (see Sec. V.B.)]. The absence of NH_2 radicals in the Ar- NH_3 - SiH_4 plasma for flows below 4 sccs NH_3 is another indication that the production and/or loss mechanism of NH_2 is different than that of N and NH. Additional measurements showed that the NH_3 flow threshold for NH_2 detection depends linearly on the SiH_4 flow. This behavior is not completely understood yet, but a few mechanisms affecting the production or the loss time of NH_2 radicals can be suggested. A first possibility is the abstraction reaction between atomic H and SiH_4 . This reaction is much faster at 1750 K [33] (reaction rate $\sim 8 \times 10^{-11} \text{ cm}^3 \text{ s}^{-1}$ [40]) than the equivalent reaction with NH_3 (with a rate of $\sim 3 \times 10^{-11} \text{ cm}^3 \text{ s}^{-1}$ [33]) such that the NH_2 *production* might be suppressed. Another reaction that can play a role is a fast *gas phase loss* reaction of the produced NH_2 with SiH_4 or its dissociation products. Likely candidates for this reaction are the amino-silane creation reactions as proposed by Beach and Jasinski [19]. Finally, NH_2 radicals might be preferentially incorporated in the a- $\text{SiN}_x\text{:H}$ film leading to the low NH_2 density in the plasma. This argument is supported by values of the NH_2 surface loss probability as discussed in Sec. V.B.

B. NH_x radical densities versus SiH_4 flow

The N, NH and NH_2 radical densities as well as the NH_3 density were also measured for different SiH_4 flows, as shown in Fig. 3. The NH_3 flow was 17 sccs and

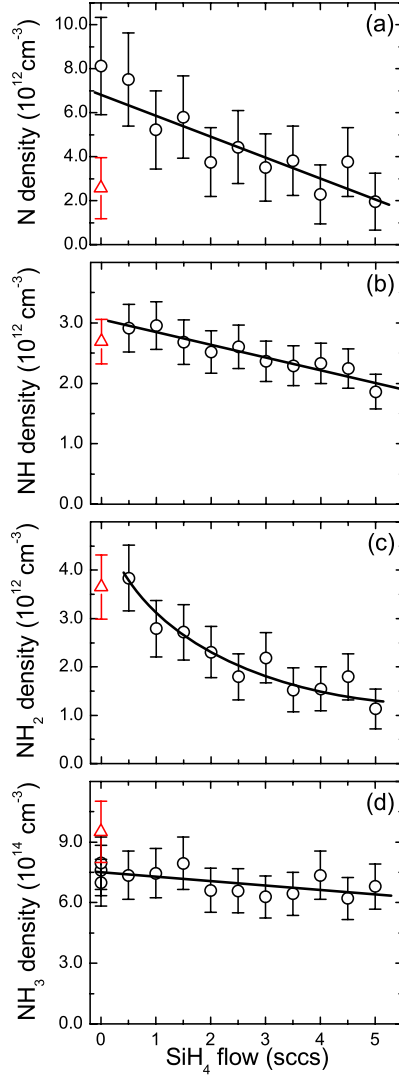


Figure 3: The N (a), NH (b) NH_2 (c) and NH_3 (d) densities as a function of the injected SiH_4 flow for an NH_3 flow of 17 sccs and an arc current of 45 A. The lines serve as a guide to the eye. The triangles are the measured values for an Ar- NH_3 plasma with clean stainless steel reactor walls.

the plasma source current 45 A. The densities of all NH_x radicals decrease significantly when silane is injected in the plasma. The N radical density decreases from $\sim 8.0 \times 10^{12} \text{ cm}^{-3}$ to $\sim 2.0 \times 10^{12} \text{ cm}^{-3}$ and the NH density from $\sim 3.0 \times 10^{12} \text{ cm}^{-3}$ to $\sim 2.0 \times 10^{12} \text{ cm}^{-3}$. The NH_2 density decreases from $\sim 4.0 \times 10^{12} \text{ cm}^{-3}$ to $\sim 1.0 \times 10^{12} \text{ cm}^{-3}$ for a SiH_4 flow of 5 sccs, while the NH_3 density decreases only slightly from $\sim 7.5 \times 10^{14}$

cm^{-3} to $\sim 6.5 \times 10^{14} \text{ cm}^{-3}$. Figure 3 also shows the values of the NH_x densities in the absence of SiH_4 for a clean stainless steel reactor (open triangles). Note that for small injected SiH_4 flows the N radical density in the depositing plasma is higher than in the situation without SiH_4 . This particular behavior will be addressed in more detail in Sec. V.B, but first the NH_x radical densities will be discussed in detail.

The small decrease of the NH density versus the SiH_4 flow can be explained by a decreased *production* rate due to the competition between the Ar^+ charge transfer reactions with NH_3 and SiH_4 , as explained in the previous section. The N and NH_2 densities, however, decrease faster than the NH density upon injection of SiH_4 , which suggests that an additional *loss* mechanism related to SiH_4 lowers the N and NH_2 density. A similar decreasing trend for the N radical density versus SiH_4 flow was observed by Kessels *et al.* in an $\text{Ar-N}_2\text{-H}_2\text{-SiH}_4$ plasma [16]. Due to the endoergic nature of the reaction of N radicals with SiH_4 (enthalpy = + 0.45 eV), the corresponding reaction rate is very low at room temperature ($< 8 \times 10^{-14} \text{ cm}^3 \text{ s}^{-1}$) [41]. At a gas temperature of 1750 K, we still expect the reaction rate to be very small due to the relatively high energy barrier for this reaction. Therefore, Kessels *et al.* argued that gas phase loss of N radicals can be excluded and it was established that a larger fraction of N radicals must be incorporated in the a-SiN_x:H film. Also for the $\text{Ar-NH}_3\text{-SiH}_4$ plasma N incorporation in the a-SiN_x:H film is most likely responsible for the observed N loss. For NH_2 , a gas phase loss mechanism involving SiH_4 molecules cannot be excluded on the basis of the reaction rates reported in the literature. Two possible reactions that might explain the observed NH_2 loss were already proposed in Sec. IV.A. The first reaction, which removes atomic H from the plasma by a reaction with SiH_4 suppressing the NH_2 production, can in principle take place. But on the basis of the small amount of injected SiH_4 molecules, it is unlikely that this reaction can explain the total NH_2 decrease. The second reaction resulting in the creation of amino-silanes is not expected to be significant as we found no evidence for these fragments by mass spectrometry. Moreover, a similar decrease of the NH and NH_2 density versus SiH_4 flow in a hotwire CVD system was attributed to a decreased decomposition efficiency of NH_3 on the hot wire surface [22] and not to gas phase reactions. In our case, the faster decrease of the NH_2 density is presumably caused by an increased incorporation of NH_2 into the a-SiN_x:H film at higher SiH_4 flows, similar to the situation for N radicals (Sec. V.B).

C. NH_x radical densities versus arc current.

Another important plasma parameter, besides the NH_3 and SiH_4 gas flows is the plasma source current, which determines the amount of ions emanating from the source. Figure 4 (a–d) show the NH_x (0–3) densities as a function of the arc current for a NH_3 flow of 17 sccs and a SiH_4 flow of 2.5 sccs. The N density increases linearly from

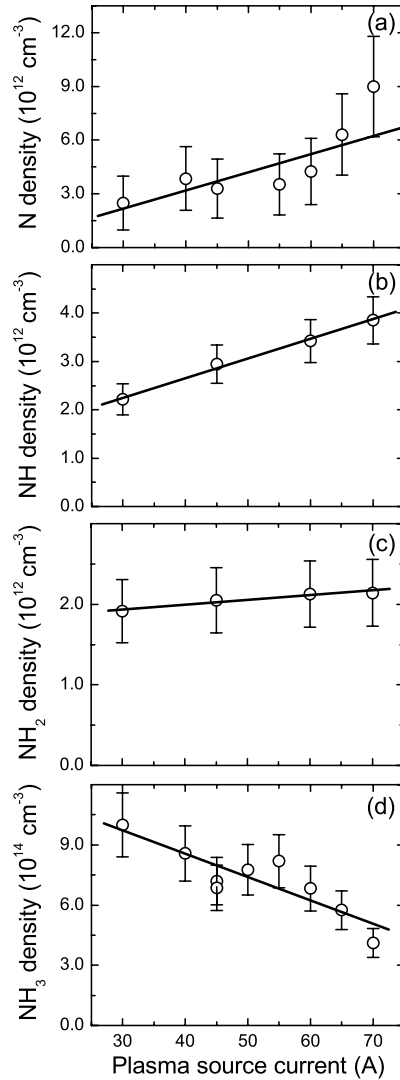


Figure 4: The N (a), NH (b), NH₂ (c) and NH₃ (d) densities as a function of the arc current for an NH₃ flow of 17 sccs and a SiH₄ flow 2.5 sccs. The lines serve as a guide to the eye.

$\sim 2.5 \times 10^{12} \text{ cm}^{-3}$ to $\sim 9.0 \times 10^{12} \text{ cm}^{-3}$ when the arc current is increased from 30 A to 70 A. Also the NH density increases linearly from $\sim 2.0 \times 10^{12} \text{ cm}^{-3}$ to $\sim 4.0 \times 10^{12} \text{ cm}^{-3}$, while the NH₂ density remains almost constant at $2.0 \times 10^{12} \text{ cm}^{-3}$. The NH₃ density in the plasma decreases from $\sim 10.0 \times 10^{14} \text{ cm}^{-3}$ to $\sim 4.0 \times 10^{14} \text{ cm}^{-3}$ when the arc current increases from 30 to 70 A.

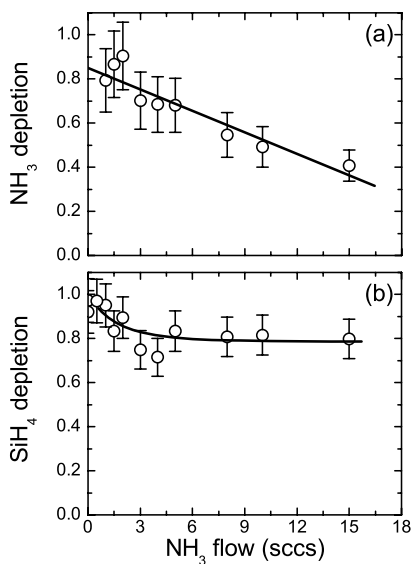


Figure 5: The depletion of NH₃ (a) and SiH₄ (b) in the Ar–NH₃–SiH₄ plasma versus the NH₃ flow for a SiH₄ flow of 2.5 sccs. The arc current was 45 A. The lines serve as a guide to the eye.

The linear increase of the N and NH density versus arc current confirms that the production mechanism of these radicals is dependent on Ar⁺ ions from the plasma source, as discussed briefly in Sec. II. The stronger increase of the N density compared to the NH density indicates that N radicals might also be produced in secondary reactions of Ar⁺ ions with NH_x radicals or N₂ molecules, while this is not the case for NH radicals. The linear decrease in the NH₃ density is expected because the NH₃ dissociation process starts with the charge transfer reaction of Ar⁺ with NH₃. Furthermore, the constant NH₂ density corroborates the previous conclusion that NH₂ is produced by a different pathway than N and NH radicals.

D. NH₃ and SiH₄ consumption

The relative amount of gas phase consumption of a precursor, also called depletion, can give valuable insights into the deposition process. Furthermore, an effective use of the precursor gas is important from a cost perspective (e.g. high depletion values allows for more efficient use of precursor gases). The amount of NH₃ and SiH₄ consumed in the plasma can be derived from mass spectrometry measurements of the NH₃ density and SiH₄ density (see Sec. III.C). In Fig. 5 we show the depletion of NH₃ (a) and of SiH₄ (b) in the plasma as a function of the NH₃ flow for a SiH₄ flow of 2.5 sccs. The depletion of NH₃ decreases from ~0.9 for small NH₃ flows to ~0.4 for high NH₃ flows. Accurate measurements of depletions near 100% for low

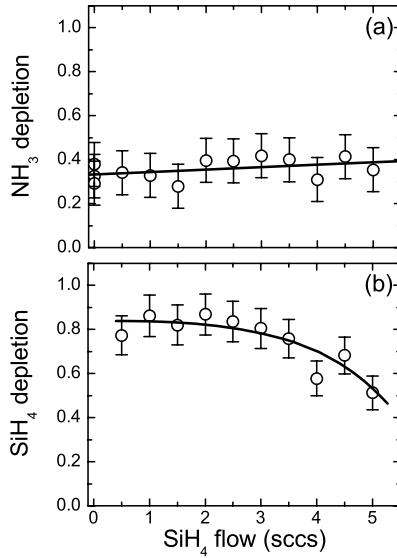


Figure 6: The depletion of NH₃ (a) and SiH₄ (b) in the Ar–NH₃–SiH₄ plasma versus the SiH₄ flow for a NH₃ flow of 17 sccs. The arc current was 45 A. The lines serve as a guide to the eye.

NH₃ flows are difficult, which explains the larger error bars in Fig. 5. The behavior of the NH₃ depletion versus NH₃ flow can be understood by considering the amount of reactive species from the source compared to the injected NH₃ flow and the remote character of the ETP technique [32]. For low NH₃ flows the amount of Ar⁺ from the plasma source is sufficient to dissociate all NH₃, but when the NH₃ flow is increased further, the amount of Ar⁺ will be deficient to dissociate all NH₃. At this point the depletion of NH₃ starts to decrease. Also the depletion of SiH₄ decreases from ~1.0 to ~0.8 when the NH₃ flow increases from 0 to ~6 sccs, whereas it remains constant at ~0.8 for higher NH₃ flows. The decrease of the SiH₄ depletion when the NH₃ flow increases is most probably related to a decrease in the direct dissociation of SiH₄ by Ar⁺ due to competition of this process with the charge exchange reaction of NH₃ with Ar⁺ as discussed in Sec. IV.A. At a NH₃ flow of 6 sccs, most Ar⁺ ions are used to dissociate NH₃, while SiH₄ is presumably dissociated indirectly by reactive NH_x species leading to a SiH₄ depletion of ~0.8.

Figures 6 (a) and (b) show the NH₃ and SiH₄ depletions versus the SiH₄ flow in an Ar–NH₃–SiH₄ plasma for a NH₃ flow of 17 sccs. The NH₃ depletion remains constant at ~0.4 over the whole range of SiH₄ flows, because the injected SiH₄ flow is relatively small compared to the NH₃ flow. Furthermore, the NH₃ flow is injected in an earlier stage of the plasma expansion than SiH₄ (see Fig. 1). Therefore, the NH₃ dissociation is not affected by the injected SiH₄ flow for these large NH₃ flows. The SiH₄ depletion

stays constant at ~0.8 for SiH₄ flows between 0 and 2.5 sccs SiH₄ and subsequently decreases to ~0.5 for a SiH₄ flow of 5 sccs. This suggests that the amount of reactive species created in the NH₃ dissociation process is the limiting factor for the SiH₄ dissociation for SiH₄ flows exceeding 2.5 sccs.

In the expanding thermal plasma, the NH₃ depletion is in the order of 40 % for actual deposition conditions of silicon nitride antireflection coatings on solar cells, while the SiH₄ depletion is approximately 80 %. Note that the consumed NH₃ flow is actually larger than the consumed SiH₄ flow leading to near stoichiometric silicon nitride. These values for the NH₃ and SiH₄ depletion are relatively high in comparison to the results reported by Umemoto *et al.* They reported a NH₃ depletion of 5% and a SiH₄ depletion of 60 % in the hotwire CVD process based on NH₃ and SiH₄. However, when H₂ is added to the NH₃/SiH₄ system, a much higher NH₃ decomposition efficiency can be achieved in the hotwire CVD process [42–44]. Chowdhury *et al.* reported SiH₄ depletions up to 100 % for small SiH₄ flows and high power density in their rf PECVD system based on N₂ and SiH₄ [45]. In the ETP plasma, both the NH₃ and the SiH₄ depletions increase when the arc current and therefore the plasma power is increased. For an injected SiH₄ flow of 2.5 sccs, NH₃ flow of 17 sccs and an arc current of 70 A, the NH₃ and SiH₄ depletions are ~60% and ~100 % respectively. These high values of the depletion enable high rate deposition of a-SiN_x:H using the ETP technique.

The typical depleted NH₃ density when the plasma is switched on is in the order of 10¹⁴ cm⁻³ while the typical NH_x densities generated are in the order of 10¹² cm⁻³ during actual deposition conditions. The difference in magnitude of these densities cannot be explained by N or H incorporation in the film alone, which means that other species besides NH_x radicals must be generated in the plasma. For an Ar–NH₃ plasma, it was already demonstrated that large densities of N₂ and H₂ molecules were generated [28]. Also in the Ar–NH₃–SiH₄ plasma we observed that most of the depleted NH₃ and SiH₄ flow is converted into H₂ and N₂ with typical densities in the order of 10¹⁴ cm⁻³ (not shown). A similar observation was also reported by Umemoto *et al.*, who measured the H₂ and N₂ production in their hotwire CVD system.

V. Discussion

A. Summary of the plasma chemistry

From the results presented in the current study combined with the outcome of previous studies, the following reaction pathway in the Ar–NH₃–SiH₄ plasma can be deduced. The cascaded arc plasma source produces primarily Ar⁺ ions that undergo a charge transfer reaction with NH₃ molecules injected in the very first part of the plasma expansion. The NH₃⁺ ions created recombine dissociatively into N and NH

radicals, while NH_2 radicals are produced via ion–molecule reactions or radical–molecule reactions with NH_3 molecules. This mechanism leads to relatively high N and NH densities that saturate at a level of $3.0\text{--}4.0 \times 10^{12} \text{ cm}^{-3}$ for high NH_3 flows due to the limited amount of Ar^+ available. The NH_2 density on the other hand increases linearly with the NH_3 flow and reaches a level of $2.5 \times 10^{12} \text{ cm}^{-3}$ for an NH_3 flow of 17 sccs.

When SiH_4 is injected in the plasma all NH_x radicals decrease in density. This decrease can be partly explained by a lower production rate due to the competition between the charge transfer reaction of Ar^+ with NH_3 and the charge transfer reaction of Ar^+ with SiH_4 . However, for the N and NH_2 radicals the decrease in density is more pronounced than for the NH radical suggesting that an additional loss mechanism is present for the N and NH_2 radicals, besides the reduction of their production rate. This loss mechanism is most likely an increased incorporation of these radicals in the a– $\text{SiN}_x\text{:H}$ film, as can be concluded from the surface loss of these radicals that will be discussed in Sec. V.B. In this case, the Si–N bond characteristic for a– $\text{SiN}_x\text{:H}$ is *not* predominantly formed in the plasma volume, but on the surface of the growing film. When the SiH_4 flow injected in the plasma is increased, the surface composition of the growing film changes due to a higher flux of impinging SiH_x radicals that create additional sites for N incorporation on the film’s surface. Therefore, the surface loss rate of N radicals will increase for higher SiH_4 flows.

The amount of reactive species emanating from the plasma source can be increased by a higher current, which leads to more production of N and NH radicals and a higher NH_3 consumption in the plasma. The higher flow of reactive NH_x species from the plasma source also allows for a higher degree of SiH_4 dissociation. For a plasma with a NH_3 flow of 17 sccs, a SiH_4 flow of 2.5 sccs and a plasma source current of 70 A, the dissociation degree of NH_3 and SiH_4 can be as high as 60% and 100% respectively. Finally, it was observed that significant amounts of N_2 and H_2 molecules are produced in the plasma from dissociated NH_3 and SiH_4 .

B. Surface loss probabilities

The kinetics of film growth in a plasma depend on the interactions of the plasma–generated species with the growing film surface. In order to understand how the film composition and electronic properties are related to the plasma parameters, detailed information on the interaction of the plasma species with the surface is required.

Information on the surface reactivity of species can be deduced from density measurements for different wall conditions. Figure 7 shows a measurement of the N radical density versus the NH_3 flow in an Ar– NH_3 plasma for a clean stainless steel wall and a wall covered with a silicon nitride film. The observed trends for both curves are identical, but the saturation value of the N radical density is substantially higher

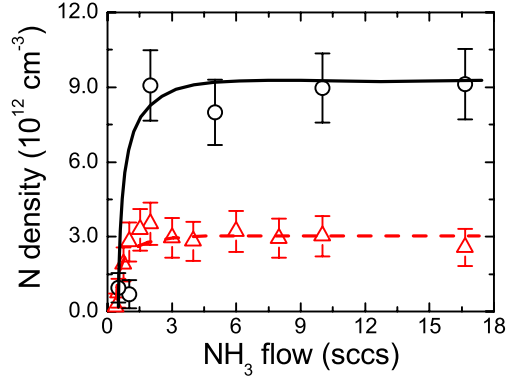


Figure 7: The N radical density versus the NH₃ flow measured in an Ar–NH₃ plasma by threshold ionization mass spectrometry for clean stainless steel reactor walls (triangles) and silicon nitride covered reactor walls (circles). The plasma settings were equal in both cases. The lines serve as a guide to the eye.

for the case of silicon nitride covered walls. For stainless steel walls the measured N density n_{SS} at high NH₃ flows is $\sim 3.0 \times 10^{12} \text{ cm}^{-3}$, while n_{SiN} is $\sim 9.0 \times 10^{12} \text{ cm}^{-3}$ for walls covered with silicon nitride. This difference in N density was already observed in Fig. 3 (a), where the N density for stainless steel walls (triangles) lies considerably lower than the N density in a depositing Ar–NH₃–SiH₄ plasma (circles). Assuming constant production rate (P) and no difference in gas phase loss for N radicals (corroborated by the extremely low reactivity of the N radical with SiH₄), the observed density difference must be caused by a changing surface loss rate [See Eq. (1)]. In general, species can be lost at the surface with a probability β , which consists of a “recombination part” with a probability γ and of a “growth part” with a probability s . According to Motz *et al.* [46] the flux of species that is lost at the surface is given by:

$$\Phi_{loss} = \frac{nv}{4} \frac{\beta}{1 - \frac{\beta}{2}}, \quad (2)$$

with $\beta = \gamma + s$, n the density of the species and v the thermal velocity. In a non-depositing NH₃ plasma, the sticking probability s is zero and the flux of species lost at the surface is determined by the recombination probability γ . For our experimental conditions with a partial N₂ pressure in the order of 10^{-2} mbar, the recombination probability on stainless steel γ_{SS} can be estimated at ~ 0.1 on the basis of the work of Adams and Miller [26] and Singh *et al.* [27]. Using this value of γ_{SS} and the experimentally observed density ratio n_{SiN}/n_{SS} of ~ 3.0 , we obtain a recombination probability of N radicals on a silicon nitride surface γ_{SiN} of ~ 0.03 via Eq. (2).

In SiH₄ containing plasmas the sticking probability s is non-zero as N radicals can also be incorporated in the growing a-SiN_x:H film. When we attribute the decrease in the N density as a function of the injected SiH₄ flow in Fig. 3 (a) solely to N incorporation in the a-SiN_x:H film, we can calculate an upper estimate for the sticking coefficient s , assuming a constant N recombination probability γ_{SiN} , no significant change in the N production rate due to SiH₄ addition and no gas phase loss. For example, the N density is $\sim 8.0 \times 10^{12} \text{ cm}^{-3}$ for a SiH₄ flow of 0 sccs, while it is $\sim 6.0 \times 10^{12} \text{ cm}^{-3}$ for a SiH₄ flow of 1 sccs. In the first situation the loss will only consist of N recombination on the surface ($s = 0$), while in the second case incorporation of N in the film causes an additional decrease in the N density. Using Eq. (2) we obtain a sticking coefficient s that varies with SiH₄ flow: from ~ 0.016 for 1 sccs injected SiH₄ to ~ 0.034 when the SiH₄ flow is 5 sccs. A similar change in the surface reaction probability $\beta = \gamma + s$ from ~ 0.007 for low SiH₄ flows to ~ 0.04 for higher SiH₄ flows was also observed by Kessels *et al.* in the Ar-N₂-H₂-SiH₄ expanding plasma [16, 17]. This change in the sticking probability s for higher SiH₄ flows, is most likely caused by a higher SiH_x flux to the surface creating more reactive surface sites available for N incorporation.

For NH and NH₂ radicals no significant difference in the surface recombination probability was observed on the basis of the measured densities in non-depositing plasmas for stainless steel walls and silicon nitride covered walls (see Figs. 3 (b) and (c)). The surface reactivity of NH and NH₂ on different materials was reported by Fisher and coworkers using laser induced fluorescence in combination with a molecular beam setup [23–25]. The molecular beam was created from a rf powered plasma based on a NH₃ or NH₃-SiH₄ feed gas mixture by expansion into a differentially pumped reactor. A surface loss probability $\beta_{NH} = 0.0 \pm 0.1$ for the NH radical on a-SiN_x:H surfaces in NH₃ and NH₃-SiH₄ plasmas was observed [23], indicating that the NH radical is virtually not reactive with the surface during plasma deposition of a-SiN_x:H ($s_{NH} = 0$). For the NH₂ radical, surface production ($\gamma_{NH2} < 0$) was found on a-SiN_x:H surfaces in a NH₃ plasma, while a surface loss probability β_{NH2} of 0.13 ± 0.07 was found in a NH₃-SiH₄ plasma [24]. This suggests that NH₂ is incorporated in the growing a-SiN_x:H film. Assuming a similar NH₂ recombination probability in NH₃ and NH₃-SiH₄ plasmas, we deduce a sticking coefficient for NH₂ (s_{NH2}) during a-SiN_x:H growth that is larger than 0.13.

C. Implications for a-SiN_x:H growth mechanism

The deposition of a-SiN_x:H films by plasmas is governed by reactive species (radicals) created in the plasma and their reaction kinetics on the surface (See Sec. V.B). More specifically, radical species are responsible for the creation of the Si-N network and two main options were introduced for the deposition mechanism of these

films. One mechanism was proposed by Smith *et al.* and is based on the creation of aminosilane radicals ($\text{Si}(\text{NH}_2)_3$) in the plasma phase [11], that are responsible for the a-SiN_x:H growth. On the other hand, Umemoto *et al.* [22] have demonstrated that NH₂ and SiH₃ radicals are the dominant growth precursors in the hotwire CVD deposition process of silicon nitride. These two mechanisms differ in the formation path of the characteristic Si–N bond, e.g. in the gas phase or on the surface of the growing film. In our analysis, we also found no evidence for the existence of amino–silanes in the ETP plasma by mass spectrometry, although the presence of the broadband absorption in the cavity ring–down measurements might indicate the presence of larger species. Umemoto suggested that the absence of amino silanes in the hotwire CVD process is caused by the relatively high atomic H fluxes that are created in the thermal decomposition of the injected precursors on the hot filament. In the expanding thermal plasma, the production of atomic H is also very efficient via the dissociative recombination reactions of NH_x⁺ ions with electrons (see Sec. IV.A). This could explain the absence of amino–silanes in the ETP plasma. Alternatively, Murley *et al.* provide another explanation for the absence of amino–silanes, which is related to the residence time of the gas in the reactor [20]. They showed that aminosilanes are primarily present for residence times higher than 2–3 s, which is larger than commonly used in the ETP plasma (typically ~0.5 s).

Based on our data of the Ar–NH₃–SiH₄ plasma, we conclude that the N incorporation in a-SiN_x:H film is most likely dominated by NH_x radicals, which implies that the Si atoms are brought to the surface via SiH_x radicals. This mechanism of Si incorporation by SiH_x radicals is also dominant in the Ar–N₂–H₂–SiH₄ plasma [16] and in the deposition of a-Si:H from Ar–H₂–SiH₄ plasmas. In the Ar–NH₃–SiH₄ plasma, we have also observed Si, SiH and SiH₃ radicals by TMS measurements. A preliminary study has shown that the densities of these radicals are all approximately $\sim 10^{11} \text{ cm}^{-3}$. From this perspective, it is expected that the role of N radicals in the Ar–NH₃–SiH₄ plasma is similar to their role in the silicon nitride growth mechanism from N₂–SiH₄ plasmas proposed by Smith *et al.* [14] and Kessels *et al.* [16, 17]. They showed that N radicals can insert into Si–Si backbonds of an a-Si:H-like layer that is created by impinging SiH_x radicals. NH radicals on the other hand are not reactive with the growing film, as can be deduced from the measured surface reaction probability, while NH₂ radicals are reactive on the surface with a reaction probability of ~0.13. This value is much higher than the reaction probability of N radicals (< 0.04), indicating a different sticking process on the surface of the growing film. NH₂ radicals might stick on dangling bonds on the surface or insert into (strained) Si–Si bonds. Furthermore, NH₂ could diffuse over the growing surface in a sort of hot precursor state, similar to the suggested mechanisms for SiH₃ in a-Si:H growth [47].

The actual contribution of the NH_x radicals to the silicon nitride growth depends on the measured densities and the surface reactivity of the radicals. These two parameters determine the N incorporation flux in the a-SiN_x:H film. To consider the feasibility of N incorporation by NH_x radicals, we estimate the N incorporation flux in two different ways. The first one is based on the deposition rate and the N atomic density determined from elastic recoil detection (ERD) measurements and in the second one we use the measured NH_x densities, the reported surface reaction probabilities and the estimated thermal velocity of the radicals in the plasma. For 1 sccs injected SiH₄, 17 sccs NH₃ and 45 A arc current, the N atomic density of the film was $\sim 3.8 \times 10^{22} \text{ cm}^{-3}$ and the deposition rate $\sim 6 \text{ nm/s}$, resulting in a N incorporation flux of $2.3 \times 10^{16} \text{ cm}^{-2} \text{ s}^{-1}$. For the calculation of the N incorporation flux from the radical densities on the other hand, we assume a sticking probability of ~ 0.02 for N radicals, ~ 0 for NH radicals and ~ 0.13 for NH₂ radicals based on the discussion in Sec. V.B. Now we can calculate the contribution of N, NH and NH₂ radicals to the growth assuming a thermal velocity of $\sim 1600 \text{ m/s}$ (corresponding to a gas temperature of 1750 K [33]), resulting in $4.9 \times 10^{15} \text{ cm}^{-2} \text{ s}^{-1}$, $0 \text{ cm}^{-2} \text{ s}^{-1}$, and $1.6 \times 10^{16} \text{ cm}^{-2} \text{ s}^{-1}$ for N, NH and NH₂ respectively. Taking into account the limited experimental accuracy in the sticking probability, the two incorporation fluxes $2.3 \times 10^{16} \text{ cm}^{-2} \text{ s}^{-1}$ and $2.1 \times 10^{16} \text{ cm}^{-2} \text{ s}^{-1}$ are in good agreement. Therefore, we conclude that the N incorporation in the a-SiN_x:H film can be explained by the NH_x ($x=0,2$) radical densities and their sticking probabilities. The NH₂ radical is the most important radical for N incorporation in the film (roughly 77%), followed by the N radical (roughly 23%). This result is similar to the growth mechanism based on SiH₃ and NH₂ radicals proposed by Umemoto *et al.* in a hotwire CVD process.

VI. Conclusions

The densities of N, NH and NH₂ radicals in the Ar-NH₃-SiH₄ expanding thermal plasma used for silicon nitride deposition were investigated. The radicals were measured as a function of several plasma parameters such as NH₃ flow, SiH₄ flow and arc current. For typical deposition conditions, we found densities of $\sim 5.0 \times 10^{12} \text{ cm}^{-3}$ for N radicals, $\sim 2.5 \times 10^{12} \text{ cm}^{-3}$ for NH radicals, and $\sim 2.0 \times 10^{12} \text{ cm}^{-3}$ for NH₂ radicals. In the SiH₄ containing plasma the densities of N, NH and NH₂ decrease with increasing SiH₄ flow, with the decrease being more prominent for N and NH₂. For NH, the decrease is most likely only due to a change in the gas phase production rate of the radicals, while N and NH₂ radicals decrease also in density as they are incorporated in the a-SiN_x:H film.

Besides the radical densities also the relative consumptions of NH₃ and SiH₄ in the plasma have been measured by mass spectrometry. For NH₃ we found relative

consumptions in the range of 90 % to 40 %, while the observed SiH₄ consumption lies between 90 % and 60 %. A large part of the consumed NH₃ is converted into H₂ and N₂ molecules, as was revealed by the large densities of these molecules (typically 10¹⁴ cm⁻³) in the plasma. Also the SiH₄ consumption contributes significantly to the observed H₂ density in the plasma.

Furthermore, we presented evidence that the recombination probability γ of N radicals is lower on a silicon nitride covered wall than on a stainless steel reactor wall. For NH and NH₂ such a difference in recombination probability was not observed. The sticking probability s for N radicals was also deduced from the measurements and varies with SiH₄ flow from ~0.01 to ~0.04. Comparison of the N growth flux calculated from the N atomic density in the film with the contributions from N and NH₂ radicals to the growth has led to the conclusion that these radicals can account for the observed N atomic density in the film. Therefore, we expect that Si atoms are delivered to the surface via SiH_x radicals creating an amorphous silicon like film that is nitrated by N and NH₂ radicals.

Acknowledgements

The authors thank M.J.F. van de Sande, J.F.C. Jansen, A.B.M. Hüsken, and H.M.M. de Jong for their skillful technical assistance. C.C.H. Lamers is gratefully acknowledged for her contribution to the measurements. This study has been supported by the Netherlands Foundation for Fundamental Research on Matter (FOM) and by the Netherlands Ministry of Economic Affairs, the Ministry of Education, Culture and Science and the Ministry of Public Housing, Physical Planning and Environment (E.E.T.–project “HR–CEL”). The research of W.K. has been made possible by a fellowship of the Royal Netherlands Academy of Arts and Sciences (KNAW).

References

- [1] J.C. Barbour, H.J. Stein, O.A. Popov, M. Yoder, C.A. Outten, *J. Vac. Sci. Technol. A* **9**, 480 (1991).
- [2] S. Garcia, I. Martil, G. Gonzalez, E. Castan, S. Duenas, M. Fernandez, *J. Appl. Phys.* **83**, 332 (1998).
- [3] J.M. Jeon and J-L. Lee, *Appl. Phys. Lett.* **86**, 172101 (2005).
- [4] D. Stryahilev, A. Sazonov, and A. Nathan, *J. Vac. Sci. Technol. A* **20**, 1087 (2002).
- [5] A.G. Aberle, *Sol. Energ. Mat. Sol. C* **65**, 239 (2001).
- [6] J. Hong, W.M.M. Kessels, W.J. Soppe, A.W. Weeber, W.M. Arnoldbik, and M.C.M. van de Sanden, *J. Vac. Sci. Technol. B* **21**, 2123 (2003).
- [7] N.I. Fainer, Yu.M. Rumyantsev, M.L. Kosinova, G.S. Yurjef, E.S. Maximovskii, and F.A. Kuznetsov, *Appl. Surf. Sci.* **113/114**, 614 (1997).
- [8] X-J. Liu, Y-F. Chen, H-L. Li, X-W. Sun, and L-P. Huang, *Thin Solid Films* **479**, 137 (2005).
- [9] R. Di Mundo, R. d'Agostino, F. Fracassi, F. Palumbo, *Plasma Process. Polym.* **2**, 612 (2005)
- [10] G. Lucovsky, P. D. Richard, D. V. Tsu, S. Y. Lin, and R. J. Markunas, *J. Vac. Sci. Technol. A* **4**, 681 (1986).
- [11] D.L. Smith, A.S. Alimonda, C-C. Chen, S.E. Ready, and B. Wacker, *J. Electrochem. Soc.* **137**, 614 (1990).
- [12] S. Sitbon, M. C. Hugon, B. Agius, F. Abel, J. L. Courant, and M. Puech, *J. Vac. Sci. Technol. A* **13**, 2900 (1995).
- [13] D. Landheer, N. G. Skinner, T. E. Jackmann, D. A. Thompson, J. G. Simmons, D. V. Stevanovic, and D. Khatamian, *J. Vac. Sci. Technol. A* **9**, 2594 (1991).
- [14] D.L. Smith, A.S. Alimonda, and F.J. von Preissig, *J. Vac. Sci. Technol. B* **8**, 551 (1990).
- [15] B.F. Hanyaloglu, and E.S. Aydil, *J. Vac. Sci. Technol. A* **16**, 2794 (1998).
- [16] W. M. M. Kessels, F. J. H. van Assche, J. Hong, D. C. Schram, and M. C. M. van de Sanden, *J. Vac. Sci. Technol. A* **22**, 96 (2004).
- [17] W.M.M. Kessels, F.J.H. van Assche, P.J. van den Oever, and M.C.M. van de Sanden, *J. Non-Cryst. Solids* **338**, 37 (2004).
- [18] D.L. Smith, *J. Vac. Sci. Technol. A* **11**, 1843 (1993).
- [19] D.B. Beach and J.M. Jasinski, *J. Phys. Chem.* **94**, 3019 (1990).
- [20] D.T. Murley, R.A.G. Gibson, B. Dunnett, A. Goodyear, and I.D. French, *J. Non-Cryst. Solids* **187**, 324 (1995).
- [21] J.A. Theil, S.V. Hattangady, and G. Lucovsky, *J. Vac. Sci. Technol. A* **10**, 719 (1992).

- [22] H. Umemoto, T. Morimoto, M. Yamawaki, Y. Masuda, A. Masuda, and H. Matsumura, *Thin Solid Films* **430**, 24 (2003).
- [23] E.R. Fisher, P. Ho. W.G. Breiland, and R.J. Buss, *J. Phys. Chem.* **96**, 9855 (1992).
- [24] P.R. McCurdy, C.I. Butoi, K.L. Williams, and E.R. Fisher, *J. Phys. Chem. B* **103**, 6919 (1999).
- [25] M.L. Steen, K.R. Kull, and E.R. Fisher, *J. Appl. Phys.* **92**, 55 (2002).
- [26] S.F. Adams, and T.A. Miller, *Plasma Sources Sci. Technol.* **9**, 248 (2000).
- [27] H. Singh, J.W. Coburn, and D.B. Graves, *J. Appl. Phys.* **88**, 3748 (2000).
- [28] P.J. van den Oever, J.L. van Hemmen, J.H. van Helden, D.C. Schram, R. Engeln, M.C.M. van de Sanden, and W.M.M. Kessels, *Plasma Sources Sci. Technol.* **15**, 546 (2006); Chapter 3.
- [29] B. Hoex, A. J. M. van Erven, R. C. M. Bosch, W. T. M. Stals, M. D. Bijker, P. J. van den Oever, W. M. M. Kessels, and M. C. M. van de Sanden, *Progress in Photovoltaics* **13**, 705 (2005).
- [30] M. Schaepekens, T.W. Kim, A.G. Erlat, M. Tan, K.W. Flanagan, C.M. Heller, and P.A. McConnelee, *J. Vac. Sci. Technol. A* **22**, 1716 (2004).
- [31] W.M.M. Kessels, C.M. Leewis, M.C.M. van de Sanden, and D.C. Schram, *J. Appl. Phys.* **86**, 4029 (1999).
- [32] M.C.M. van de Sanden, R.J. Severens, W.M.M. Kessels, R.F.G. Meulenbroeks, and D.C. Schram, *J. Appl. Phys.* **84**, 2426 (1998); *J. Appl. Phys.* **85**, 1243 (1999).
- [33] P.J. van den Oever, J.H. van Helden, C.C.H. Lamers, R. Engeln, D.C. Schram, M.C.M. van de Sanden, and W.M.M. Kessels, *J. Appl. Phys.* **98**, 093301 (2005); Chapter 2.
- [34] J.P.M. Hoefnagels, Y. Barrell, W.M.M. Kessels, and M.C.M. van de Sanden, *J. Appl. Phys.* **96**, 4094 (2004).
- [35] W.M.M. Kessels, A. Leroux, M.G.H. Boogaarts, J.P.M. Hoefnagels, M.C.M. van de Sanden, and D. C. Schram, *J. Vac. Sci. Technol. A* **19**, 467 (2001).
- [36] S. Agarwal, G.W.W. Quax, M.C.M. van de Sanden, D. Maroudas, and E.S. Aydil, *J. Vac. Sci. Technol. A* **22**, 71 (2004).
- [37] J. Benedikt, S. Agarwal, D. Eijkman, W. Vandamme, M. Creatore and M.C.M. van de Sanden, *J. Vac. Sci. Technol. A* **23**, 1400 (2005).
- [38] Kim Y –K and Desclaux J P 2002 *Phys. Rev. A* **66** 012708
- [39] H.M. Rosenstock, K. Draxl, B.W. Steiner and J.T. Herron, *Energetics of Gaseous Ions*, Journal of Physical and Chemical Reference Data Vol 6, Supplement No. 1 (American Institute of Physics, Inc, New York, 1977).
- [40] A. Goumri, W.-J. Yuan, L. Ding, Y. Shi, and P. Marshall, *Chem. Phys.* **177**, 233 (1993).
- [41] L.G. Piper and G.E. Caledonia, *J. Phys. Chem* **95**, 698 (1991).

- [42] A.H. Mahan, A.C. Dillon, L.M. Gedvilas, D.L. Williamson, and J.D. Perkins, *J. Appl. Phys.* **94**, 2360 (2003).
- [43] Q. Wang, S. Ward, L. Gedvilas, B. Keyes, E. Sanchez, and S. Wang, *Appl. Phys. Lett.* **84**, 338 (2004).
- [44] S.G. Ansari, H. Umemoto, T. Morimoto, K. Yoneyama, A. Izumi, A. Masuda, and H. Matsumura, *Thin Solid Films* **501**, 31 (2006).
- [45] A.I. Chowdhury, T.M. Klein, T.M. Anderson, and G.N. Parsons, *J. Vac. Sci. Technol. A* **16**, 1852 (1998).
- [46] H. Motz, and H. Wise, *J. Chem. Phys.* **32**, 1893 (1960).
- [47] G. Ganguly, and A. Matsuda, *Phys. Rev. B* **47**, 3661 (1993).

PART II

Chapter 5

Real time spectroscopic ellipsometry on ultrathin ($<50 \text{ \AA}$) hydrogenated amorphous silicon films^{*}

Real time spectroscopic ellipsometry was used to determine the time–evolution of the dielectric function, bulk thickness and surface roughness during hot–wire chemical vapor deposition of hydrogenated amorphous silicon (a–Si:H). The amorphous silicon films were deposited on native–oxide covered c–Si (100) and GaAs (100) substrates at temperatures in the range from 70 to 350 °C. Data analysis by a three layer optical model, consisting of substrate, bulk and surface roughness layer, revealed that the dielectric function of the a–Si:H film changes in the initial growth regime ($d < 50 \text{ \AA}$), which can be attributed to a higher optical bandgap for films with a smaller thickness. It is argued that the origin of this higher bandgap lies most likely in quantum confinement effects of the electron wavefunction in the ultrathin film, with possibly a small contribution of a higher hydrogen content in the ultrathin film. In addition, we show that the trends in surface roughness and bulk thickness are only marginally affected, regardless of whether the change in dielectric function with film thickness is incorporated in the data analysis.

^{*} Submitted for publication: P.J. van den Oever, M.C.M. van de Sanden, and W.M.M. Kessels

I. Introduction

In recent years there has been a continuous trend towards the application of thinner films deposited on wafer substrates, which is primarily caused by the advancement of the semiconductor industry [1]. Another example can be found in the solar cell industry. Ultrathin films (thickness $< 50 \text{ \AA}$) of hydrogenated amorphous silicon (a-Si:H) are for example applied as a surface passivation layer, emitter of charge carriers, and back surface contact in silicon heterojunction (SHJ) solar cells [2,3]. For virtually all applications, the quality of the interface between the ultrathin film and the underlying substrate created in the first stages of growth is paramount [4,5]. Valuable information about the processes governing the interface formation can be extracted from the time-evolution of film properties – such as surface roughness, bulk thickness, and dielectric function ϵ – in the early stages of deposition. For a-Si:H, for instance, the dielectric function reflects the main absorption in the film due to band-to-band transitions, while the evolution of the surface roughness yields information about nucleation processes and surface roughening or smoothing mechanisms [6,7]. Furthermore, it is believed that the hydrogen content in the a-Si:H film plays an important role in the initial stages of growth until a thickness of approximately 35 \AA [8,9]. For such thin films, *in situ* and real time measurement of material properties requires very sensitive diagnostics, because of the limited thickness of the films and the dynamic nature of the initial growth regime.

Ultrathin a-Si:H films have been investigated both structurally and compositionally by a variety of techniques such as high-resolution transmission electron microscopy [5,10] and secondary ion mass spectrometry [10,11]. Although very powerful, these techniques are not applicable in real time measurements, are sample-destructive, and do not provide fast process feedback. Alternatively, real time spectroscopic ellipsometry (RTSE) has demonstrated its sensitivity to sub-nanometer changes in thickness and can be applied in real time providing instantaneous process feedback [12,13]. However, in most cases the interpretation of the RTSE data is challenging as the analysis is based on a multilayer model that requires assumptions about the film structure and dielectric function of each consecutive layer. Within these assumptions the RTSE data analysis gives the evolution of the bulk thickness and surface roughness during film growth, which also yields information about the initial growth regime [6,7,14].

The dielectric functions of thick a-Si:H films can be determined directly from RTSE data by an elaborate procedure using a global regression analysis, when they are constant over a relatively large thickness range. This procedure determines the shape of the dielectric function and yields accurate results for the bulk thickness and surface roughness evolution. Nevertheless, parameterizations that assume a

prescribed shape of the dielectric function are often preferred, because they are relatively uncomplicated, are defined in physically useful parameters, can be applied on a single, ex-situ measurement and allow for a controlled variation of the dielectric function. In contrast to thick films ($d \gg 50\text{\AA}$), many authors have reported that the dielectric function of ultrathin a-Si:H films changes significantly with thickness [15–20]. However, in most RTSE analysis methods such a change in dielectric function is not incorporated, although it might impact the information extracted about the first stages of a-Si:H growth.

Here we investigate the thickness dependence of the dielectric function and the evolution of the bulk and surface layer thickness in the first stages of growth by RTSE. The RTSE data analysis procedure for ultrathin a-Si:H films is improved compared to the well established procedure for thick films [6,14]. In Sec. II of this Chapter we present the experimental arrangement and in Sec. III the RTSE data analysis is described in detail. The optical model is discussed and a method to extract the dielectric function directly from the ellipsometric data is presented. The commonly used Cody–Lorentz and Tauc–Lorentz parameterizations [21] are discussed and compared in Sec. III.C on the basis of the fit quality for six RTSE data sets of a-Si:H growth under different conditions. Subsequently, we focus on the data analysis for ultrathin films and show that the quality of the fit can be drastically improved by allowing a controlled change in the dielectric function via a parameterization for films thinner than 50 Å. In Sec. IV.C, we consider and discuss possible origins for the observed changes in dielectric function, such as a high hydrogen content in the interface layer or quantum confinement effects of the electron wavefunction. Finally, we discuss the impact of the improved RTSE data analysis on the deduced bulk thickness and roughness evolution in comparison with the analysis when using a thickness independent dielectric function for the initial stage of growth. (Sec. IV.D).

II. Experimental procedures

The a-Si:H films were deposited in an ultrahigh vacuum (UHV) setup consisting of two independently pumped stainless steel chambers separated by a central flange with the substrate mount. The setup features a low contaminant background, accurate substrate temperature control and excellent optical access to the substrate for diagnostics such as spectroscopic ellipsometry (SE) [14], infrared absorption spectroscopy in the attenuated total reflection geometry (ATR) [22], and second-harmonic generation [23]. More details on the experimental setup can be found in Ref. 14. Although SE and ATR were used simultaneously to monitor the deposition process of a-Si:H films by hot wire chemical vapor deposition (HWCVD), we focus on the SE measurements in this study.

Due to a possible substrate material dependency, both Si(100) and GaAs(100) substrates (50x20 mm²) with surface native oxide were used. In addition, GaAs substrates have a high infrared transmission at elevated substrate temperatures, which was required for the ATR measurements. The substrates were cleaned ultrasonically in ethanol for 20 minutes and subsequently blown dry with nitrogen. The GaAs substrates could be re-used by removing the silicon remnants from previous depositions by a wet chemical etch in a 0.1 M/l KOH solution for ~30 min prior to the cleaning procedure. After mounting the substrate and pumping down, the setup and the substrate were heated to 70 °C and 150 °C respectively and left over night to reach a base pressure below 2×10^{-8} mbar.

Before the actual deposition by hot-wire chemical vapor deposition (HWCVD) in undiluted SiH₄, the substrate was cooled down or heated to the desired temperature. A SiH₄ flow of 3 standard cm³/min (Praxair, purity > 99.995% and with additional purification) resulted in a deposition pressure of $\sim 8 \times 10^{-3}$ mbar. The SiH₄ was decomposed by a coiled tungsten filament (0.4 mm diameter), which was located approximately 11 cm from the substrate. This filament was resistively heated to a temperature of $\sim 2000 \pm 200$ °C by a DC current of 9.5 A, while before deposition the substrate was protected from direct exposure to generated radical species by an automated shutter located directly in front of the substrate. The used pressure and filament-substrate distance correspond to optimal conditions for hot-wire a-Si:H deposition as reported by Molenbroek *et al.* [14,24]. In this study, films were deposited on GaAs at substrate temperatures of 70, 150, 250, and 350 °C, while for the depositions on c-Si only temperatures of 150 and 250 °C were used. For all these conditions the deposition rate was approximately 30 Å/min. Table 1 summarizes the most important deposition conditions as well as the bandgap determined by the Tauc procedure [25] and the refractive index at 2 eV for the six depositions discussed in this Chapter. Although the study is focused on ultrathin films ($d < 50$ Å), the depositions were continued to a film thickness of ~ 1500 Å to accurately determine the bulk material properties.

The spectroscopic ellipsometry measurements were carried out using a rotating compensator spectroscopic ellipsometer (J.A. Woollam M-2000U), collecting 476 wavelengths in a spectral range from 1.24 to 5.0 eV. The ellipsometry light beam entered and exited the vacuum chamber via strain-free windows (Bomco Inc.) and the angle of incidence was approximately 59 degrees. RTSE measurements were taken in real time before, during and after the film deposition. Averaging 25 spectra, the time resolution of the RTSE measurements was ~ 3.5 seconds, giving an excellent signal-to-noise ratio.

Table 1: An overview of the a-Si:H samples used in this study. The Cody-Lorentz parameters, Tauc bandgap (E_{Tauc}) and refractive index at 2 eV (n_{2eV}) are given for a-Si:H grown on c-Si and GaAs substrates with native oxide at a deposition temperature of 70, 150, 250 and 350°C. Also the MSE between fit and data, averaged over all consecutive time slices, is given for Cody-Lorentz and Tauc-Lorentz parameterizations of the dielectric function. In the first data column the typical errors in the parameters are given.

Sample number	1	2	3	4	5	6
Substrate material	Si(100)	Si(100)	GaAs(100)	GaAs(100)	GaAs(100)	GaAs(100)
T_{sub} (°C)	150 ± 20	250	70	150	250	350
E_{Tauc} (eV)	1.75 ± 0.03	1.72	1.81	1.81	1.72	1.64
n_{2eV}	4.22 ± 0.02	4.45	3.78	4.14	4.43	4.61
$\epsilon_1(\infty)$	1.39 ± 0.05	1.02	1.43	1.39	1.32	1.29
A	79 ± 2	92	85	81	77	77
Γ	2.40 ± 0.01	2.43	2.56	2.37	2.32	2.35
E_0 (eV)	3.74 ± 0.01	3.69	3.75	3.75	3.67	3.62
E_g (eV)	1.59 ± 0.02	1.52	1.63	1.67	1.55	1.43
E_p (eV)	1.17 ± 0.05	1.33	1.70	1.25	1.02	0.98
Av. MSE CL	3.28	1.74	2.24	1.44	2.64	2.25
Av. MSE TL	3.78	2.91	3.19	2.91	3.74	4.17

III. RTSE data analysis

A. General information

In this section, we introduce the data analysis procedures needed to extract useful information from the SE measurements. Spectroscopic ellipsometry measures the change in polarization state of light upon reflection off a sample in terms of the ellipsometric angles Ψ and Δ , that can also be expressed in the *pseudo* dielectric function of the sample ($\langle \epsilon \rangle = \langle \epsilon_1 \rangle + i \langle \epsilon_2 \rangle$). To extract physical quantities of interest such as the dielectric function, bulk thickness and surface roughness from the pseudo dielectric function, a multilayer optical model is needed. Throughout this Chapter we use a relatively simple three-layer optical model, consisting of substrate, film, and surface roughness layer for the RTSE data analysis. The dielectric function ($\epsilon = \epsilon_1 + i\epsilon_2$) of the substrate can easily be extracted from the measurements before deposition, but the extraction of the dielectric function of the film from the RTSE data after deposition is more complex. The film's dielectric function can be determined directly without assumptions about its spectral shape by a global regression analysis (method 1), or it can be determined indirectly by using a parameterization that

prescribes a specific shape of the dielectric function versus photon energy (method 2). Method 2 is often preferred as it is relatively uncomplicated, provides direct access to physically useful parameters and can be applied to a single ex-situ measurement at the final thickness, which is not the case for method 1. Section III.B discusses both methods to determine the dielectric function in detail. After the dielectric function of the film has been determined (either method 1 or 2), the bulk thickness and surface roughness layer thickness can be extracted from the RTSE data. At all points in time, a realistic optical model should provide an accurate description of the measured Ψ and Δ values while maintaining the lowest level of complexity (number of fitting parameters) possible.

In our case, all RTSE data were analyzed with the EASE 2.30 software package provided by J.A. Woollam Co., Inc. [26] using the three layer model with bulk film thickness (d_b) and surface roughness layer thickness (d_s) as free parameters. The total film thickness is defined as $d_t = d_b + (1-f_v) \times d_s$, in which f_v is the void fraction in the surface roughness layer (see Sec. III.B). The model was fit to each spectrum minimizing the mean square error (MSE) between fit and data. The MSE is defined as:

$$\text{MSE} = \sqrt{\frac{1}{2N-M} \sum_{i=1}^N \left[\left(\langle \varepsilon_1 \rangle_i^{\text{exp}} - \langle \varepsilon_1 \rangle_i^{\text{mod}} \right)^2 + \left(\langle \varepsilon_2 \rangle_i^{\text{exp}} - \langle \varepsilon_2 \rangle_i^{\text{mod}} \right)^2 \right]}. \quad (1).$$

In this expression, N is the number of measured wavelengths, M the number of fit variables in the model and $\langle \varepsilon_1 \rangle_i^{\text{exp}}$, $\langle \varepsilon_1 \rangle_i^{\text{mod}}$, $\langle \varepsilon_2 \rangle_i^{\text{exp}}$, and $\langle \varepsilon_2 \rangle_i^{\text{mod}}$ are the real and imaginary parts of the experimental or modeled pseudo dielectric functions at wavelength i calculated directly from the experimental or modeled ellipsometric angles Ψ and Δ . In the fit procedure, the final fit parameters at one point in time provide the starting values for fitting the next time point.

B. The optical model

Substrate dielectric function

The substrate dielectric function used in the model was extracted from the RTSE measurements before deposition by direct numerical inversion [27] and is in good agreement with the tabulated values for GaAs or c-Si plus native oxide. The use of this so-called “pseudo-substrate” method is justified by the relatively small native oxide thickness (~ 20 Å) compared to the probing wavelength ($\gg 2450$ Å), which precludes interference effects in these layers. Furthermore, we assume no substrate modification during deposition, which is a reasonable assumption because of the remote nature of the HWCVD technique used in this study.

Film dielectric function

The dielectric function of the a-Si:H film was determined directly from the RTSE data in a procedure based on the three layer substrate–film–roughness model by a global regression analysis using at least six RTSE spectra, equally distributed in time over the part of the deposition in which the material properties can be assumed constant (i.e., excluding the initial regime of film growth, $d \ll 50 \text{ \AA}$). This procedure (method 1) determines the dielectric function in a Kramers–Kronig consistent way without a priori assumptions about the shape of the dielectric function (no parameterization), the bulk thickness, and the surface roughness layer thickness. It minimizes the MSE by fitting the shape of the dielectric function, the bulk thickness and surface roughness layer thickness for all selected time slices simultaneously. In this procedure, the surface roughness is represented by a Bruggeman effective medium approach, which will be discussed below. This relatively fast analysis, which uses tabulated values for the a-Si:H dielectric function as an initial guess, yields a dielectric function that corresponds to the minimum in the MSE and is in good agreement with results obtained by the more elaborate global dynamic minimization scheme described by Collins *et al.* [28]. The dielectric function resulting from the abovementioned procedure can be used directly to extract the bulk thickness and the surface roughness layer thickness from the RTSE data.

In some cases a parameterization of the dielectric function (i.e., method 2) is preferable as discussed previously. Suitable parameterizations for the a-Si:H dielectric function are the Kramers–Kronig consistent Tauc–Lorentz (TL) or Cody–Lorentz (CL) model, which are both based on the assumption of parabolic bands but either with a constant momentum matrix element (TL) or a constant dipole matrix element (CL) [21]. For both parameterizations, the imaginary part of the dielectric function can be written as^{*}:

$$\varepsilon_2(E) = \begin{cases} 0 & 0 < E \leq E_g \\ G(E) \frac{AE_0\Gamma E}{[(E^2 - E_0^2) + \Gamma^2 E^2]} & E > E_g \end{cases}, \quad (2)$$

with A the amplitude, E_0 the peak transition energy, Γ the broadening term and E_g the bandgap energy. $G(E)$ defines the near bandgap behavior, which is different for respectively the TL (G_{TL}) and CL (G_{CL}) model:

^{*} In contrast to the original description of the Cody-Lorentz model by Ferlauto and coworkers, here the exponential Urbach tail due to localized states below the bandgap is not included, mainly because of the limited sensitivity to low absorption values and the small spectral range below the bandgap.

$$G_{TL}(E) = \frac{(E - E_g)^2}{E^2} \quad (3)$$

$$G_{CL}(E) = \frac{(E - E_g)^2}{(E - E_g)^2 + E_p^2} . \quad (4)$$

In the CL expression, E_p is a transition energy that separates the Cody shaped absorption onset from the Lorentzian behavior. The real part of the dielectric function $\varepsilon_1(E)$ is in both cases obtained by Kramers–Kronig integration of $\varepsilon_2(E)$, given by:

$$\varepsilon_1(E) = \varepsilon_1(\infty) + \frac{2}{\pi} P \int_{E_g}^{\infty} \frac{\xi \varepsilon_2(\xi)}{\xi^2 - E^2} d\xi , \quad (5)$$

where $\varepsilon_1(\infty)$ is a fitting constant that allows $\varepsilon_1(E)$ to converge to values different from unity, and P stands for the Cauchy principal part of the integral.

In previous studies, we also used the Tauc–Lorentz parameterization directly (method 2) to determine the dielectric function of hot–wire deposited a–Si:H [14], which is justified when the parameterization is a good representation of the film's dielectric function. However, when this is not the case or when the dielectric function of the deposited film is unknown, a parameterization can not be used and the dielectric function needs to be determined directly from the RTSE data (for example using method 1). This dielectric function obtained can subsequently be used to fit the consecutive RTSE spectra in time as well as to develop an adequate parameterization for the dielectric function of the deposited film. In the next section, we will determine which parameterization is best suited to describe the dielectric function of a–Si:H deposited at various substrate temperatures on Si(100) and GaAs(100) substrates covered with native oxide.

Surface roughness

The dielectric function of the surface roughness layer (ε_s) was modeled using a Bruggeman effective medium approximation, which is assumed to consist of voids with a fraction f_v and of the underlying film with a fraction $f_f = 1 - f_v$:

$$0 = (1 - f_v) \frac{\varepsilon_f - \varepsilon_s}{(\varepsilon_f + 2\varepsilon_s)} + f_v \frac{\varepsilon_v - \varepsilon_s}{(\varepsilon_v + 2\varepsilon_s)} . \quad (6)$$

In this expression ε_f and ε_v represent the dielectric function of the film and voids ($\varepsilon_1 = 1$ and $\varepsilon_2 = 0$ for all photon energies), respectively. The Bruggeman effective medium approximation is commonly used to model the surface roughness layer in ellipsometry data analysis and its validity was evaluated in detail by Fujiwara and coauthors [29]. They found that a void fraction f_v of 0.5 gives an excellent representation of the surface roughness layer for bulk a–Si:H growth. In a similar analysis carried out on our RTSE data, we came to the same conclusion. Therefore, we

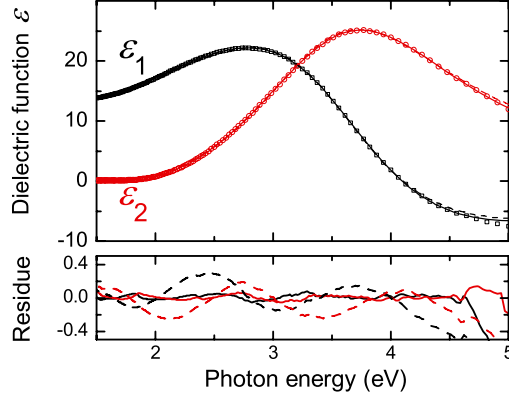


Figure 1: The real and imaginary part of the dielectric function (ϵ_1 and ϵ_2) of an a-Si:H film deposited at 150 °C on a GaAs substrate determined by a global regression analysis using 12 time slices of RTSE data. The parameterizations of the dielectric function using the Tauc-Lorentz (dashed line) and Cody-Lorentz (solid line) model are also shown, as well as the corresponding residue values.

use a void fraction of 0.5 in the Bruggeman effective medium approximation of the surface roughness layer in this study. Although the surface roughness determined by SE is not sensitive to the shape of the surface morphology, a comparison between atomic force microscopy (AFM) and SE has led to the conclusion that the roughness of a-Si:H films determined by SE is midway between the peak-to-peak and root-mean-square roughness determined by AFM [29].

C. The choice between Tauc-Lorentz or Cody-Lorentz parameterization

In this section we evaluate which parameterization is best suited to describe the dielectric function of a-Si:H using actual RTSE data from depositions. Figure 1 shows the dielectric function of the a-Si:H film deposited at 150 °C on a GaAs substrate determined directly from the RTSE data using method 1 as described above. Furthermore, the figure shows the best fits to this dielectric function using the CL and TL parameterizations. As can be seen from the residue values between data and fit depicted in the lower part of Fig. 1, the fit using the CL parameterization is significantly better. Only for photon energies above 4.5 eV a small deviation between parameterization and the directly determined dielectric function is observed. For the depositions at other substrate temperatures and types we also found that the CL parameterization was better than the TL parameterization.

Table 1 shows the CL parameters $\epsilon(\infty)$, A , E_0 , Γ , E_g and E_p extracted from the fits for the six a-Si:H depositions considered in this study. These CL as well as the TL parameterizations determined by fitting the directly extracted dielectric function were

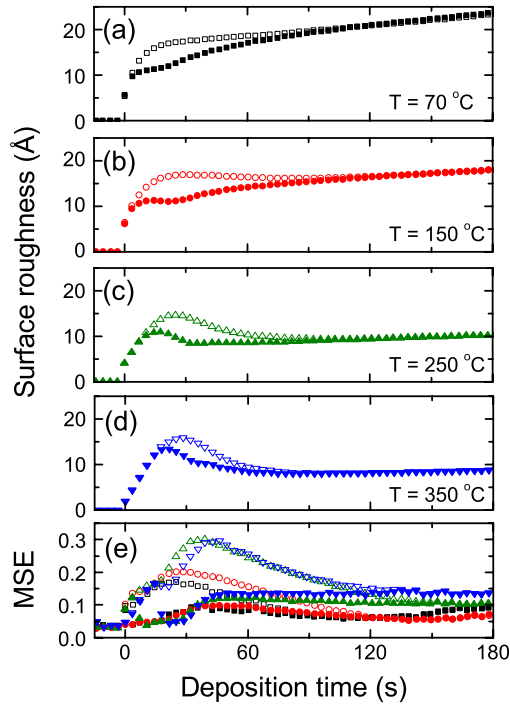


Figure 2: The surface roughness evolution in the first 180 seconds ($\sim 90 \text{ \AA}$) extracted from the RTSE data using the analysis with fixed (open symbols) and variable bandgap (solid symbols) for films deposited on GaAs substrates at a substrate temperatures of (a) 70°C , (b) 150°C , (c) 250°C and (d) 350°C . (e) The mean square error (MSE) associated with the fits. In (e) the symbol types correspond to those in (a)-(d).

subsequently used to extract the time–evolution of the bulk thickness and surface roughness layer thickness from the consecutive RTSE spectra. The time–averaged MSE values associated to these fits are also given in Table 1. Comparing the averaged MSE obtained using the CL and the TL parameterizations confirms the conclusion that the CL model is a better representation of the a–Si:H dielectric function for films deposited on both c–Si and GaAs substrates at evaluated temperatures. The superiority of the CL over the TL parameterization is supported by various other studies [21,30] and therefore, in all subsequent analysis the Cody–Lorentz parameterization will be used.

IV. RTSE data analysis for ultrathin films

A. RTSE data analysis with a thickness independent dielectric function

The use of a thickness independent dielectric function of the bulk layer has become a standard procedure in analyzing RTSE data of thin film deposition processes [6,14]. Here we apply the data analysis procedure described in the previous section under the assumption of a thickness independent dielectric function to our data and focus on the early stages of growth. The bulk dielectric function was extracted directly from the RTSE data (method 1) and subsequently parameterized by the Cody–Lorentz model, which was used to fit the consecutive RTSE spectra for bulk thickness and surface roughness. Figure 2 shows the fit results using the three layer model (as described in Sec. III) in the first 180 seconds of a–Si:H deposition on GaAs substrates at various temperatures. For brevity, we only show the temperature series on GaAs substrates in this section, but the depositions on c–Si show a similar behavior with slightly lower absolute values of the surface roughness. As expected, the bulk layer thickness (not shown) increases linearly as a function of the deposition time for all substrate temperatures and the total film thickness after 180 s deposition is approximately 90 Å for all films. In the first 20 seconds of the deposition, the surface roughness d_s increases very fast for all temperatures to a level of approximately 15 Å as can be seen in Figs. 2 (a–d). Thereafter, the surface roughness evolution behaves differently for the various temperatures. For the deposition at 70 °C the roughness increases monotonically to ~24 Å, while the depositions at 150, 250 and 350 °C show a substrate temperature dependent decrease that is followed by a gradual increase to values of ~18 Å, ~10 Å and ~9 Å after 180 s of deposition, respectively. It is clear from these results that the surface roughness for thick films decreases with increasing substrate temperature. A slightly different behavior of the bulk thickness and surface roughness versus deposition time was reported previously for a–Si:H deposited on crystalline silicon covered with native oxide¹⁴. The MSE depicted by the open symbols in Fig. 2 (e), which is a measure for the quality of the fit (see Sec. III.A), reaches a maximum at 30–60 seconds deposition time. In the next 60–90 seconds it decreases significantly, after which it remains approximately constant. After 180 seconds, the surface roughness increases slowly for all temperatures, which is normal for steady state a–Si:H growth. Fujiwara *et al.* found a similar maximum in fit error for plasma enhanced chemical vapor deposited a–Si:H films, which was attributed to a change in the dielectric function of the ultrathin film combined with an increase in the void fraction of the Bruggeman effective medium approximation used to describe the surface roughness [29]. In the next section it will be shown that the MSE does not show a clear maximum when the dielectric function comprises a thickness dependent bandgap.

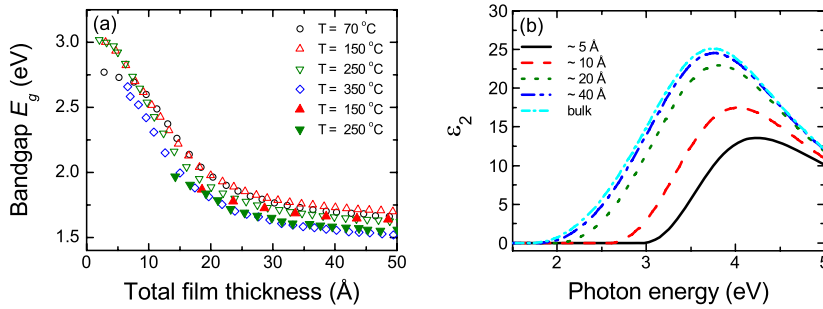


Figure 3: (a) The variation of the bandgap parameter E_g as a function of the film thickness deduced from the fits of the RTSE spectra. Open symbols correspond to films deposited on GaAs substrates and closed symbols to films deposited on c-Si. (b) An example of the imaginary part of the dielectric function ϵ_2 of an a-Si:H film deposited at 150 °C on a GaAs substrate in the thickness range from ~ 5 Å to ≥ 50 Å (bulk film).

B. RTSE data analysis with variable bandgap

The broad peak in fit error (MSE) observed in Fig. 2 (e) coincides with the region in which most of the dynamics in the surface roughness evolution occur. This questions the reliability of the suggested data analysis procedure in this region. In an attempt to improve the fit in the initial part of the deposition, the bandgap in the CL parameterization of the a-Si:H was allowed to vary. The choice for a varying a-Si:H bandgap was inspired by other studies that reported a higher bandgap for ultrathin films, such as the studies of a-Si:H/SiO₂ multilayer structures by Lockwood *et al.* [18,19] and a typical dielectric function of ultrathin a-Si:H observed by RTSE [29]. As can be seen in Fig. 2 (e), incorporating a varying bandgap lowers the MSE values in the first 120 s of the deposition significantly compared to the analysis with a thickness independent dielectric function that was described in the previous section. Also the surface roughness evolution is marginally affected by the inclusion of variable bandgap in the data analysis procedure as is shown in Fig. 2 (a)–(d) and discussed in Sec. IV.D. Figure 3 (a) shows the bandgap variation as a function of the total film thickness deduced from the RTSE analysis for all depositions. The behavior of the bandgap energy as a function of the film thickness shows similar behavior for all films studied, regardless of the deposition temperature or substrate used. In the first 50 Å of the deposition the bandgap decreases from ~ 3 eV to the bulk bandgap value, which varies between 1.5 and 1.7 eV depending on the substrate temperature. The depositions on c-Si show the same trend, but due to the limited optical contrast between the c-Si substrate and the depositing film it was not possible to determine the bandgap in the first 15 Å of growth. As an example, the corresponding change in

the imaginary part of the dielectric function ε_2 [from Eqs. (2) and (4)] is shown in Fig. 3 (b) for a total film thickness d_t that progresses from ultra-thin films to bulk values ($\gg 50 \text{ \AA}$). Besides the increase of the bandgap energy, also the height of ε_2 decreases for ultrathin films*. A similar reduction of the height of the dielectric function was predicted by atomistic calculations for Si quantum dots by Wang *et al.* [31].

Furthermore, it has been verified that a varying void fraction in the surface roughness layer (affecting the amplitude of the dielectric function, not the bandgap) only yields a marginal reduction of the MSE (not shown). Therefore, we have chosen to neglect a possible change in void fraction in our analysis to avoid increased complexity of the optical modeling. In the Sec. IV.D, the consequences of including a variable bandgap on the surface roughness evolution extracted from the RTSE modeling will be examined, but first possible origins of the thickness dependence of the bandgap will be discussed.

C. Thickness dependent bandgap: physical origin

Several authors have observed a higher bandgap for ultrathin a-Si:H films compared to the bulk value using various diagnostics. Yet the discussion about the origin of this effect has not completely settled [15–20]. In the literature, two explanations for the increased bandgap of ultrathin films are commonly suggested: (i) an increased hydrogen content and (ii) quantum confinement effects of the electron wavefunction. Fujiwara *et al.* attributed the observed $\sim 0.2 \text{ eV}$ blueshift compared to the bulk dielectric function of a 17 \AA thick a-Si:H film deposited on a c-Si substrate to a higher H content in the initial layer [29]. In an earlier study the same group reported a blue shift of the bandgap for a-Si:H as well as for c-Si films with decreasing film thickness [15]. For the c-Si films, this effect was attributed to confinement of the electron wavefunction in the material, while for the a-Si:H films an excess H content was suggested as the cause for the bandgap shift.

Recently, we demonstrated that a-Si:H films deposited on GaAs substrates also have a hydrogen rich interface layer [8], while it is generally accepted that the bandgap E_g increases with hydrogen content [H] for bulk a-Si:H [32,33]. Therefore, excess hydrogen content is a likely candidate to contribute to the increased bandgap for ultrathin films. Quantum confinement on the other hand, can take place when the film thickness is smaller than the localization length of the electron wavefunction. A well known example can be found in the etching of c-Si to a porous material. When the film becomes more porous, an increase in bandgap is observed by a clear blue

* Note that the height of ε_2 changes despite the constant amplitude parameter A in the CL parameterization (Eq. 2).

shift of the photoluminescence (PL) peak energy [34,35]. For a-Si:H however, conflicting results have been reported in the literature. In the etching of a-Si:H to a porous variant the PL peak energy remained at the same position [36], which indicates that the localization length of the electron wavefunction might be too short for quantum confinement effects on the lengths scales in the porous amorphous silicon (30–50 Å). This was also suggested by Mott who estimated the localization length of the electron wavefunction in a-Si:H to be ~10 Å compared to ~50 Å in c-Si [37]. On the basis of this statement quantum confinement effects in a-Si:H films thicker than ~10 Å are unlikely. Nevertheless, Park *et al.* have shown that quantum confinement is possible in 24 Å sized a-Si:H quantum dots in an a-SiN_x:H matrix [38]. This observation is supported by theoretical work by Nishio *et al.*, who calculated the size dependence of the peak energy in the emission of a-Si quantum dots in an a-SiN_x:H matrix [39] and find perfect agreement with the experimental results of Park *et al.* More experimental evidence for quantum confinement in 10–30 Å thick hydrogen deficient a-Si layers was given by Lockwood and coworkers, who measured the blue shift of the photoluminescence peak energy in MBE grown a-Si/SiO_x superlattices as a function of the a-Si film thickness. The blue shift observed was corroborated by independent soft X-ray Si L_{2,3} edge absorption spectroscopy, which probes the shift in the conduction band minimum and valence band maximum [18,19]. The observed energy gap shift $E_g - E_{g,\text{bulk}}$ could be accurately fitted by an effective mass model for one dimensionally confined Si assuming infinite potential barriers:

$$E_g - E_{g,\text{bulk}} = \frac{C}{d^2}, \quad (5)$$

with the confinement parameter C defined as:

$$C = \frac{\pi^2 \hbar^2}{2} \left(\frac{1}{m_e^*} + \frac{1}{m_h^*} \right). \quad (6)$$

In this expression m_e^* and m_h^* are the electron and hole effective masses and d is the film thickness. The experimental results by Lockwood *et al.* were reproduced theoretically by Nishida *et al.*, who calculated the electronic structures of ultrathin Si (100) films and concluded that the MBE grown a-Si are almost crystalline [40]. More theoretical support for the existence of the quantum confinement effect comes from Allan *et al.* who calculated the electronic structure of amorphous silicon clusters within the tight binding approximation and concluded that one should expect blueshifts with the reduction in size comparable to what is reported for c-Si clusters [41]. In a separate publication, they report that quantum confinement effects can be expected in a-Si layers with a thickness below 30 Å [42]. In the next two sections, we will discuss an increased hydrogen content as well as the quantum confinement effect

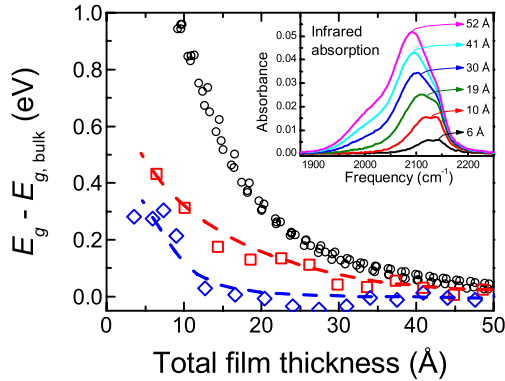


Figure 4: The bandgap shift $E - E_{g, \text{bulk}}$ calculated on the basis of the hydrogen content deduced from *in situ* infrared absorption measurements shown for the depositions at a substrate temperatures of 70 °C (open squares) and 350 °C (open diamonds). The lines are a guide to the eye. Furthermore, the bandgap shifts deduced from the RTSE analysis are represented by the open circles for all substrate types and temperatures used. The inset shows the absorption spectra of the film deposited at 70 °C at several values of the film thickness. These absorption spectra were used to calculate the bandgap shift on the basis of the hydrogen content.

as possible explanations for the higher bandgap for ultrathin films with respect to the bandgap value for bulk films.

Increased hydrogen content

Several studies have shown that the initial layer in a-Si:H growth is relatively hydrogen rich compared to the bulk film [8,9]. The contribution of this higher hydrogen content near the interface to the increase of the bandgap observed can be estimated by a measurement of the hydrogen content as a function of the film thickness. As mentioned in Sec. II, the hydrogen content was measured *in-situ* and real-time by infrared absorption spectroscopy in the so-called attenuated total reflection geometry (ATR) [8,9,22] simultaneously with the RTSE experiments. The inset in Fig. 4 shows the infrared absorption due to SiH and SiH₂ groups in an a-Si:H film with increasing thickness deposited at 70 °C. Assuming thickness independent absorption cross sections of the SiH and SiH₂ groups [43], the infrared absorption spectra were used to determine an upper estimate of the bonded atomic H content as a function of the film thickness. As reported in Ref. 8, this analysis revealed a hydrogen-rich interface layer, which was corroborated by secondary ion mass spectrometry measurements. Subsequently, the value of the bandgap corresponding to the hydrogen content at a certain film thickness was calculated from the relation between the hydrogen content [H] and bandgap derived from measurements for thick a-Si:H films: $E_g = (1.34 \pm 0.06) + (21 \pm 4) \times 10^{-3} \times [H]$. This relation is in good agreement with results presented in Refs. 44, 45, and 46. Figure 4 shows the bandgap shift

$E_g - E_{g,\text{bulk}}$ with respect to the bulk value $E_{g,\text{bulk}}$ calculated from the H content as a function of the total film thickness as well as the bandgap shifts obtained from the RTSE measurements. Both data sets show a higher bandgap shift for thinner films, but the bandgap shifts obtained from the RTSE measurements are clearly higher than the ones deduced from the H content measured by infrared absorption spectroscopy. These observations suggest that the observed bandgap shift can not be fully attributed to the increased hydrogen content. Moreover, the bandgap shifts extracted from the RTSE measurements are independent of the substrate temperature, while the bandgap shift deduced from the infrared measurements is not. This indicates that the observed higher bandgap for thinner films is probably not completely caused by the increased hydrogen content of the ultrathin films.

Another argument supporting the conclusion that the higher bandgap for ultrathin films is not caused by a high initial hydrogen content, follows from RTSE modeling of thick a-Si:H films. When we assume that a hydrogen rich interface layer is responsible for the increased bandgap, the optical model used for the RTSE data analysis of films thicker than $\sim 50 \text{ \AA}$ should be extended with a high bandgap interface layer between substrate and bulk a-Si:H film. The inclusion of such a high bandgap interface layer in the optical model, however, does not result in lower but in higher MSE values for the fits of the RTSE spectra of the thick films. The quantum confinement effect on the other hand, is only present for ultrathin films and disappears for films thicker than $\sim 50 \text{ \AA}$, which is exactly what we observe in our data. In addition, it was shown by Jun *et al.* that the blue shift in the dielectric function for thin a-Si:H films remains after all atomic H was removed from the samples by annealing the a-Si:H at $600 \text{ }^\circ\text{C}$ [17]. The abovementioned observations basically exclude hydrogen as the only origin of the increased bandgap observed for ultrathin films. However, a minor contribution of the excess hydrogen content to the higher bandgap for ultrathin films, can not be excluded on the basis of these data.

Quantum confinement

As discussed before, an alternative explanation for the increased bandgap observed in the experiments is the quantum confinement effect. Figure 5 shows the bandgap shift $E - E_{g,\text{bulk}}$ deduced from the RTSE measurements and several literature values of bandgap shifts that have been attributed to quantum confinement effects in a-Si:H, such as the studies reported by Lockwood *et al.* [19], Allan *et al.* [40] and Nishida [42]. The lines in Fig. 5 are fits by the simple approximation of 1D quantum confinement given by Eq. (5), while the inset shows the same data on a double logarithmic scale. The bandgap shift determined by the RTSE measurements shows a $1/d^2$ behavior that is characteristic for quantum confinement. Only for a film thickness $< \sim 10 \text{ \AA}$, the data and the fit show a deviation, which could be caused by the

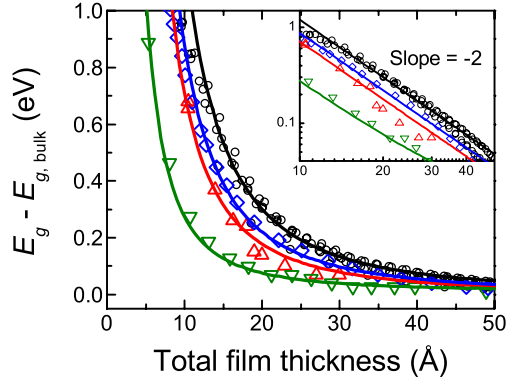


Figure 5: The bandgap shift $E_g - E_{g, \text{bulk}}$ as a function of the total film thickness deduced from the RTSE analysis (open circles). Also values from thin film structures that include amorphous silicon reported in the literature are shown (triangle up–Lu *et al.* [18], triangle down–Allan *et al.* [42], squares–Nishida *et al.* [40]). The lines are fits to the data using a $1/d^2$ relation that is characteristic for 1D quantum confinement. The inset shows the same data with double logarithmic axes.

limited optical contrast between substrate and film in the RTSE measurements for such thin films. The extracted value for the confinement parameter C of $120 \pm 4 \text{ eV}\text{\AA}^2$ is in fair agreement with literature values for the electron and hole effective masses in a–Si:H. Using $m_e^* = (0.3 \pm 0.1)$ and $m_h^* = (1.0 \pm 0.1)$ for the effective masses of electrons and holes in a–Si:H [47] respectively, a confinement parameter of $165 \pm 70 \text{ eV}\text{\AA}^2$ is found*. These results clearly suggest quantum confinement as the origin of the higher bandgap for ultrathin films.

D. Implications for the surface roughness evolution.

For the RTSE fitting in this study, we chose to adapt a varying bandgap in the first 50 Å of film growth to account for the change in the dielectric function. As was demonstrated in Fig. 2 (e), this modification to the data analysis procedure significantly improves the fit quality and produces consistent fit results. In the Figs. 2 (a)–(d) we compare the behavior of the surface roughness as a function of the deposition time obtained from the RTSE analysis using the thickness independent bandgap (Sec. III.A) and the varying bandgap method (Sec. III.B). When the varying

* It is remarkable that the confinement parameters extracted from the results of Nishida and Lockwood *et al.* show better agreement with the value expected for a c–Si film than with the value for an a–Si:H film. This might indicate that the ultrathin films show a quasi–crystalline structure, as was also suggested by Nishida.

bandgap method is used for fitting, the initial increase in surface roughness is smaller compared to the method with the thickness independent bandgap. The surface roughness is also lower in the subsequent region until approximately 90 s deposition time when the bandgap is varied. For films thicker than 50 Å (~90 s deposition time), no difference between both analysis methods is observed. The general trends as described in Sec. IV.A, however, are the same for both fitting methods. For the temperature range studied, these trends in the surface roughness versus deposition time have been attributed to physical phenomena in previous work: (a) heterogeneous nucleation in the first 20 seconds of growth (typical film thickness 10 Å), followed by (b) coalescence of the nuclei and temperature dependent smoothing on a relatively small lateral length scale (film thickness from 10 Å to ~75 Å), and finally (c) surface roughening on larger lateral length scales (films thicker than ~75 Å) [6,7,14]. The relatively minor changes in the observed trends imply that the conclusions based on the surface roughness evolution drawn by several authors are still valid. For instance the nucleation density on the native oxide surface calculated from the initial roughness increase due to heterogeneous nucleation would be in the range of $(1-2)\times 10^{13} \text{ cm}^{-2}$ for both fitting methods.

V. Conclusions

The thickness–evolution of the dielectric function of a–Si:H was studied by real–time spectroscopic ellipsometry during hot–wire chemical vapor deposition. The dielectric functions of thick a–Si:H films were determined directly from the data without assumptions about their shape and could be parameterized best by the Cody–Lorentz rather than by the Tauc–Lorentz parameterization. For ultrathin films ($d < 50 \text{ Å}$) the data analysis procedure using a constant dielectric function over the whole film thickness could be improved significantly by incorporating a higher bandgap for thinner films via the Cody–Lorentz parameterization. Although the varying bandgap in the RTSE analysis greatly improved the fit quality in the first 50 Å, the evolution of the surface roughness was only marginally affected. The magnitude of the surface roughness decreases slightly in the first 50 Å of growth, but the general trends described in previous studies remain nearly unaffected. This implies that spectroscopic ellipsometry can be used with confidence for the analysis of the surface roughness of ultrathin films.

Two possible explanations for the higher bandgap of ultrathin films that were suggested in the literature have been discussed in this Chapter. First, we argued that the higher hydrogen content in the interface region measured by infrared absorption spectroscopy can not explain the higher bandgap for ultrathin films. Alternatively, we demonstrated that this bandgap shift can be accurately fitted by a $1/d^2$ relation,

which is characteristic for 1 D quantum confinement. Furthermore, our data show resemblance with studies (both experimental as well as modeling studies) that attribute the higher bandgap in ultrathin a-Si:H structures to quantum confinement effects. On the basis of our data we suggest therefore that the observed phenomenon of a higher bandgap for ultrathin films is caused by quantum confinement.

Acknowledgements

M.J.F. van de Sande, J.F.C. Jansen, and J.J.A. Zeebregts are acknowledged for their skilful technical assistance. This study has been supported by the Netherlands Foundation for Fundamental Research on Matter (FOM) and by the Netherlands Ministry of Economic Affairs, the Ministry of Education, Culture and Science and the Ministry of Public Housing, Physical Planning and Environment (E.E.T. project “HR-CEL”). The research of W.M.M.K. has been made possible by a fellowship of the Royal Netherlands Academy of Arts and Sciences (KNAW).

References

- [1] D.B. Mitzi, L.L. Kosbar, C.E. Murray, M. Copel, and A. Afzali, *Nature* **428**, 299 (2004).
- [2] M. Taguchi, K. Kawamoto, S. Tsuge, T. Baba, H. Sakata, M. Morizane, K. Uchihashi, N. Nakamura, S. Kiyama, and O. Oota, *Progress in Photovoltaics* **8**, 503 (2000).
- [3] N. Jensen, R.M. Hausner, R.B. Bergmann, J.H. Werner, and U. Rau, *Progress in Photovoltaics* **10**, 1 (2002).
- [4] C.J. Först, C.R. Ashman, K. Schwarz, and P.E. Blöch, *Nature* **427**, 53 (2003).
- [5] Y. Yan, M. Page, T.H. Wang, M.M. Al-Jassim, H.M. Branz, and Q. Wang, *Appl. Phys. Lett.* **88**, 121925 (2006).
- [6] R. W. Collins, A. S. Ferlauto, G. M. Ferreira, C. Chen, J. Koh, R. J. Koval, Y. Lee, J. M. Pearce and C. R. Wronski, *Solar Energy Materials and Solar Cells* **78**, 143 (2003).
- [7] R.W. Collins, and B.Y. Yang, *J. Vac. Sci. Technol. B* **7**, 1155 (1989).
- [8] P.J. van den Oever, J.J.H. Gielis, M.C.M. van de Sanden and W.M.M. Kessels, submitted for publication in *Thin Solid Films*; Chapter 6.
- [9] H. Fujiwara, Y. Toyoshima, M. Kondo, and A. Matsuda, *Phys. Rev. B* **60**, 13598 (1999).
- [10] S. de Wolf, and G. Beaucarne, *Appl. Phys. Lett.* **88**, 022104 (2006).
- [11] J.S. Christensen, A.G. Ulyashin, K. Maknys, A.Yu. Kuznetsov, and B.G. Svensson, *Thin Solid Films* **511–512**, 93 (2006).
- [12] Y. Cong, I. An, H.V. Nguyen, K. Vedam, R. Messier, and R.W. Collins, *Surface and Coatings Technology* **49**, 381 (1991).
- [13] H. Fujiwara, and M. Kondo, *Appl. Phys. Lett.* **86**, 032112 (2005).
- [14] W.M.M. Kessels, J.P.M. Hoefnagels, E. Langereis, and M.C.M. van de Sanden, *Thin Solid Films* **501**, 88 (2006).
- [15] H.V. Nguyen, Y. Lu, S. Kim, M. Wakagi, and R.W. Collins, *Phys. Rev. Lett.* **74**, 3880 (1995).
- [16] S. Hazra, I. Sakata, M. Yamanaka, and E. Suzuki, *Appl. Phys. Lett.* **80**, 1159 (2002).
- [17] K. H. Jun, K. S. Lim, S. Y. Kim, and S. J. Kim, *J. Non-Cryst. Solids* **275**, 59 (2000).
- [18] Z.H. Lu, D.J. Lockwood, and J. –M. Baribeau, *Nature* **378**, 258 (1995).
- [19] D.J. Lockwood, Z.H. Lu, and J. –M. Baribeau, *Phys. Rev. Lett.* **76**, 539 (1996).
- [20] M. Beaudoin, M. Meunier, and C.J. Arsenaault, *Phys. Rev. B* **47**, 2197 (1993).
- [21] A.S. Ferlauto, G.M. Ferreira, J.M. Pearce, C.R. Wronski, R.W. Collins, X. Deng, and G. Ganguly, *J. Appl. Phys.* **92**, 2424 (2002).
- [22] D.C. Marra, E.A. Edelberg, R.L. Naone, and E.S. Aydil, *J. Vac. Sci. Technol. A* **16**, 3199 (1999).

- [23] I.M.P. Aarts, J.J.H. Gielis, M.C.M. van de Sanden, and W.M.M. Kessels, *Phys. Rev. B* **73**, 045327 (2006).
- [24] E.C. Molenbroek, A.H. Mahan, and A. Gallagher, *J. Appl. Phys.* **82**, 1909 (1997).
- [25] D.E. Sweenor, S.K. O'Leary, and B.E. Foutz, *Solid State Communications* **110**, 281 (1999).
- [26] EASE 2.30, J. Hale and B. Johs, Copyright 1999-2004, J.A. Woollam Co., Inc.
- [27] H. Arwin, and D.E. Aspnes, *Thin Solid Films* **113**, 101 (1984).
- [28] I. An, Y.M. Li, H.V. Nguyen, C.R. Wronski, and R.W. Collins, *Appl. Phys. Lett.* **59**, 2543 (1991).
- [29] H. Fujiwara, J. Koh, P. I. Rovira, and R. W. Collins, *Phys. Rev. B*, **61**, 10832 (2000).
- [30] A.S. Ferlauto, G.M. Ferreira, J.M. Pearce, C.R. Wronski, R.W. Collins, X. Deng, and G. Ganguly, *Thin Solid Films* **455**, 388 (2004).
- [31] L-W. Wang, and A. Zunger, *Phys. Rev. Lett.* **73**, 1039 (1994).
- [32] G. Cody, C.R. Wronski, B. Abeles, R.B. Stephens, and B. Brooks, *Solar Cells* **2**, 227 (1980).
- [33] W. Futako, T. Kamiya, C.M. Fortmann, I. Shimizu, *J. Non-Cryst. Solids* **266**, 630 (2000).
- [34] D.J. Lockwood, *Solid State Comm.* **92**, 101 (1994).
- [35] A.G. Cullis, L.T. Canham, and P.D.J. Calcott, *J. Appl. Phys.* **82**, 909 (1997).
- [36] R.B. Wehrspoon, J.-N. Chazalviel, R. Ozanam, and I. Solomon, *Eur. Phys. J.* **8**, 179 (1999).
- [37] N. F. Mott, *Phil. Mag.* **B43**, 941 (1981).
- [38] N-M. Park, C.-J. Choi, T-Y. Seong, and S-J. Park, *Phys. Rev. Lett.* **86**, 1355 (2001).
- [39] K. Nishio, J. Koga, T. Yamaguchi, and F. Yonezawa, *Phys. Rev. B* **67**, 195304 (2003).
- [40] M. Nishida, *Phys. Rev. B* **59**, 15789 (1999).
- [41] G. Allan, C. Delerue, and M. Lannoo, *Phys. Rev. Lett.* **78**, 3161 (1997).
- [42] G. Allan, C. Delerue, and M. Lannoo, *Appl. Phys. Lett.* **71**, 1189 (1997).
- [43] A.H.M. Smets, W.M.M. Kessels, and M.C.M. van de Sanden, *Appl. Phys. Lett.* **82**, 1547 (2003).
- [44] L. Ley, in *The physics of Hydrogenated Amorphous Silicon II*, edited by J. D. Hoannopoulos and G. Lucovsky (Springer, Berlin, 1984), Vol. 56, p. 61.
- [45] K. Fukutani, M. Kanbe, W. Futako, B. Kaplan, T. Kamiya, C. M. Fortmann, and I. Shimizu, *J. Non-Cryst. Solids* **227–230**, 63 (1998).
- [46] J.P.M. Hoefnagels, Ph.D. Thesis, Eindhoven University of Technology, The Netherlands
- [47] R.A. Street, *Hydrogenated amorphous silicon*, (Cambridge University press, Cambridge 2005).

Chapter 6

Hot-wire deposition of a-Si:H thin films on wafer substrates studied by real-time spectroscopic ellipsometry and infrared spectroscopy^{*}

Film growth of hydrogenated amorphous silicon (a-Si:H) by hot-wire chemical vapor deposition was studied simultaneously and in real-time by spectroscopic ellipsometry and attenuated total reflection infrared spectroscopy. The a-Si:H films were deposited on native oxide-covered GaAs(100) and Si(100) substrates at temperatures ranging from 70 to 350 °C. A temperature dependent initial growth phase is revealed by the evolution of the surface roughness and the surface and bulk SiH_x absorption peaks. It is discussed that the films show a distinct nucleation behavior by the formation of islands on the surface that subsequently coalesce followed by bulk a-Si:H growth. Insight into a temperature-activated smoothening mechanism and the creation of a hydrogen-rich interface layer is presented.

^{*} Accepted for publication in Thin Solid Films: P.J. van den Oever, J.J.H. Gielis, M.C.M. van de Sanden, and W.M.M. Kessels

I. Introduction

Initial growth of hydrogenated amorphous silicon (a-Si:H) and the subsequent evolution of the material properties as a function of the film thickness is an interesting area of research, which becomes more relevant with the increasing amount of applications of thin a-Si:H films on wafer substrates. Very thin (<100 Å) a-Si:H films on crystalline silicon substrates are applied in heterojunction solar cells [1] and for backside surface passivation schemes of diffused emitter solar cells [2]. Furthermore, information on the growth of ultrathin a-Si:H films is important to understand the breakdown to the amorphous phase in the epitaxial growth of thin crystalline silicon films [3,4].

Several questions with respect to the nucleation of an a-Si:H film on the substrate, the coalescence of the nucleation sites at increasing film thickness, and the formation of a hydrogen-rich interface layer, remain unresolved although it is clear that the substrate temperature is a key parameter. It is generally difficult to obtain insight in these aspects as this requires real-time measurements during film growth that do not disturb the deposition process. It was already shown that spectroscopic ellipsometry (SE) is well suited for real time studies of the initial growth process [5], but the combination of SE with attenuated total reflection (ATR) infrared spectroscopy is even more powerful. This all-optical and non-intrusive approach was already applied by Fujiwara and co-workers for plasma-enhanced chemical vapor deposition (PECVD) of a-Si:H [6,7]. Although the data analysis of these real-time measurements requires optical modeling and deconvolution of spectra, Fujiwara and co-workers were able to obtain detailed insight into the growth of a-Si:H on native-oxide covered and H-terminated Si(100) substrates for a substrate temperature of 240 °C and 130 °C, respectively. In the present study, we apply the combination of both techniques to a-Si:H films grown on native oxide covered GaAs(100) and Si(100) substrates at temperatures between 70 to 350 °C. The films were deposited by hot-wire chemical vapor deposition (HWCVD), which is the method of choice for high-rate deposition and also for well-controlled growth of a-Si:H without ion bombardment. Hot-wire deposited silicon films have also been used successfully in heterojunction solar cells [8] and epitaxial growth studies [4,9].

II. Experiment

The a-Si:H films were deposited in an ultrahigh vacuum setup [see Fig. 1 (a)] by HWCVD using SiH₄ (purity $> 99.99\%$) at a pressure of 8×10^{-3} mbar and a hot-wire temperature of $\sim 2000 \pm 200$ °C. The SiH₄ flow rate was 3 sccm and the filament, which was heated by a DC current of ~ 10 A, was positioned at a distance of 11 cm from the

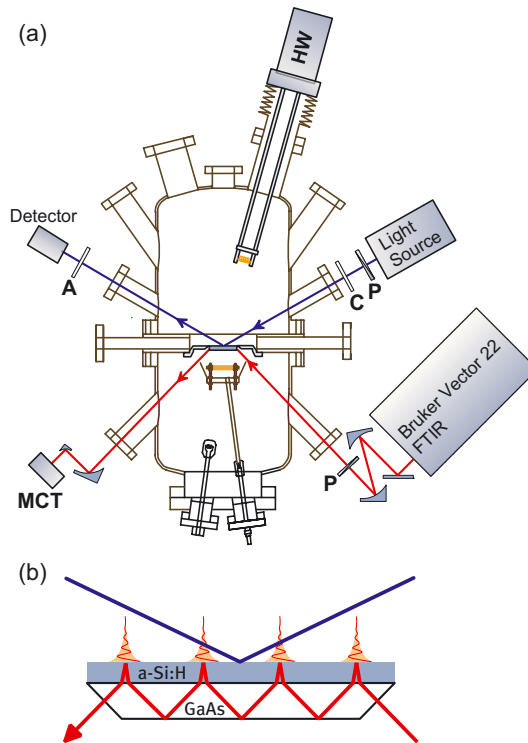


Figure 1: (a) A schematic overview of the ultrahigh vacuum system consisting of a deposition chamber and a backside chamber for optical access to the substrate which is positioned at the flange separating the two chambers. The filament for HWCVD is positioned in the deposition chamber, the substrate heater in the backside chamber. The figure also shows the setups for spectroscopic ellipsometry (SE) and attenuated total reflection (ATR) infrared spectroscopy. In the figure “HW” stands for hot-wire, “P” for polarizer, “C” for compensator, “A” for analyzer, and “MCT” for Mercury Cadmium Telluride. (b) An enlargement of the sample region schematically showing the a-Si:H film on the ATR substrate including the ellipsometry and infrared beam path.

double side polished GaAs(100) or Si(100) substrates used in this study. These settings correspond to optimal conditions for hot-wire a-Si:H deposition as reported by Molenbroek *et al.* [10]. The substrates were cut trapezoidal (50 mm × 20 mm × 0.7 mm) with 45° angled bevels (i.e., so-called ATR substrates) and were cleaned ultrasonically in ethanol, while no efforts were made to remove the native oxide. Subsequently, the substrates were mounted in the setup and baked at 150 °C overnight prior to heating or cooling down to the desired deposition temperature. The growth rate was ~30 Å/min for the conditions described.

Spectroscopic ellipsometry (SE) measurements were carried out with a J.A. Woollam M-2000U rotating compensator ellipsometer with a photon energy range of 1.24–5 eV. The ellipsometry light beam entered the setup at the deposition side through strain-free windows at an angle of incidence of $\sim 60^\circ$ [see Fig. 1(a)]. For every data point, 25 spectra were averaged to obtain a good signal-to-noise ratio leading to a time resolution of ~ 3.5 s and a depth resolution of ~ 2 Å for the present condition. The data were analyzed by an optical model consisting of (i) a substrate with native oxide; (ii) a bulk a-Si:H layer; and (iii) a surface roughness layer. For a detailed description of the analysis procedure we refer to a separate paper [11]. The results on the thickness of the bulk layer d_b and surface roughness layer d_s are used in this Chapter. The (total) film thickness is represented by $d_b + \frac{1}{2}d_s$.

The attenuated total reflection (ATR) measurements took place from the backside vacuum chamber as depicted schematically in Fig. 1. The infrared (IR) radiation from the Bruker Vector 22 FTIR spectrometer entered and exited the vacuum through ZnSe windows and was polarized perpendicular to the plane of incidence by a wire grid polarizer. The beam was focused on the 45° angled bevels of the trapezoidal ATR substrates by parabolic gold mirrors. The IR beam underwent multiple internal reflections in the ATR substrate before emerging from the opposite bevel, where it was focused on a liquid nitrogen cooled HgCdTe (MCT) detector. The refractive index of the GaAs as well as Si ATR substrates closely match that of a-Si:H, yielding total internal reflection at the film-vacuum interface and not at the substrate-film interface. Furthermore, GaAs is IR transparent up to ~ 750 cm^{-1} at temperatures exceeding 350 $^\circ\text{C}$, in contrast to c-Si which only allows IR transmission at frequencies higher than ~ 1500 cm^{-1} and temperatures up to 150 $^\circ\text{C}$. In our configuration, the IR beam experiences approximately 35 total internal reflections on each side of the ATR substrate and, hence, the absorption path length in the film deposited on the ATR substrate is enhanced by approximately a factor of 70 compared to a normal transmission measurement. Before deposition, the background transmission T_0 was measured by averaging 500 scans while for the real-time measurements the number of averages was set to 15 scans. The calculation of the transmission T from the measured interferogram was carried out after the deposition to optimize the measurement repetition rate. With a resolution of 4 cm^{-1} , these settings led to a time resolution of ~ 6.8 s, which corresponds to a depth resolution of ~ 4 Å at a typical growth rate of ~ 30 Å/min. To accurately represent the absorption of the deposited film, the absorbance A is calculated from the measured transmission T and the background transmission T_0 using the expression $A = -\log(T/T_0)$. Small corrections were applied to obtain a flat baseline in the spectra before fitting absorption peaks in the deconvolution procedure.

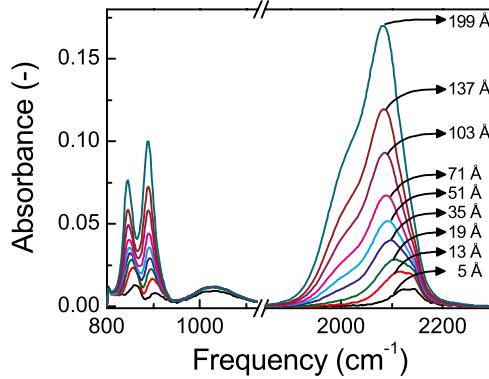


Figure 2: The measured absorbance during the deposition of an a-Si:H film at 70 °C (only selected spectra are shown for clarity). The region between 800 and 950 cm^{-1} is assigned to deformation and wagging modes of SiH_2 and SiH_3 and the peak at $\sim 1050 \text{ cm}^{-1}$ is due the stretching mode of Si-O-Si bonds located primarily at the interface between the a-Si:H and the native oxide covered GaAs substrate. The region between ~ 1900 and 2200 cm^{-1} is assigned to the stretching vibrations of SiH_x ($x=1,2,3$) both at the surface and in the bulk of the film.

III. Results

A. Infrared absorption spectra

Figure 2 shows the measured absorbance for a-Si:H deposited on GaAs at 70 °C in the thickness range from 5 Å to 200 Å. Two absorption regions due to SiH_x ($x=1,2,3$) bonds in the film can be distinguished in these spectra: (i) SiH_2 and SiH_3 deformation and wagging modes in the ~ 800 – 950 cm^{-1} region; and (ii) SiH_x stretching modes in the ~ 1900 – 2200 cm^{-1} region. Clearly, the measured absorbance in both regions increases with increasing film thickness. The presence of the deformation and wagging modes ($\sim 845 \text{ cm}^{-1}$ and $\sim 890 \text{ cm}^{-1}$) indicates a high content of SiH_2 and SiH_3 groups in the film as commonly observed at low substrate temperatures [12]. The observed peak at $\sim 1050 \text{ cm}^{-1}$ remains constant after its initial appearance and can be attributed to O–Si–O bonds formed at the interface between the native oxide covered GaAs substrate and the a-Si:H film [13]. Besides an increase in the amplitude of the absorbance, the stretching modes show also a shift in the position of the absorbance towards lower frequencies with increasing film thickness.

To obtain quantitative information about the evolution of the bonding of hydrogen versus time, the spectra in Fig. 2 were deconvoluted into several Gaussian peaks. Figure 3 (a) and (b) show the deconvolution of the thinnest ($\sim 5 \text{ Å}$) and thickest film ($\sim 200 \text{ Å}$) from Fig. 2, respectively. The spectrum of the thinnest film shows several relatively narrow peaks, attributed to SiH_x surface groups, while the spectrum of the thick film is dominated by two broad bulk peaks centered at $\sim 2000 \text{ cm}^{-1}$ [low

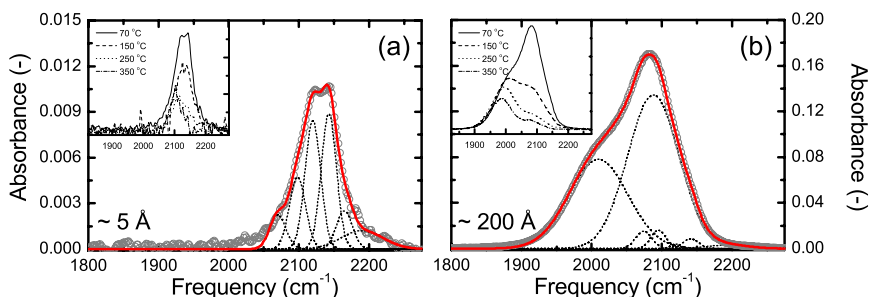


Figure 3: Infrared spectra obtained for an a-Si:H film at a thickness of (a) $\sim 5 \text{ \AA}$ and (b) $\sim 200 \text{ \AA}$ deposited at $70 \text{ }^\circ\text{C}$. The solid lines are the deconvolution of the spectrum into several Gaussian peaks (dotted lines), representing different SiH_x stretching modes either at the surface or in the bulk of the a-Si:H film. In the inset the spectra obtained for the different temperatures are compared.

stretching mode (LSM)] and $\sim 2090 \text{ cm}^{-1}$ [high stretching mode (HSM)]. Note that narrow SiH_x surface peaks are also necessary for a good deconvolution of the thick film spectrum, but the uncertainty in the amplitude and position of these peaks is considerably higher compared to thinner films due to correlation with the HSM peak. On the high frequency side above 2190 cm^{-1} , two relatively broad peaks due to oxygen backbonded SiH_x groups are detected in some cases [6,13]. Similar to the peak at $\sim 1050 \text{ cm}^{-1}$, these peaks are related to the interface formation on the native oxide and they do not increase in amplitude as film growth progresses.

The different surface peaks were assigned on the basis of data reported for different crystalline silicon surfaces [13]. The assignment was similar to the one employed by Marra *et al.* [14] and Fujiwara *et al.* [6] with possible small differences in peak deconvolution having negligible effect on the final interpretation. For the proportionality constants used to calculate the hydrogen content in the film and the assignment of the bulk peaks we follow Smets *et al.*, who assign the LSM to SiH in vacancies in the a-Si:H bulk and the HSM to SiH on void surfaces and to bulk SiH_2 [15]. A summary of the used assignments is given in Table 1. Finally, it is noted that in the deconvolution of the temperature dependent spectra, the positions and widths of the surface SiH_x peaks were kept constant for all temperatures, while they were allowed to vary as function of temperature for the LSM and HSM bulk peaks.

In the insets of Fig. 3, the spectra obtained at the different substrate temperatures are compared. When the temperature increases, the overall absorbance decreases in amplitude and shifts towards the lower frequency region in the spectrum for both the $\sim 5 \text{ \AA}$ and $\sim 200 \text{ \AA}$ thick film. This behavior indicates a decrease of the total amount of SiH_x bonds with increasing temperature. For ultrathin films, a clear shift

Table 1: The assignments of the infrared absorption peaks in the SiH_x stretching region of a-Si:H [13,14,15]. The full width at half maximum of a surface peak is typically 27 cm⁻¹ while the bulk peaks are ~85 cm⁻¹ wide.

Surface hydrogen		Bulk hydrogen	
Peak position (cm ⁻¹)	Assignment	Peak position (cm ⁻¹)	Assignment
2070–2080	SiH	1980–2020 (LSM ^a)	SiH in vacancies
2095–2105	SiH	2080–2095 (HSM ^b)	SiH ₂ / SiH on void surfaces
2110–2120	SiH ₂		
2135–2145	SiH ₃	2190–2210	SiH _x (O _y)
2155–2165	SiH(O ₂)	2240–2260	SiH(O ₃)

^a LSM: low stretching mode; ^b HSM: high stretching mode

from a mainly SiH₃ to a SiH dominated surface coverage can be observed when the substrate temperature increases [16,17], while for the thicker film the LSM becomes relatively more important with respect to the HSM.

B. The bonding of hydrogen and surface roughness evolution

In Fig. 4 the data obtained from the infrared spectra and the spectroscopic ellipsometry measurements are summarized for the different substrate temperatures. Figures 4 (a)–(d) show the peak area of the LSM, HSM, and the sum of the surface SiH_x peaks as a function of the film thickness while the surface roughness evolution (measured simultaneously) is given in Fig. 4 (e)–(h). The insets show typical atomic force micrographs of the a-Si:H surface morphology while also the microstructure parameter \bar{R}^* , the hydrogen content [H], and the surface roughness from the AFM and SE measurements are given for the final film thickness.

From Fig. 4, it is clear that [H] and \bar{R}^* decrease for increasing substrate temperatures. The values obtained from the ATR infrared spectroscopy are slightly higher than those obtained by Rutherford backscattering and infrared transmission measurements of 2000 Å thick a-Si:H films on native oxide covered c-Si substrates carried out in a separate study. The surface roughness of the films decreases with temperature as can be concluded from both the AFM and SE data while the relation between the AFM and SE roughness is similar as previously reported [18]. For the data on the bonding of hydrogen, the trends with thickness show similar behavior for all temperatures. The HSM increases relatively steep initially and levels off after ~20–25 Å of film growth, while the LSM remains zero in the initial growth phase. The SiH_x surface groups show a maximum in the first 20–25 Å for all temperatures while for 250 and 350 °C the large increase and subsequent decrease of the surface SiH_x groups is very pronounced. The surface roughness evolution shows a clear

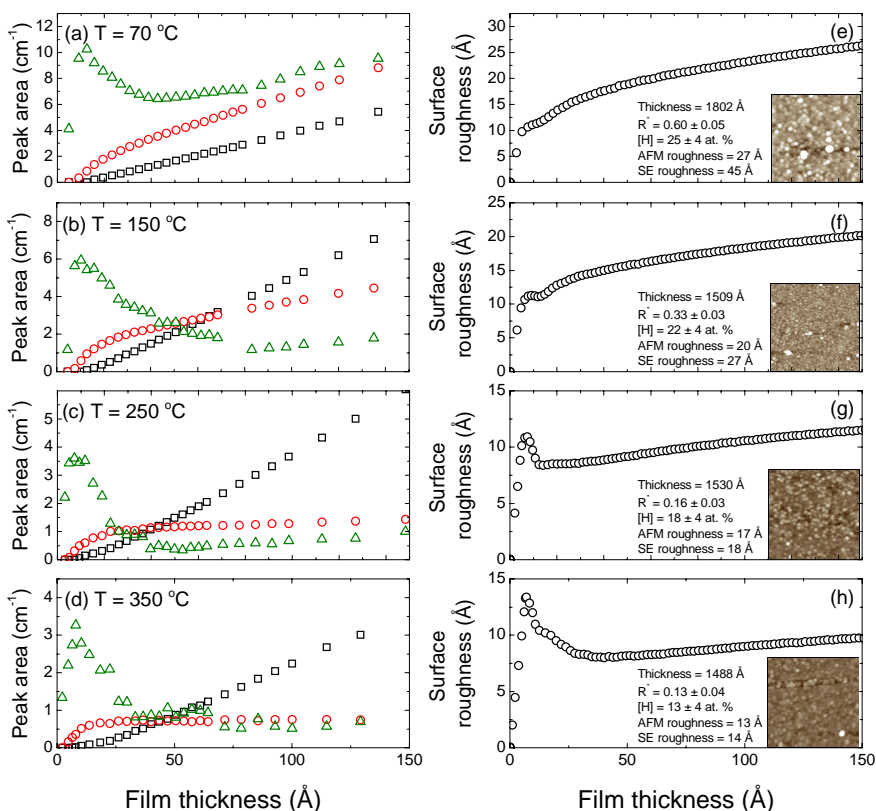


Figure 4: (a)-(d) The peak areas of the SiH_x stretching modes for the bulk low stretching mode (LSM, open squares), the bulk high stretching mode (HSM, open circles), and the sum of the SiH_x surface modes (open triangles) are shown as a function of the film thickness. (e)-(h) The surface roughness as a function of the film thickness. The insets show typical atomic force micrographs of the a-Si:H [scan area: 2 μm × 2 μm; height scale: 0 Å (black) - 150 Å (white)]. Also film properties such as the microstructure parameter R^2 , the hydrogen content [H], and the AFM and SE roughness are given for the final film thickness. The substrate temperatures are 70 °C for (a) and (e); 150 °C for (b) and (f); 250 °C for (c) and (g); and 350 °C for (d) and (h).

dependence on the substrate temperature. For all temperatures an initial increase in the roughness to a level of ~11–13 Å is observed. Subsequently, for the higher substrate temperatures the surface roughness reaches a maximum after which it decreases again, while for the lower substrate temperatures only a slower steady increase with film thickness takes place. Such a slow increase in surface roughness is eventually also observed for the higher substrate temperatures, but the rate of this steady state increase is significantly reduced at elevated temperatures.

Abovementioned results were obtained for films deposited on GaAs substrates with native oxide. From a comparison with results obtained for c-Si with native oxide at a temperature of 70 and 150 °C, only very minor differences between the data obtained on GaAs and c-Si were found. The aforementioned trends in the bonding of hydrogen and surface roughness evolution were similar and are probably ruled by the native oxide present at the substrates. However when comparing with previous data [19], for the higher temperatures some differences exist with respect to the magnitude of the decrease in the surface roughness after it reached a maximum. In the present data, the decrease in roughness is smaller and in good agreement with the work of Collins and co-workers [20]. It has been verified that this difference is not due to the SE data analysis procedure or substrate material, but it is probably related to a different substrate preparation [11,19].

IV. Discussion

Previously, the surface roughness evolution has been used to extract information about the microstructural evolution of the a-Si:H at the initial stage of film growth [19,20]. The present observations show a good agreement with the earlier data and therefore we discuss the microstructural evolution in more detail on the basis of the additional ATR infrared measurements by following the previously proposed interpretation [6,19,20].

The fast initial increase in surface roughness to a level of ~11–13 Å can be explained by heterogeneous nucleation on the native oxide covered substrate. The nucleation density of $(15-20) \times 10^{12} \text{ cm}^{-2}$ on the substrate is very similar to the one reported in Ref. [19]. During this nucleation phase also the sum of the SiH_x surface peaks increases rapidly for all temperatures which can be understood from the increase in the a-Si:H surface area when the islands start growing.

The fast increase in roughness stops when the point of coalescence of the islands is reached and at this thickness also the maximum in the SiH_x surface coverage is observed. In the subsequent phase, the surface roughness for 70 and 150 °C increases continuously but at a significantly slower rate. For 250 and 350 °C a decrease in surface roughness is observed which can be attributed to a surface smoothening mechanism that flattens out the nucleation-induced roughness when film closure is reached. This smoothening mechanism is thermally activated and might be ruled by a surface diffusion process acting at relatively short lateral length scales. The decrease in surface roughness is accompanied by a pronounced decrease in the SiH_x surface peak area which can be understood from the decrease in surface area. Probably also another effect leads to the reduction of the SiH_x surface peak area as the data at 70 and 150 °C also show a decrease albeit less pronounced. Hydrogen

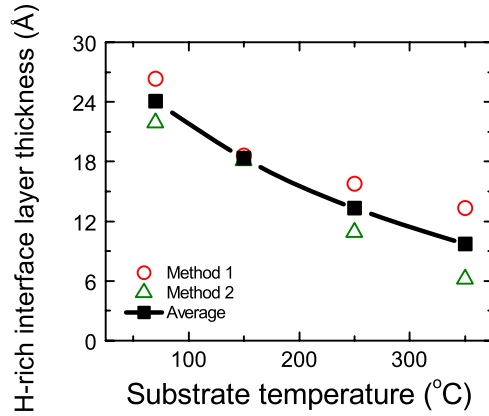


Figure 5: The approximated thickness of the H-rich layer formed at the interface in the initial stage of film growth as a function of substrate temperature. The thickness is given for two methods and the average value is shown as well.

is likely expelled from the surface for all temperatures when film closure is reached while it can also be converted into bulk hydrogen (*e.g.*, in the HSM which comes up at film closure).

When steady-state growth is reached, the surface roughness increases only slowly with film thickness, especially for the higher substrate temperatures. This is also revealed by the growth exponent β that can be calculated in the post-initial growth regime from the relation $d_s \propto d_b^\beta$. β decreases from 0.14 to basically 0 when increasing the temperature from 70 to 350 °C, in good agreement with previous results [19]. For 70 °C, the increase in surface roughness is still considerable which can be correlated to the small increase in the SiH_x surface area which is observed in Fig. 4(a). However, the increase in SiH_x surface peak area at 70°C might also be caused by the incorporation of SiH_x surface groups located in voids in the bulk material. For the other temperatures, the slight increase of the SiH_x surface peak area versus film thickness observed in Fig.4 cannot be distinguished from a constant value within the accuracy of the data.

The bulk HSM peak starts to increase at film closure and at a certain film thickness the *increase* in the HSM peak area levels off or even becomes constant. At that film thickness the LSM absorption peak has just appeared. From the data, it can be concluded that a hydrogen-rich layer exists at the interface in this early growth phase. The thickness of this interface layer can be estimated by determining the point where the increase in HSM levels off (method 1). Another approach (method 2) is to determine the position where the total hydrogen content becomes constant (this can basically be done by taking the derivatives of the peak areas versus film thickness).

Figure 5 shows that both approaches give similar values and that the average thickness of the H-rich layer formed in the initial film growth decreases from $\sim 24 \text{ \AA}$ at $70 \text{ }^\circ\text{C}$ to $\sim 10 \text{ \AA}$ at $350 \text{ }^\circ\text{C}$. From the present experiments it is not clear whether this H-rich layer remains located at the interface when growth proceeds or is divided in an H-rich *interface* layer and an H-rich *near-surface* layer. Secondary ion mass spectrometry has unambiguously shown that a more H-rich interface layer exists in deposited a-Si:H films. From an isotope experiment, Fujiwara *et al.* concluded that the H-rich layer in an a-Si:H film deposited at a substrate temperature of $240 \text{ }^\circ\text{C}$ is mainly located at the interface region near the native-oxide covered silicon substrate [6].

V. Conclusions

The combination of real time spectroscopic ellipsometry and attenuated total reflection infrared spectroscopy is applied to study the film growth of a-Si:H by HWCVD on native oxide-covered wafer substrates. From the evolution of the surface roughness and the bonding of hydrogen more insight is obtained into the microstructural evolution of the a-Si:H film in the initial growth phase. The temperature dependence of film growth aspects such as nucleation, coalescence and film closure, surface smoothing and roughening, and H-rich interface layer formation is discussed. In future work, these aspects will also be studied for a-Si:H film growth on H-terminated crystalline silicon substrates.

Acknowledgements

M.J.F. van de Sande, J.F.C. Jansen, and J.J.A. Zeebregts are acknowledged for their skilful technical assistance. This study has been supported by the Netherlands Foundation for Fundamental Research on Matter (FOM) and by the Netherlands Ministry of Economic Affairs, the Ministry of Education, Culture and Science and the Ministry of Public Housing, Physical Planning and Environment (E.E.T. project "HR-CEL"). The research of W.M.M.K. has been made possible by a fellowship of the Royal Netherlands Academy of Arts and Sciences (KNAW).

References

- [1] M. Taguchi, K. Kawamoto, S. Tsuge, T. Baba, H. Sakata, M. Morizane, K. Uchihashi, N. Nakamura, S. Kiyama and O. Oota, *Prog. Photovolt: Res. Appl.* **8**, 503 (2000).
- [2] M. Schaper, J. Schmidt, H. Plagwitz and R. Brendel, *Prog. Photovolt: Res. Appl.* **13**, 388 (2005).
- [3] D. J. Eaglesham, H.-J. Gossmann, and M. Cerullo, *Phys. Rev. Lett.* **65**, 1227 (1990).
- [4] C.W. Teplin, D.H. Levi, E. Iwaniczko, K.M. Jones, J.D. Perkins, and H.M. Branz, *J. Appl. Phys.* **97**, 103536 (2005).
- [5] R.W. Collins, B.Y. Yang, *J. Vac. Sci. Technol. B* **7**, 1155 (1989).
- [6] H. Fujiwara, Y. Toyoshima, M. Kondo, and A. Matsuda, *Phys. Rev. B* **60**, 13598 (1999).
- [7] H. Fujiwara, and M. Kondo, *Appl. Phys. Lett.* **86**, 032112 (2005).
- [8] T.H. Wang, E. Iwaniczko, M.R. Page, D.H. Levi, Y. Yan, H.M. Branz, and Q. Wang, *Thin Solid Films* **501**, 284 (2006).
- [9] C.E. Richardson, Y.-B. Park, and H.A. Atwater, *Phys. Rev. B* **73**, 245328 (2006).
- [10] E.C. Molenbroek, A.H. Mahan, and A. Gallagher, *J. Appl. Phys.* **82**, 1909 (1997).
- [11] P.J. van den Oever, J.J.H. Gielis, M.C.M. van de Sanden, and W.M.M. Kessels, submitted for publication; Chapter 5.
- [12] G. Lucovsky, R.J. Nemanich, and J.C. Knights, *Phys. Rev. B* **19**, 2064 (1979).
- [13] S.M. Han, and E.S. Aydil, *J. Vac. Sci. Technol. A* **14**, 2062 (1996).
- [14] D.C. Marra, E.A. Edelberg, R.L. Naone, and E.S. Aydil, *J. Vac. Sci. Technol. A* **16**, 3199 (1999).
- [15] A.H.M. Smets, W.M.M. Kessels, and M.C.M. van de Sanden, *Appl. Phys. Lett.* **82**, 1547 (2003).
- [16] D.C. Marra, W.M.M. Kessels, M.C.M. van de Sanden, K. Kashefzadeh, and E.S. Aydil, *Surf. Sci.* **530**, 1 (2003).
- [17] W.M.M. Kessels, J.P.M. Hoefnagels, P.J. van den Oever, Y. Barrell, and M.C.M. van de Sanden, *Surf. Sci. Lett.* **547**, L865 (2003).
- [18] H. Fujiwara, M. Kondo, and A. Matsuda, *Phys. Rev. B* **63** (2001) 115306.
- [19] W.M.M. Kessels, J.P.M. Hoefnagels, E. Langereis, and M.C.M. van de Sanden, *Thin Solid Films* **501**, 88 (2005).
- [20] R.W. Collins, A.S. Ferlauto, G.M. Ferreira, C. Chen, J. Koh, R.J. Koval, Y. Lee, J.M. Pearce, C.R. Wronski, *Sol. Energy Mater. Sol. Cells* **78**, 143 (2003).

Summary

In situ studies of silicon–based thin film growth for crystalline silicon solar cells

First generation, crystalline silicon solar cell technology currently dominates the photovoltaic market, but several technological as well as fundamental developments are needed to sustain a leading position that enables wide-scale implementation of solar electricity. In the manufacturing technology high-throughput systems for the deposition of functional materials applied in solar cells are required, while improved solar cell concepts that yield higher conversion efficiencies or a facilitated fabrication process are crucial to further reduce the costs per unit energy produced. This thesis work concentrates on two key issues in the deposition process of silicon–based thin films for crystalline silicon solar cells.

First, the deposition of amorphous silicon nitride ($a\text{-SiN}_x\text{:H}$) antireflection coatings using the expanding thermal plasma (ETP) source was addressed. Optimization of the deposition process in a high throughput industrial system has established excellent surface and bulk passivation properties of the $a\text{-SiN}_x\text{:H}$ antireflection coatings. A full characterization of the ETP plasma source applied in the industrial system was carried out. The reactive species emanating from the plasma source operated on an Ar-NH_3 gas mixture were investigated using a combination of several advanced diagnostics. The absolute densities of N, NH and NH_2 radicals in the plasma were measured using threshold ionization mass spectrometry and cavity ring-down absorption spectroscopy, while the density and composition of the ions in the plasma were investigated by Langmuir probe and mass spectrometry. Detailed analysis of the observed trends in radical and ion densities versus important plasma parameters revealed the production mechanism of N, NH and NH_2 radicals in the Ar-NH_3 plasma. Subsequently, the role of these reactive species in the deposition mechanism of $a\text{-SiN}_x\text{:H}$ was determined by investigating the effects of SiH_4 addition to the plasma. From measurements of the radical and ion densities in the $\text{NH}_3\text{-SiH}_4$ containing plasma it was established that N and NH_2 radicals govern the mechanism of nitrogen incorporation in the deposited film, while silicon atoms are most likely brought to the surface in the form of SiH_x ($x=0\text{-}3$) radicals.

The second subject of study was the deposition of ultrathin amorphous silicon ($a\text{-Si:H}$) films on wafer substrates, which is of eminent importance in recent applications of $a\text{-Si:H}$ for surface passivation and in silicon heterojunction solar cells. Three *in situ* and real time diagnostic techniques probing different properties of the $a\text{-Si:H}$ /crystalline silicon system were implemented in an ultra high vacuum setup

that provided well defined conditions for a-Si:H growth. Spectroscopic ellipsometry (SE) was used to monitor the time-evolution of the dielectric function as well as the surface roughness and film thickness, while infrared absorption spectroscopy in the attenuated total reflection (ATR) geometry was introduced to monitor bound forms of hydrogen in the film. The non-linear optical technique of second-harmonic generation (SHG) was implemented to monitor the buried interface and surface properties of the growing film. In the first 50 Å of a-Si:H growth, the SE measurements revealed a higher bandgap for the ultrathin films compared to thick bulk films. The thickness trend in this shift of the bandgap was found to be *independent* of the substrate temperature. Infrared absorption spectroscopy measurements carried out simultaneously, demonstrated the presence of a hydrogen-rich interface layer that is clearly *dependent* on the substrate temperature. The difference in temperature dependence suggests that the bandgap shift observed by SE for films with decreasing thickness is not caused by the hydrogen-rich interface layer. In addition, the bandgap shift as a function of film thickness could be fitted remarkably well to a one-dimensional quantum confinement model. Therefore, we argue that quantum confinement is the origin of the observed higher bandgap for ultrathin films. From the described experiments it was established that the multi-diagnostic approach chosen in this study is very promising for future investigations of the deposition of ultrathin amorphous silicon films on hydrogen terminated silicon substrates. Preliminary SHG measurements, carried out simultaneously with the SE and ATR experiments, indicate, for example, that SHG might be very sensitive to epitaxial film growth for ultrathin films. Detection of epitaxial or amorphous initial growth is one of the first steps in understanding and controlling the interface formation of a-Si:H, which is very important for the applications of thin films in solar cells.

Acknowledgements

Het ligt nu voor je, vier jaar werk in de vorm van een boekje. Uiteraard was dit niet mogelijk geweest zonder de medewerking en ondersteuning van vele personen. Daarom wil ik iedereen die een bijdrage heeft geleverd hartelijk bedanken. Bedankt!

In het bijzonder gaat mijn dank uit naar mijn copromotor Erwin. Jouw aanstekelijk enthousiasme voor de fysica heeft erg motiverend gewerkt. Ook de gedetailleerde correcties op het geschreven werk – soms zelfs binnen een dag nadat het geschreven was – waren vooral in het laatste jaar erg belangrijk. Maar naast de onmiskenbare toegevoegde waarde die je hebt gehad voor de wetenschappelijke inhoud van dit proefschrift, waren de gesprekken aan de bar over menig (niet altijd even zinnig) onderwerp ook altijd erg gezellig!

Ook Richard ben ik veel dank verschuldigd. Allereerst voor de wetenschappelijke input op mijn werk, maar ook voor het creëren van een groep met een zeer prettige werksfeer, waarin de mogelijkheden bijna onbeperkt zijn. Het is fijn om met iemand te werken met zoveel nieuwe en “wilde” ideeën.

De bijdragen van afstudeerder Hans en stagiaire Carolien zijn ook van groot belang geweest. Jullie werk vormt het fundament voor het eerste deel van dit proefschrift! Ondanks dat de metingen niet altijd voorspoedig liepen zijn de uiteindelijke resultaten toch heel mooi! Bedankt voor de samenwerking! Ook Jean-Pierre en Joost wil ik bedanken voor de prettige samenwerking. Met zijn tweeën werken aan een project blijft toch leuker dan in je eentje!

Van doorslaggevend belang voor de experimenten was de technische ondersteuning van Ries en Jo. Zonder jullie bijdrage zou de PMP groep er heel anders uitzien. Altijd weer een slim ontwerp, met vakmanschap gemaakt, als de oplossing voor een nieuw probleem. Een speciaal bedankje gaat uit naar Erik, Bram en Jean-Pierre voor het lezen van delen van dit proefschrift. Also Andrew is thanked for reading the manuscript cover-to-cover and commenting on the scientific as well as the linguistic content. Naast mijn kamergenoten Jean-Pierre en Ioana, wil ik de collega's van PMP bedanken voor de gezellige tijd en prettige samenwerking. Ook de hulp van Jeanne, Lianne, Bertus en Herman moet hier vermeld worden. Bedankt.

Naast bovengenoemde werk gerelateerde bedankjes is hier ook een woord van dank voor vele vrienden en teamgenoten op zijn plaats. Jullie hebben ervoor gezorgd dat ik de nodige ontspanning kreeg naast mijn promotie. Tijdens lunchtijd op donderdag was het steevast zaalvoetballen met Bal op 't Dak. Rob, Tom, Erik, Jef, Alquin, Jeroen, en ook Twan: bedankt. Ook bedank ik mijn hockeyteam en tennisteam voor de vele uurtjes ontspanning, waarna ik weer fris aan het werk kon gaan. In het bijzonder wil ik de Stiefelcommissie Natuurkunde bedanken voor de vele gezellige uurtjes op donderdagmiddag in de “Salon” van Van der Waals, de Stiefel-avonden en uiteraard de legendarische weekenden. Ook alle “Kneudels” worden bedankt voor de etentjes, feestjes, gesprekken en de ontzettend gezellige weekendjes. Jullie hebben

nog een weekendje tegoed! Sonja, Yolanda en Jelle wil ik eveneens bedanken voor de gezellige avonden en weekenden, waarin we ontzettend veel hebben gelachen. Bijna als laatste wil ik mijn schoonfamilie – Peter, Ine, Urs en Greg – bedanken voor hun steun en interesse.

Uiteraard wil ik ook mijn ouders bedanken voor hun liefde, interesse, goede zorgen en steun. Zonder jullie had ik hier waarschijnlijk niet gestaan. Ook mijn zus Ciske wil ik bedanken voor haar steun, het is altijd weer gezellig als we met z'n allen thuis zijn. Als laatste, Daniëlle, wil ik jou bedanken voor al je liefde en steun. Jouw bijdrage in de hectische maanden voordat dit proefschrift af moest zijn is van onschatbare waarde. Nu heb ik weer tijd voor je!

Peter

Januari 2007

Curriculum Vitae

Curriculum Vitae

24 June 1978

Born in Oss, The Netherlands.

June 1996

Diploma Gymnasium,
Titus Brandsma Lyceum, Oss.

September 1996 – October 2002

Master's degree Applied Physics,
Eindhoven University of Technology, Eindhoven, The Netherlands.

Three months (spring 2001) traineeship in the group of prof. R.G. Clark,
Centre for Quantum Computer Technology,
University of New South Wales, Sydney, Australia.

Master thesis project in the group Equilibrium and Transport in Plasmas,
Department of Applied Physics, Eindhoven University of Technology,
Eindhoven, The Netherlands.

November 2002 – March 2007

PhD Student, Plasma & Materials Processing,
Department of Applied Physics, Eindhoven University of Technology,
Eindhoven, The Netherlands.

Three months (summer 2005) working visit in the group of prof. R.W. Collins,
Department of Physics and Astronomy, The University of Toledo, Toledo, U.S.A.

